Effect of Interplanetary Trajectory Options on a Manned Mars Aerobrake Configuration

Robert D. Braun,
Richard W. Powell,
and Lin C. Hartung
Langley Research Center
Hampton, Virginia

Contents

Acknowledgments

Summary

Manned Mars missions originating in low-Earth orbit (LEO) in the time frame 2010 to 2025 were analyzed to identify preferred mission opportunities and the associated vehicle and trajectory characteristics. Interplanetary and Mars atmospheric trajectory options were examined under the constraints of an initial manned exploration scenario. Two chemically propelled vehicle options were considered: (1) an all-propulsive configuration, and (2) a configuration that employs aerobraking at Earth and Mars with low lift-drag (L/D) shapes. For the all-propulsive option, mission feasibility depends on the initial required LEO weight, and numerous interplanetary transfer options must be considered. In an aerobraking scenario, aerodynamic and thermodynamic issues associated with the atmospheric passage must also be assessed. This investigation addresses both the interplanetary trajectory options and the Mars atmospheric passage to provide a coupled trajectory simulation. The interplanetary transfer is shown to influence the Mars atmospheric passage by specifying the Mars entry velocity (hence, the required velocity decrement) and the Mars arrival weight (thus, the ballistic coefficient). Conversely, the atmospheric trajectory affects the interplanetary transfer selection by providing: (1) a maximum deceleration limit (based upon physiological factors), (2) a minimum entry-corridor width (imposed by interplanetary guidance accuracy), and (3) a maximum heating rate as a result of thermal protection system (TPS) characteristics.

In this analysis, direct and Venus swing-by interplanetary transfers with a 60-day Mars stopover are considered. The range and variation in both Earth- and Mars-entry velocity are also defined. Two promising mission strategies emerged from the study: (1) a 1.0- to 2.0-year Venus swing-by mission, and (2) a 2.0- to 2.5-year direct mission. Through careful trajectory selection, 11 mission opportunities are identified in which the Mars-entry velocity is between 6 and 10 km/sec and the Earth-reentry velocity ranges from 11.5 to 12.5 km/sec. Patched conic theory is utilized to simulate the interplanetary trajectories, and the equations of motion are integrated numerically during the Mars atmospheric passage. Simulation of the Earth-return aerobraking maneuver is not performed.

This investigation shows that a low L/D configuration (L/D ≤ 0.28) is not feasible for Mars aerobraking without substantial improvements in the interplanetary navigation system. However, even with an advanced navigation system (capable of reducing the initial-state error to ±0.25° in flight-path angle), entry-corridor and aerothermal requirements restrict the number of potential mission opportunities. This study also shows that for a large blunt Mars aerobrake configuration, the effects of radiative heating can be significant at entry velocities as low as 6.2 km/sec and will grow to dominate the aerothermal environment at entry velocities above 8.5 km/sec. The large stagnation-point heat rate associated with radiative heating dictates the use of an ablative TPS for a majority of the Martian aerocapture maneuvers. Despite the additional system complexity associated with an aerobraking vehicle, the use of aerobraking was shown to significantly lower the required initial LEO weight. In comparison with an all-propulsive mission, savings between 19 and 59 percent were obtained, depending on launch date. Also, aerobraking reduced the variance in initial LEO weight with launch date and thereby provided mission flexibility.

Introduction

Objectives and Scope

With the use of an operational space station as an initial staging node in low-Earth orbit (LEO), recent studies (refs. 1 and 2) have shown that manned exploration of the solar system will be technically feasible early in the 21st century. Because of its proximity, environment, and scientific interest, Mars will most

likely be the first planet visited by man. In this investigation, a range of interplanetary and atmospheric trajectory options have been studied to identify and quantify the relative effects of various mission requirements upon the initial flights of a manned Mars program in the time frame 2010 to 2025.

Although a number of propulsive options have been proposed for manned Mars missions (surveys are given in refs. 3 and 4), a transportation system that relies upon chemical propulsion is generally considered to be the leading candidate for an early manned expedition, because it is based upon well-established technology. Hence, in this analysis, interplanetary trajectory simulations are performed for a chemically propelled vehicle that is consistent with several recent analyses (refs. 5 and 6).

While many interplanetary studies incorporate the LEO weight reductions associated with an aerobraking mission, the effects of the atmospheric passage upon mission feasibility are generally neglected. Other studies (surveyed in refs. 7 and 8) have addressed the problems associated with atmospheric braking at the higher speeds encountered by an interplanetary vehicle; however, the effects of the various entry conditions (velocity and mass) dictated by the interplanetary transfer are generally not included. That is, the interplanetary and atmospheric trajectories have been assessed independently, when in actuality they are inherently coupled. Thus, one objective of this investigation is to couple the interplanetary and Mars atmospheric trajectory simulations. This coupling allows the effect of various interplanetary transfer characteristics upon the feasibility of aerobraking at Mars to be identified. Also, the restrictions imposed upon the interplanetary trajectory by the atmospheric passage are determined. In this manner, trajectories that meet both the interplanetary and Mars atmospheric mission requirements are identified.

There is a great deal of debate over the actual entry conditions that will be encountered during Mars entry and Earth reentry; hence, particular attention has been focused on defining these entry envelopes. In a mission that features high-energy aerobraking, these entry conditions are another constraining factor (in addition to the required initial LEO weight).

Because of the energy requirements associated with interplanetary transfer, an aerobraking vehicle may encounter a more severe aerothermal flight environment than either Apollo or the Space Shuttle, particularly upon return to Earth. (See ref. 8.) To help characterize the nonequilibrium flow regime, which cannot be simulated in existing experimental facilities, NASA has proposed the Aeroassist Flight Experiment. (See ref. 9.) This experiment will assess the flight environment during return to Earth from geosynchronous orbit or from the Moon. Because of the packaging efficiency inherent to blunt configurations with low values of L/D, the knowledge gained through the Apollo program, and the present AFE research, shapes with low values of L/D (figs. 1 to 4) have been widely accepted as being applicable to manned Mars missions that feature aerobraking at both Earth and Mars (ref. 8). However, the Earth-return entry velocities, upon completion of an interplanetary mission, are greater than those predicted for the Aeroassist Flight Experiment (AFE) or encountered by Apollo. Furthermore, because the ballistic coefficient for an interplanetary return vehicle may be substantially different from that of either Apollo or the AFE, this shape may not be optimal. Because the Martian atmosphere is vastly different from that of Earth in both composition and density, AFE and Apollo results cannot be directly applied to this flight regime. Also, celestial navigation and thermal protection issues at Mars are significantly different than those at Earth. Therefore, another objective of this investigation is to study the feasibility of high-energy aerobraking at Mars with a large, blunt, low L/D vehicle configuration.

One of the unresolved questions concerning high-energy aerobraking at Mars is in regard to the magnitude and type of aerothermodynamic environment that the vehicle will encounter. In general, convective heating is dominant for vehicles with small nose radii, whereas radiative heating tends to dominate the thermodynamic environment about blunt configurations at higher velocities. There is a great deal of debate as to the significance of radiative heating over blunt vehicles during Mars aerocapture. Because the Martian atmosphere is predominantly composed of CO_2, it is expected to be a stronger radiator than the atmosphere of Earth. However, because the atmospheric entry velocities upon Mars entry are much lower than those associated with Earth reentry, it has been suggested that a reduced aeroheating environment actually exists at Mars (particularly the radiative environment). Thus, there are differing views as to the dominant type of heating that will be encountered—convective or radiative (ref. 8). Furthermore, because radiative heat transfer is a more complex issue than convective heating, most preliminary design studies do not incorporate this type of heat transfer into the analysis. This investigation addresses the validity of attempting Martian aerocapture with a low L/D shape, and establishes preliminary guidelines pertaining to the type of heating present in the stagnation region of a large blunt vehicle during Mars aerocapture. Hence, the Mars aerobraking assessment includes an aerodynamic

performance evaluation as well as the relative effects of convective and radiative heating upon the number of possible mission opportunities.

In summary, the objectives of this investigation are to (1) identify energy-efficient interplanetary transfer options and mission opportunities in the time frame 2010 to 2025, (2) define the range and variation in atmospheric entry conditions upon Mars arrival and Earth return, (3) evaluate the aerodynamic performance and stagnation-point aerothermodynamic environment of a large, blunt, low L/D Mars aerobraking configuration, and (4) provide a mission study in which the interplanetary and Mars atmospheric trajectory simulations are coupled.

Exploration Strategies

In general, manned Mars missions may be split into two categories that have different programmatic goals. In one category, the objective is to place man on the surface of Mars for a short period of time. In the other category, a permanent manned presence is the goal. The first of these will be referred to as an initial-excursion-class mission. In this scenario, a relatively small crew of four to eight members explores the Martian surface for 30 to 90 days. (See refs. 10 and 11.) Because this is to be mankind's first visit to another planet, the crew brings all the supplies that are needed and lives out of their descent craft. Also, because of the limited knowledge available concerning man's ability to survive for an extended period of time in the zero-gravity environment of space, total trip time becomes a major concern, and transfers that are as short as possible are desired.

In the second scenario, which will be referred to as the Mars base approach, the number of crew members varies from 6 to 20. In this strategy, the crew spends a much longer time on Mars (1 to 3 years). (See refs. 12 and 13.) Transfer time is not as stringent a constraint, and most of the supplies are not transferred with personnel, but rather on separate cargo missions. In this exploration scenario, the crews live in a base camp environment and are slightly more independent of their transfer ship or ships. Furthermore, to decrease the required weight that must be initially lifted to LEO, many of these missions assume Martian production of the propellant required for Earth return. (See refs. 13 and 14.)

In a buildup strategy, initial excursion-class missions are first attempted to remove the key technological barriers associated with interplanetary flight. These missions are performed to provide the first manned presence on another world, albeit temporary. In this scenario, the initial excursion-class mission is treated as a required step, but not as an end in itself. Gradually, these missions become more ambitious until a Mars base approach is deemed technologically feasible. A general survey of various proposed mission concepts is provided in reference 15.

Because man must reach Mars before undertaking more advanced mission options, the initial excursion scenario is of prime importance. Thus, the focus of this investigation is to identify and qualify the aspects of a candidate initial excursion-class mission. The general guidelines followed in this analysis include (1) a crew of six, (2) a total trip time of 1 to 2.5 years, which, to be consistent with other studies (refs. 10 and 11) includes a 60-day Mars stopover, and (3) launch from LEO in the time frame 2010 to 2025. Transportation infrastructure assumptions include the use of an advanced launch vehicle to transfer the required mass into LEO and the use of a space station for on-orbit assembly of the interplanetary vehicle.

Planetary Ephemeris Cycles

Because the planets travel at different angular rates about the Sun, the relative position of any two given bodies is constantly changing according to cyclic, geometric phasing. These cycles, which can greatly affect the characteristics of a high thrust trajectory, are partially responsible for the efficiency and atmospheric entry conditions of a given trajectory. In the Earth-Mars system, the planetary motion can be modeled by the superposition of two synodic variations. The first of these variations is caused by the motion of the two planets about the Sun at different angular rates. As shown in figure 5, if the two planets begin in a certain relative orientation (in this case celestial opposition) at time zero, 2.135 years or approximately 25.62 months will elapse before the two bodies return to that same relative angular position. At that point, the heliocentric angle between Earth and Mars is repeated; however, as shown in figure 6, the two planets are in a different heliocentric position. While the Earth's orbit is approximately circular, Mars' orbit is not. Although slight, its eccentricity ($e \approx 0.093$) is large enough to vary the planet's radial position from the Sun and affect the efficiency of a given trajectory. Note that figures 5 and 6 are drawn to scale. The planets will return to their approximate original heliocentric position every seven to eight oppositions, or 15 to 17 years (fig. 6).

For certain interplanetary transfers, the spacecraft's flight path falls inside the Earth's orbit. Under these circumstances, the gravitational attraction of Venus can become significant. If the motion of Venus is included, the planetary cycles become even more complex. Because of the involvement of a third planet, each particular geometric alignment is less frequent, and fewer feasible mission opportunities

should exist. However, because Venus moves faster than Mars about the Sun (by a factor of approximately three in angular rate), it is generally available as a trajectory shaping force on either the inbound or outbound interplanetary leg. Once again, two synodic cycles exist between the position of Venus and the time of Earth-Mars alignment (e.g., celestial opposition). As shown in figure 7, every third Earth-Mars opposition (or once every 6.405 years), all three planets will return to the same relative angular position. However, once again because of a variance in Mars' radial position from the Sun (Venus' orbit is roughly circular), the fact that the three planets are not in the same heliocentric position becomes significant. The three planets will return to the same approximate heliocentric alignment once in every 15 Earth-Mars oppositions, or 32.025 years.

Mission Options

Interplanetary trajectory options. High-thrust interplanetary transfers that are applicable to a manned Mars mission can be split into two categories—conjunction-class and opposition-class transfers. The term opposition refers to the situation when the Sun and Mars are on opposite sides of the Earth, whereas conjunction implies that the Sun and Mars are on the same side of the Earth. This Earth centered reference frame is commonly used by astronomers to record the positions of stars. Although interplanetary analyses are better suited to a heliocentric reference frame, these names are still utilized to classify the various mission modes.

In a conjunction-class mission (fig. 8), an energy-efficient (near Hohmann) transfer is utilized on both the outbound and inbound legs. However, because the Earth and Mars move about the Sun at different angular rates, a relatively long Mars stopover is required to insure the proper planetary alignment on both legs of the trajectory. In general, this stopover is on the order of 500 days, and the total transfer time is approximately 2.5 to 3.0 years. Because this trajectory class is long in both total duration and Mars stay time, it is better suited for a program in which the goal is a manned Mars base rather than an initial-excursion-class mission. In this investigation, all the interplanetary transfers can be classified as opposition-class trajectories, in which a short Mars stay time (on the order of 30 to 90 days) forces a compromise between optimal inbound and outbound legs. Generally, in this type of mission, one leg of the trajectory is an energy-efficient transfer, and the other is forced to pass within the orbit of the Earth (fig. 9). This trajectory class is characterized by a short Mars stopover and a relatively short total trip time; thus, it is applicable to an initial-excursion scenario.

Three opposition-class trajectory modes were simulated in this analysis: (1) direct, (2) inbound Venus swing-by, and (3) outbound Venus swing-by. Several other types of interplanetary transfers (which were not examined in this investigation) exist for a chemically propelled vehicle that is performing an initial-excursion-type mission. These include transfers that utilize more than one planetary swing-by and missions that incorporate a complex burn sequence.

Vehicle characteristics and baseline mission scenario. The mission begins as the interplanetary vehicle is assembled at the space station in LEO. After arrival at Mars via one of several possible interplanetary transfers, the vehicle is placed in a polar elliptical orbit with a period of 1 Martian day (approximately 24.6 hours). This orbit is achieved either propulsively or with the use of atmospheric braking. The eccentricity of this parking orbit was chosen as a compromise between the relatively simple logistics provided by a circular orbit and the inherent propellant savings of an extremely eccentric orbit, such as one with a 48-hour period. (See ref. 16.) Choice of a polar orbit allows for the selection of a high-latitude landing site and potential global coverage from orbit, and yields a conservative estimate of lander propellant. For an actual mission, selection of the Mars parking-orbit inclination, eccentricity, and periapsis altitude is primarily dictated by orbital precession concerns. That is, the parking orbit must be selected such that, upon completion of the Mars stopover, the orbit has precessed into an orientation consistent with the departure trajectory requirements. In this investigation, orbital precession issues were not examined. The crew descends to the surface in the Mars excursion module (MEM). After performing the necessary excursion operations, the crew returns to the MEM, a portion of which ascends to orbit, and preparations for Mars departure are made. The total time of Mars operations assumed in this study is 60 days. After discarding unnecessary components (such as the Mars arrival propellant tankage and the Mars ascent vehicle), the vehicle performs a high-thrust maneuver to begin its journey back to Earth. The mission is concluded with the return of the vehicle to the space station in LEO. Earth-return deceleration is accomplished either propulsively or with the use of an aerobrake.

To provide analysis flexibility, the trajectory analysis portion of this research was performed through a series of weight-ratio calculations in which all vehicle weights were nondimensionalized by the Earth-return

weight. This method makes the results presented in this investigation applicable to any vehicle design, provided that two vehicle parameters remain approximately constant: (1) the propulsion systems must be similar (in terms of specific impulse and tankage weight), and (2) the ratio of weight left behind at Mars to Earth-return weight must be comparable. Also, the use of an impulsive velocity addition must be valid. (Hence, the vehicle must use a high-thrust propulsion system.) Therefore, in this analysis, a general class of interplanetary spacecraft is being studied as opposed to a specific vehicle.

Propulsive option. The vehicle used as a baseline in this analysis is similar to that developed in reference 5 and is conceptually shown in figure 10. The vehicle mass breakdown is given in table 1. Estimates of its mass have been computed for missions of both 1.0 to 2.0 years and 2.0 to 2.5 years and are listed in table 1. The propellant used is LOX/LH_2, and a chemical rocket engine characterized by a vacuum specific impulse I_{sp} of 480 sec is assumed.

Because the total trip time is at least 1 year, the spacecraft's two habitation modules are attached to either end of a rotating truss structure; in this manner, an artificial gravity environment is produced (refs. 5 and 17). The habitation modules, which are similar in size to space-station hardware, provide a total volume of 325 m^3 (approximately 200 m^3 of living space). Also, by utilizing two small habitation modules, as opposed to a single large one, an inherent safeguard in the event of an accidental depressurization of a portion of the living space is included. Also aboard the vehicle is the MEM, which includes all vehicle components used in the descent to, exploration of, and ascent from the Martian surface. If a 1.0- to 2.0-year mission is flown, three of six crew members use the MEM to explore the Martian surface. For a longer mission, allowances have been made so that as many as six crew members are able to descend to the surface. (See table 1.) The MEM descent and ascent stages have been sized for use in conjunction with a 24.6-hour, polar orbit. (See ref. 18.) For a 2.0- to 2.5-year mission, a third space-station module is adapted as an onboard zero-gravity laboratory. This module would be situated just behind the MEM to provide another 100 m^3 of living space but is not shown in figure 10.

Aerobraking option. By utilizing atmospheric drag to decelerate the vehicle, aerobraking provides a significant reduction in the required initial LEO weight. For a mission that features aerobraking at both Earth and Mars, the interplanetary vehicle is modeled differently and is conceptually shown in figure 11. The same habitation modules, truss structure, and MEM are included; however, the truss structure must be retracted prior to Mars arrival so that the habitation modules are shielded. In contrast to the propulsive option, there are no braking stages to perform the Mars-arrival and Earth-return maneuvers; instead, a double aerobrake system exists. The larger aerobrake is used to achieve the correct parking orbit at Mars as well as to provide protection to the MEM as it descends to the surface. The smaller aerobrake is used upon Earth return.

The vehicle configuration shown in figure 11 is being used only to illustrate the relative size of each of the vehicle components. In the final configuration, the MEM, habitation modules, Mars-departure propellant, and Earth-return aerobrake are positioned behind the Mars aerobrake so as to be shielded from the intense aerothermal environment. This packaging analysis is described in the section "Vehicle Packaging," and the final vehicle configurations are considerably different than that illustrated in figure 11.

The low L/D aerobrakes utilized in this investigation are modeled after the AFE configuration. (See ref. 19.) The AFE shape was chosen so that the large amount of aerodynamic and thermodynamic research performed on the AFE could be utilized in the present analysis. Details of both the aerodynamic characteristics and thermodynamic properties of this shape are discussed in subsequent sections.

Earth-return modes. Whether the Earth return is accomplished propulsively or by aerobraking, two modes were studied. In the first scenario, the habitation modules and the artificial gravity device are returned to the space station for refurbishment in LEO. The second mode utilizes a small crew-return capsule to lower the weight that must be braked upon Earth return. In this scenario, just prior to the interplanetary encounter with Earth, the crew leaves the habitation modules and transfers into the Earth-return capsule. This module returns to LEO, and the habitation modules and truss structure are left in heliocentric orbit. The first mode is well suited for a mission in which reusability is a major concern; however, in the second mode, the complexity of the Earth-return maneuver is greatly simplified by utilizing a crew-return module. In a propulsive mission, this translates into lower propellant requirements; in an aerobraking scenario, the second option requires less weight to be captured. Hence, the second Earth-return mode is more probable for an initial manned mission.

Although two Earth-return aerobraking options are investigated from a mission scenario standpoint, this study simulates only the atmospheric passage at Mars. The Earth-return aerobrake concepts are

included only because, as a portion of the vehicle Mars payload, the size and weight of the Earth-return aerobrake affects the Mars aerobrake configurations.

In summary, the mission options considered in this investigation include: (1) direct versus Venus swing-by interplanetary transfers, (2) propulsive versus aerobraking deceleration, and (3) use of an Earth-return vehicle (habitation modules and truss structure) versus an Earth-return capsule.

Symbols

C	constant for a specific atmospheric composition used in Sutton-Graves equation, $\frac{\text{kg}^{1/2}}{\text{m}}$
C_D	drag coefficient
$C_{f,c}$	continuum-regime aerodynamic coefficient
$C_{f,fm}$	free molecular-regime aerodynamic coefficient
$C_{f,\text{tran}}$	transitional-regime aerodynamic coefficient
C_L	lift coefficient
conv	convective
d	declination, deg
$d_{p,s}$	average planetary distance from Sun, m
e	eccentricity
F_{drag}	drag force, N
F_g	gravitational force, N
F_{lift}	lift force, N
F_{solar}	solar force, N
F_{thrust}	thrust force, N
F_{total}	sum of all forces, N
G	gravitational constant, 6.67×10^{-11} Nm^2/kg^2
G_{max}	maximum encountered deceleration, g units
g	Earth's gravitational acceleration constant, 9.81 m/sec^2
I_{sp}	specific impulse, sec
K	bend angle, deg
Kn	Knudsen number

L/D	lift-drag ratio
l_{ref}	aerobrake reference length (base diameter), m
M	mass of celestial body, kg
m	mass of vehicle, kg
m_f	mass of vehicle just after propulsive maneuver, kg
m_i	mass of vehicle just prior to propulsive maneuver, kg
$\dot{q}_{\text{max}}$	stagnation-point maximum total heat rate, W/cm^2
$\dot{q}_{s,\text{conv}}$	stagnation-point convective heat rate, W/cm^2
$\dot{q}_{s,\text{rad}}$	stagnation-point radiative heat rate, W/cm^2
R	radius of curvature of AFE aft skirt
r	vehicle position vector relative to dominant celestial body, m
$\ddot{r}$	vehicle acceleration vector relative to dominant celestial body, m/sec^2
r_{atm}	atmospheric interface radius, km
r_n	acrobrake effective nose radius, m
r_p	planetary position vector or vehicle position vector at periapsis, km/sec
$r_{p,vac}$	position vector at periapsis in a vacuum
r_{SOI}	radius of SOI of celestial body, m
r_{XY}	AFE ellipsoidal nose radius in X-Y plane, m
r_{XZ}	AFE ellipsoidal nose radius in X-Z plane, m
rad	radiative
S	reference aerodynamic surface area, m^2
t	time, sec
V	velocity, m/sec
V_{atm}	vehicle velocity at atmospheric interference, m/sec
V_1	vehicle heliocentric velocity vector upon entrance to SOI of Venus, m/sec
V_2	vehicle heliocentric velocity vector upon exit from SOI of Venus, m/sec
V_{HP}	vehicle relative velocity vector, m/sec

V_{HP1}	vehicle relative velocity vector upon entrance to SOI of Venus, m/sec
V_{HP2}	vehicle relative velocity vector upon exit from SOI of Venus, m/sec
V_p	velocity vector of planetary body or vehicle velocity vector at periapsis, m/sec
V_∞	free-stream velocity vector, m/sec
W_f	final LEO weight
W_i	initial LEO weight
W_i/W_f	vehicle weight ratio
α	angle of attack, deg
γ	ratio of specific heats
γ_{atm}	flight-path angle at atmospheric interface, deg
ΔV	impulsive velocity change, m/sec
μ	gravitational parameter, constant for each celestial body, kg^3/sec^2
ρ	atmospheric density, kg/m^3
σ	standard deviation

Acronyms:

AFE	Aeroassist Flight Experiment
CFD	computational fluid dynamics
CG	center of gravity
CO_2	carbon dioxide
COSPAR	Committee on Space Research
LaRC	Langley Research Center
LEO	low-Earth orbit
LH_2	liquid hydrogen
LOX	liquid oxygen
MEM	Mars excursion module
MMC	Martin Marietta Corporation
MRSR	Mars Rover Sample Return
MSFC	Marshall Space Flight Center
NASA	National Aeronautics and Space Administration
POST	Program to Optimize Simulated Trajectories
RAD	radiation model

RIFSP	Radiation Inviscid Flow Stagnation Point program
SAIC	Science Applications International Corporation
SMART	Solid Modeling Aerospace Research Tool
SOI	sphere of influence
SWISTO	Swing-by Stopover Optimization program
TPS	thermal protection system

Flight Mechanics

Patched Conic Theory

During an interplanetary trajectory, the motion of a vehicle is affected by several celestial bodies. The relative effect that the gravitational force of each body has upon the vehicle motion is proportional to both the body and vehicle masses and is inversely proportional to the square of the radial distance of the vehicle from the body. This gravitational force may be expressed as

$$F_g = \frac{-GMmr}{|r|^3}$$

For a Mars mission, the major gravitational forces are due to the influence of the Sun, Earth, Mars, and possibly Venus, upon the vehicle. During an actual interplanetary transfer, each of these bodies affects the spacecraft throughout its entire flight as do the Moon, Phobos and Deimos (the two Martian moons), and the other planets. Furthermore, the relative effect each body has upon the vehicle gradually changes with distance. For example, in LEO, the Earth produces the dominant gravitational attraction; but while the vehicle is in orbit about Mars, the Martian gravitational force is dominant.

Other forces may be present because of atmospheric drag, solar pressure, and the vehicle thrust. Newton's second law (in an inertial reference frame) may be expressed as

$$\frac{d}{dt}(mV) = F_{total}$$

where, for an interplanetary transfer,

$$F_{total} = F_{g,Sun} + F_{g,Earth} + F_{g,Mars} + F_{g,other} + F_{thrust} + F_{drag} + F_{solar}$$

In patched conic theory, approximations are made which greatly simplify the analysis. By modeling

7

each body as being spherically symmetric, all forces can be assumed to act through the body center of mass. Also, by reducing the problem to include only two bodies and the gravitational force between them, the equation is greatly simplified. For example, over the portion of the transfer in which the Sun is the dominant gravitational body, $F_{total} = F_{g,Sun}$.

With these assumptions, Newton's second law yields a simplified equation of motion. (For a complete derivation and list of assumptions, see ref. 20.) This two-body equation of motion may be expressed as

$$\ddot{r} + \mu \frac{r}{|r|^3} = 0$$

During the atmospheric passage, as a result of the addition of aerodynamic forces, this equation is not valid, and the equations of motion are numerically integrated. However, two-body motion is applicable to the high-thrust interplanetary portion of the mission and was used in this investigation. To understand this application, the concept of a sphere of influence (SOI) must be introduced. The sphere of influence is defined as an imaginary sphere about each planetary body. Once within this sphere, the vehicle motion is assumed to be governed solely by the gravitational force between the vehicle and the enclosed celestial body. The size of a planet's SOI is a function of its mass relative to the Sun and its distance from the Sun. Approximate sizes of Earth, Mars, and Venus spheres of influence are given in table 2, along with other pertinent celestial data. The size of each planet's SOI is obtained from an approximate formula first derived by Laplace. (See ref. 20.) This expression may be written as

$$r_{SOI} = d_{p,S} \left(\frac{M_{planet}}{M_{Sun}} \right)^{0.4}$$

Because an average planetary distance from the Sun is utilized in the SOI expression, the size of each SOI is approximated as constant regardless of time. Using the SOI assumption for two-body motion, numerous gravitational forces are not simulated; instead, only the dominant gravitational force affects the motion of the spacecraft. Furthermore, the effects of the other celestial bodies (such as the Moon, Phobos, Deimos, and the other planets) are never taken into account. However, because patched conic theory greatly simplifies the equations of motion, a large number of trajectories may be simulated quickly; hence, it is ideal for preliminary mission design studies.

Interplanetary Trajectory

Direct mode. In the direct transfer mode, the vehicle travels directly to Mars and back. However, when both a short total trip time and a short Mars stopover are mission requirements, a feasible energy-efficient trajectory is difficult to obtain, because one of two adverse conditions generally arises.

In the first situation (fig. 12), the spacecraft leaves Earth on an energy-efficient transfer to Mars. However, by the end of the outbound transfer, the Earth has begun to lead Mars in its angular orientation about the Sun. Therefore, after the Mars stopover, the vehicle is forced to take a return transfer that can catch up to the Earth in heliocentric angle. To accomplish this, the vehicle must achieve a higher angular speed; thus, its path must fall inside the Earth's orbit. Unfortunately, this type of inbound transfer causes the spacecraft velocity vector to be nontangential to the Earth's velocity vector upon return. This condition leads to either a high atmospheric entry velocity or a large propulsive requirement, either of which has an adverse effect on mission performance. The second situation (fig. 13) results from planning for an Earth-return transfer characterized by either a low entry velocity or smaller propulsive braking requirements. Thus, an energy-efficient inbound transfer is desired. However, for the vehicle to be in the proper return alignment, Mars must lie ahead of the Earth in heliocentric angle on the outbound transfer. This constraint, when coupled with the requirement for a short trip time, forces the outbound transfer to pass within the Earth's orbit and to be of higher energy. A high-energy outbound transfer translates into larger Earth-departure propellant requirements and higher entry velocities at Mars.

Therefore, for a mission in which both a short Mars stopover and a short total transfer time are desired, use of a direct transfer characterizes the mission as having either Earth-departure or Earth-return deficiencies. As either of these two requirements (short Mars stopover or short total transfer time) is relaxed, the trajectory is less constrained, and these adverse effects are reduced.

Venus swing-by mode. In each of the previously described direct transfer modes, the requirements of both a short Mars stopover and a short total transfer time caused one of the transfer legs to pass inside the Earth's orbit. When this occurs and Venus is in the proper position, its gravitational attraction may be used to perturb the trajectory. Thus, by performing a Venus swing-by en route to Mars (outbound swing-by) or prior to Earth return (inbound swing-by), the spacecraft can take advantage

of Venus' gravitational field to adjust its interplanetary trajectory.

The flight mechanics of a Venus swing-by are elegantly described in reference 21. As shown in figure 14, when approaching Venus' SOI, the vehicle has a given heliocentric velocity V_1. However (as described in the section "Patched Conic Theory"), while within Venus' SOI, the motion is assumed to be solely governed by the planet's gravitational force. Therefore, the heliocentric velocity vector must be transformed into one that is relative to Venus. This transformation is accomplished by vectorially subtracting Venus' velocity V_p from the heliocentric velocity, V_1. The resultant vector is the vehicle initial velocity relative to Venus V_{HP1}, and the vehicle is now on a hyperbolic trajectory about Venus. After passing through periapsis, the spacecraft reaches the SOI boundary on its way back into heliocentric space. At this point, the vehicle has velocity V_{HP2} relative to Venus. Upon SOI departure, the velocity is transformed back into a heliocentric reference frame V_2 by vectorially adding Venus' velocity vector. Considering the relationship between the entrance and exit velocity vectors, figure 14 shows that

$$|V_{HP1}| = |V_{HP2}|$$
$$V_{HP1} \neq V_{HP2}$$

$$|V_1| \neq |V_2|$$
$$V_1 \neq V_2$$

Without performing a propulsive maneuver, conservation of energy requires the relative velocity at SOI entrance and exit to be the same magnitude. However, these vectors are oriented in different directions; that is, the relative velocity vector has been rotated through an angle denoted as K. Thus, when the relative velocity vector is recombined with Venus' velocity vector upon SOI exit, a different heliocentric vector results (fig. 14). The heliocentric velocity vectors upon SOI entrance and exit may be different in both magnitude and direction. In this case, the heliocentric velocity was increased; however, by passing Venus on its other side, the heliocentric velocity may be decreased. Through the use of this trajectory-shaping technique, the spacecraft may either gain or lose energy relative to the Sun without performing a propulsive maneuver. When used properly, this effect can result in a lower initial LEO weight. (See ref. 22.) Furthermore, a Venus encounter may be used to affect the atmospheric entry conditions at the subsequent planet. (See ref. 23.) The effect which the Venus swing-by has upon the interplanetary transfer depends on the magnitude of the relative velocity

vector at the SOI and the closest approach distance, which is physically constrained by the edge of Venus' atmosphere. The range of achievable bend angles K without the use of propulsion is governed (ref. 23) by

$$\csc\left(\frac{K}{2}\right) = \frac{|r_p||V_{HP}|^2}{\mu} + 1.0$$

Hence, the effect of a Venus swing-by on a given transfer increases as either the magnitude of the SOI relative velocity vector is reduced or the closest approach point is decreased. This bend-angle range may be augmented by using a propulsive maneuver during the Venus encounter (ref. 24). In certain instances, the planetary alignment is such that a Venus swing-by may be performed on both the outbound and inbound transfer legs. (See ref. 11.) However, because of the infrequency of this type of trajectory (one or two possibilities every 15 to 17 years), the current research was limited to round-trip transfers with at most one Venus swing-by. In the outbound swing-by mode, the vehicle is generally accelerated so that it reaches Mars in a shorter period of time. This acceleration may result in either an increased Mars entry velocity or slightly larger propulsive requirements at Mars. However, it allows for a longer, more energy-efficient return transfer and an associated lower Earth-reentry velocity without greatly increasing the total trip time. An example of this type of trajectory is given in figure 15. In the inbound swing-by mode (fig. 9), the vehicle is generally decelerated as it passes Venus on its way back to Earth. Once again, this trajectory results in a lower weight requirement and a lower Earth-reentry velocity.

A comparison of figures 9 and 12 or 13 and 15 shows that the only difference between a Venus swing-by mission and a direct transfer of approximately the same total trip time is the position of Venus. If Venus is in the correct position, its presence will perturb the trajectory and result in improved performance. An inbound Venus swing-by mission (fig. 9) is characterized by lower Earth-return velocities than a direct transfer (fig. 12), and an outbound Venus swing-by (fig. 15) has reduced Earth-departure requirements in comparison with the inverted direct mode (fig. 13). Therefore, when both a short total trip time and short Mars stopover are required, the Venus swing-by can be used to increase the efficiency of a given trajectory, from a weight standpoint, and to lower the Earth-return velocities.

Mars Atmospheric Trajectory

During the Mars atmospheric passage, different equations are utilized to determine the vehicle motion. In this case, the major forces can be attributed

to the Mars gravitational and aerodynamic forces (i.e., lift and drag). No thrusting is performed during the atmospheric passage. Hence, Newton's second law (in an inertial reference frame) may be expressed as

$$\frac{d}{dt}(mV) = F_{g,\text{Mars}} + F_{\text{lift}} + F_{\text{drag}}$$

where

$$F_{g,\text{Mars}} = \frac{-GM_{\text{Mars}}mr}{|r|^3}$$

$$|F_{\text{lift}}| = \frac{1}{2}\rho|V_\infty|^2 SC_L$$

$$|F_{\text{drag}}| = \frac{1}{2}\rho|V_\infty|^2 SC_D$$

This equation is solved numerically with use of a fourth-order Runge-Kutta computational scheme described in the section "Computational Methods."

Mars atmospheric model. Several Mars atmospheric models have been tabulated by David E. Pitts of NASA Johnson Space Center for use in the Mars Rover Sample Return mission (MRSR). The objective of this unmanned mission, which is being planned for the mid-1990's, is to land a rover on Mars and return a sample of the Martian surface to Earth (ref. 25). A great deal of the current research in atmospheric properties, as well as in guidance, navigation, and aerobraking technology, is aimed at the MRSR mission. Because the MRSR mission is viewed as a precursor test-bed scenario for certain systems required in manned exploration, many of the constraints and requirements used in this analysis are based upon the MRSR mission.

The MRSR atmospheric models include the effects of the Martian dust storms and the variation of the Martian atmosphere with latitude and yearly season. For this study, the atmospheric model of the Committee on Space Research north summer mean (COSPAR NS mean) was selected. This model is currently being utilized as the baseline atmosphere for the MRSR mission analysis; furthermore, Viking atmospheric measurements (figs. 16 and 17) tend to substantiate its validity as an average atmosphere. The significant atmospheric properties are tabulated in table 3, and plots of the variation of several atmospheric properties with altitude are given in figures 18 to 21.

Entry-corridor definition. Aerobraking can be defined as a deceleration due to the effects of atmospheric drag upon a vehicle. For an interplanetary transfer, enough energy must be lost that the vehicle is captured into orbit about a planet. If the atmospheric trajectory is too steep, the vehicle will lose

so much energy that it is unable to maintain an orbit and will follow a descent trajectory towards the planet surface. On the other hand, flying a trajectory that is too shallow prevents the vehicle from being captured by the planet's gravitational attraction. In this case, the vehicle would continue to travel through heliocentric space past the target planet. These two scenarios bound the classical definition of an atmospheric entry corridor (ref. 26) as an imaginary corridor in the atmosphere within which the vehicle must fly to be successfully captured about a planet. This corridor is constrained by the two trajectories just described and is illustrated in figure 22.

This definition of entry corridor may be constrained further by selecting a specific capture orbit. For a particular Mars-arrival weight, if a ballistic entry (a zero-lift trajectory) is flown, the vehicle will follow a single trajectory, and the entry corridor concept does not apply (assuming the vehicle has a constant surface area, constant drag coefficient, and is not thrusting). However, for lifting vehicles, proper use of this aerodynamic force can perturb the atmospheric trajectory such that the vehicle flies either above or below its nominal ballistic path. In this investigation, the entry corridor is defined as the imaginary corridor in a planet's atmosphere through which the vehicle is able to fly by modulating its lift vector while still achieving a specified capture orbit. This corridor, which is illustrated in figure 23, includes the vehicle nominal ballistic path and is bounded by two trajectories.

The upper bound is defined by the shallowest trajectory the vehicle can fly and still lose the proper amount of energy. This trajectory is achieved by flying the vehicle in a full lift-down configuration. In this manner, the vehicle stays in the atmosphere as long as possible, and the energy loss is spread out over time. The lower bound of the entry corridor may be defined by a full lift-up trajectory, which is the steepest trajectory the vehicle can fly and still achieve the atmospheric exit conditions required for the specified capture orbit. This atmospheric path takes the vehicle in and out of the atmosphere as quickly as possible and is characterized by higher decelerations than a lift-down passage. Because of the energy loss requirements associated with interplanetary transfer, these decelerations can be large and tend to increase with entry velocity. Therefore, a maximum deceleration limit of $5g$ (49.0 m/sec^2) was imposed as an additional constraint, and the lower bound of the entry corridor is defined as the trajectory through which the vehicle either reaches this deceleration limit ($5g$ limited trajectory) or could not have flown any steeper (full lift-up trajectory).

In general, the width of an entry corridor is a function of the amount of lift the vehicle can generate to perturb it off the nominal ballistic path. Thus, the width is partially governed by the choice of the vehicle L/D. Also, because lift varies with the square of velocity, the vehicle possesses greater control authority with increasing entry speed; however, as the entry velocity increases, the maximum encountered deceleration also becomes larger. The center of the entry corridor is approximately defined by the nominal ballistic trajectory and is determined by the vehicle ballistic coefficient $m/C_D S$. In general, vehicles characterized by high ballistic coefficients decelerate lower in the atmosphere. (See ref. 27.) Because this placement determines the atmospheric density regime through which the vehicle will fly, it will greatly affect the amount of aerodynamic heating the vehicle must withstand.

Finally, because the entry corridor may be thought of as being bounded by a steep and shallow atmospheric passage, its width may be described by the use of flight-path angle at the atmospheric interface. (The atmospheric interface altitudes at Earth and Mars are listed in table 2.) This convention is utilized throughout the present study. That is, the width of the entry corridor is denoted as the difference in the initial flight-path angles of the full lift-down trajectory and either the full lift-up or the $5g$ limiting trajectory.

Interplanetary navigational accuracies. Upon completion of one leg of the interplanetary transfer, the vehicle must achieve an atmospheric-interface flight-path angle within a prescribed range specified by the vehicle aerocapture capabilities. Present-technology interplanetary guidance systems that utilize Earth-based radio tracking are capable of placing a vehicle at the Martian atmospheric interface to within $\pm 1.8°$ (3-σ accuracy) in flight-path angle. (See ref. 28.) Thus, if a 3-σ probability of completing a successful aerocapture with Earth-based tracking alone is required, the entry corridor achievable by an aerobrake configuration would have to be at least 3.6° wide. Recent MRSR studies (ref. 29) have shown that a reduction in this guidance error is achievable by complementing the Earth-based radio tracking with an onboard, optical navigation system. Through optical sightings of the Martian moon Deimos and its known ephemeris data, a more precise vehicle position is obtained. The accuracy of this system is mainly a function of the time at which the optical measurements must be suspended for the vehicle to be readied for entry. As shown in figure 24, if optical measurements are taken up to 2 hours prior to entry, the navigation error is estimated as $\pm 0.5°$—

3-σ accuracy. (See ref. 29.) Thus, the entry corridor would be required to be at least 1.0° in width (the present MRSR requirement). Furthermore, with the use of optical measurements until just prior to entry, the navigation error is estimated as $\pm 0.25°$ -3-σ accuracy (ref. 29) and the required entry corridor would be on the order of 0.5° wide. These guidance-system inaccuracies are tabulated in table 4.

These error estimates do not include atmospheric, midcourse correction or trim angle-of-attack uncertainties. With these effects included in the analysis, the error in entry flight-path angle increases. For example, the $\pm 0.25°$ error in flight-path angle is increased to $\pm 0.42°$ when these effects are included (ref. 28). In this investigation, various corridor width requirements (between 0.5° and 1°) were imposed upon the entry analysis.

Aerodynamics. Of the various possible low L/D configurations, an enlarged version of the AFE was selected. A description of the vehicle geometry (ref. 19) is presented in figure 25. The lift and drag coefficients at various angles of attack are presented in figure 26 under continuum flow conditions. At the AFE trim angle of attack (17°), reference 30 predicts that the vehicle continuum hypersonic L/D is approximately 0.28.

In an aerobraking scenario, the vehicle flies through the entire spectrum of aerodynamic regimes: free-molecular, transitional, and continuum. Thus, throughout the atmospheric passage, the vehicle is characterized by a regime-dependent set of aerodynamic coefficients. In this study, AFE data (ref. 30) obtained through both wind-tunnel and CFD methods were utilized to estimate the aerodynamic coefficients in the free-molecular and continuum regimes. However, to include transitional aerodynamics in the analysis, the Lockheed bridging formula was used to define the lift and drag coefficients as functions of Knudsen number. This formula, which may slightly underpredict the extent of the transitional regime at higher altitudes (ref. 31), utilizes a sine-squared curve fit to estimate the transitional aerodynamics. This bridging formula, used in both the Space Shuttle and AFE programs, can be expressed as

$$C_{f,\text{tran}} = C_{f,c}$$
$$+ (C_{f,fm} - C_{f,c}) \sin^2 \left\{ \pi \left[\frac{1}{3} + \frac{1}{6} \log(Kn) \right] \right\}$$

The Knudsen number (ref. 32) is a nondimensional flow parameter defined as the molecular mean free path divided by the vehicle characteristic length (which for this shape was assumed to be equivalent

11

to the base diameter). It may be used to identify the aerodynamic flow regime as follows:

$$Kn \leq 0.01 \text{ (Continuum flow)}$$

$$0.01 < Kn < 10.00 \text{ (Transitional flow)}$$

$$Kn \geq 10.00 \text{ (Free-molecular flow)}$$

For an AFE characteristic length on the order of 35 m, the Mars atmosphere may be divided into a free-molecular flow regime above 153 km, a continuum flow regime below 97 km, and a transitional flow regime between these altitude limits. The variation of AFE lift and drag coefficients with altitude predicted by the Lockheed bridging formula is shown in figure 27.

Although a free-molecular L/D of 0.0037 was used in this investigation (based on a preliminary analysis), a more detailed study performed by Celenligil, Moss, and Blanchard predicts a free-molecular L/D of 0.010 for the AFE at 17° angle of attack. (See ref. 31.) However, because all of a Mars aerobraking vehicle deceleration occurs at altitudes well below 97 km (as depicted in fig. 23), only continuum aerodynamics are of importance. Thus, the use of the refined free-molecular and transitional aerodynamic coefficients given in reference 31 has an insignificant effect upon this study.

Vehicle packaging. In this investigation, the payload was placed behind the Earth and Mars aerobrakes based on two criteria. The first criterion is that the vehicle must fly at the AFE trim angle of attack of 17°. To accomplish this, the vehicle was packaged to meet the center-of-gravity (CG) requirements determined by an AFE stability analysis. (See ref. 30.)

Because this aerobraking configuration does not completely enclose its cargo, a second packaging criterion was included to protect the vehicle payload during the atmospheric passage. Using CFD techniques, Gnoffo (ref. 33) numerically calculated and classified the streamlines about the AFE configuration according to their flow properties. In this manner, the subsonic and supersonic regions of flow in the wake region behind the aerobrake were determined; the subsonic streamlines behind this configuration are shown in figure 28. By restricting the allowable payload volume to be within this subsonic region, the cargo was assumed to be reasonably safe from the aerothermodynamic environment.

The payload arrangements that satisfied the packaging criteria are illustrated in figures 29 and 30 at both Mars entry and Earth reentry for both the Earth-return aerobrake and capsule modes. From these figures it is evident that by attempting to reuse the habitation modules (Earth-return mode 1), the size of the Earth-return aerobrake is significantly increased; however, there is only a slight increase in the size of the Mars aerobrake. Because of the criterion for subsonic wake-region packaging, the aerobrakes in this investigation are larger than those in most other recent studies (particularly at Mars); a wake-region flow-field analysis was most likely not included in the design of these other vehicles (figs. 1 to 4). For comparison, the base diameter and reference surface area of the configuration used in this analysis and those described in other recent studies (refs. 2 and 5) are listed in table 5.

Aeroheating calculations. To obtain a preliminary estimate of the total heating environment induced by aerobraking through the Martian atmosphere, both radiative and convective stagnation-point heating calculations were included in this analysis. Both the radiative and convective stagnation-point solutions depend on the effective nose radius of the vehicle. For a vehicle with a high L/D (greater than 1), the nose is roughly spherical, and thus the effective nose radius is equivalent to the actual nose radius. This is not the case for a blunt configuration. For blunt shapes, like Apollo or the AFE, the concept of a single nose radius is rather vague; therefore, an effective nose radius is utilized. The effective nose radius is defined as the radius of an imaginary sphere over which the same shock conditions (in particular, shock standoff distance) would occur. For the Mars aerobrake utilized in this analysis, the effective nose radius (based on AFE data) was either 16.3 m or 20.0 m, depending on the Earth-return mode selected.

To calculate convective heating at the stagnation point, the Sutton-Graves equation was utilized. (See ref. 34.) This equation, which is a correlation of numerically obtained stagnation-point boundary-layer solutions for flows in chemical equilibrium over a range of flight conditions, may be expressed as

$$\dot{q}_{s,\text{conv}} = C(r_n)^{-0.5} \{\rho\}^{0.5} |V_\infty|^3$$

By using this approximate stagnation-point solution, convective heating is treated independently of the rest of the problem; that is, the flow-field and radiative heating solutions. Thus, the effects of radiative absorption and blowing in the boundary layer are not included in this analysis. In the preceding equation, the constant C is a function of the mass fraction, molecular weight, and transport properties of the atmospheric base gases. For the Martian atmospheric composition listed in table 3,

the value of C is 1.90270×10^{-4} kg$^{1/2}$/m, and for the atmosphere of Earth its value is slightly lower, 1.74153×10^{-4} kg$^{1/2}$/m.

Radiative heat transfer is inherently coupled to the flow-field solution. That is, radiative heat transfer depends on the flow-field properties (in particular, density and temperature), which are in turn affected by the radiative intensity. (See ref. 35.) For this reason, a simple correlation analogous to the Sutton-Graves equation for convection does not exist for radiative-heat-rate calculations, and a more complex approach is required. The method used in this analysis to calculate the stagnation-point radiative heat transfer was Sutton's inviscid equilibrium approach. (See ref. 36.) Details of this method are provided in the section "Computational Methods."

By assuming the flow to be inviscid (negligible boundary layer) and in local thermodynamic and chemical equilibrium, a conservative estimate of the radiative heat rate is obtained. For example, in a Pioneer Venus spacecraft analysis that was modeled by a similar atmospheric composition (although the density and entry velocity are higher), the inviscid results were shown to be approximately 30-percent higher than the viscous solution (see ref. 37). Ablative effects, which tend to lower the radiative heat rate through absorption in the boundary layer, are not included in this analysis. For instance, during Earth reentry, this reduction can be on the order of 20 percent to 50 percent (refs. 38 and 39). Therefore, use of this inviscid equilibrium method results in a fairly high preliminary estimate of the stagnation-point radiative heat rate.

Integration of Interplanetary and Mars Atmospheric Trajectories

Details of the interplanetary and atmospheric trajectory simulations have been provided. However, an important aspect of this research is to integrate the trajectories such that a coupled simulation is obtained. In this fashion, the interdependence of the interplanetary and atmospheric trajectory options is established. For example, the effects of a particular interplanetary trajectory selection upon the atmospheric entry conditions and the feasibility of aerobraking can be examined.

This integration is done by patching the two trajectories together at the Mars sphere of influence. Thus, for a specific Earth-Mars transfer, a heliocentric simulation is performed and integrated with the Mars planetocentric simulation. Prior to simulating the Martian atmospheric passage, the vehicle position and velocity vectors relative to Mars must be obtained from the heliocentric data.

The initial velocity vector at Mars' SOI (hyperbolic excess velocity) is obtained by vector subtraction in an analogous method as described in the section "Venus swing-by mode." However, obtaining the initial position vector is not quite as straightforward. At Earth departure, the spacecraft is targeted for the point in space where Mars will be at the end of the outbound transfer. Because two-body motion is assumed, the Sun's gravitational attraction provides the only force that affects the vehicle motion. Thus, from a heliocentric perspective, Mars is reduced to a massless point. At the end of the Earth-Mars transfer, the spacecraft has a certain heliocentric velocity and, therefore (given the velocity vector of Mars), a specific hyperbolic excess velocity. Based on the definition of the hyperbolic excess velocity (the velocity that the spacecraft has above that required to escape the planet's gravitational attraction), the vehicle must be at the edge of the Martian SOI. Furthermore, because in the heliocentric analysis the entire Martian SOI is assumed to be a massless point, the vehicle can be placed at any position on this sphere. Thus, the vehicle initial planetocentric velocity is uniquely defined by the heliocentric trajectory, but its planetocentric position is not. Its planetocentric position remains variable, because any position on the edge of the Mars SOI corresponds to the same heliocentric point in space. This seemingly confusing result is a by-product of the two-body approximation.

Another way to view this problem is to consider an actual mission scenario. Upon Earth departure, Mars and its SOI are so far away that from the vehicle perspective the Martian system does appear as a point. Furthermore, the gravitational attraction of Mars is so small that its influence on the vehicle motion can be ignored. Therefore, very small changes in the Earth-departure velocity translate into major changes in the vehicle arrival position relative to Mars. In this manner, the vehicle can achieve any position on the Martian SOI for approximately the same departure velocity. Because this change in the required departure velocity is insignificant, it is lost in other uncertainties and can be thought of as being part of the midcourse correction sequence.

From an energy standpoint, only the magnitudes of the position and velocity vectors are significant. Therefore, the initial energy of the hyperbolic trajectory at Mars is also uniquely determined by the heliocentric trajectory. Because any initial position on the SOI may be chosen, one might expect it to be possible to achieve any orbital inclination at Mars; however, this is not the case. By defining an orbit's inclination, the vehicle plane of motion is specified. By definition, this plane must contain the vehicle velocity and

position vectors throughout time. Although there are many possible initial position vectors, the problem is restricted to one initial velocity vector. Thus, the plane of motion is defined as the plane containing the vehicle initial velocity vector and one of many possible initial position vectors. Both of these vectors may be defined in terms of magnitude, right ascension, and declination. As demonstrated in reference 40, it is the declination of the initial velocity vector (defined relative to the Mars equatorial plane) that limits the achievable orbital inclination. If the initial velocity vector is characterized by a given declination d, the achievable orbital inclinations are in the following range (ref. 40):

$$d \leq i \leq 180 - d \quad \text{(in degrees)}$$

Therefore, a polar orbit may always be achieved, but an equatorial orbit is not possible for every interplanetary trajectory without the use of either an extra propulsive maneuver or aerodynamic forces. This phenomenon may be extended to Earth return and requires the interplanetary transfer to yield a hyperbolic excess velocity with declination at or below $28.5°$ to rendezvous with the space station (otherwise, a plane-changing maneuver must be performed). However, this is not a difficult constraint for the interplanetary trajectory to satisfy.

Computational Methods

Interplanetary Trajectory Simulation

To specify a particular interplanetary transfer, a specific form of Lambert's problem must be solved. This classic problem refers to the situation in which two position vectors and the time of flight between them are known and either the initial or final velocity vector must be found. At any point in time, knowledge of both the position and velocity vectors uniquely defines the heliocentric trajectory. To simulate the interplanetary portion of this analysis and solve Lambert's problem, the Swing-by Stopover Optimization (SWISTO) program was utilized. (See ref. 41.) The program can simulate a variety of one-way and round-trip interplanetary missions that involve a general-vehicle model capable of performing as many as four impulsive high-thrust maneuvers and one gravitational swing-by. Lambert's problem is solved by using a three-dimensional patched conic approach that iterates upon eccentric anomaly. In this manner, the heliocentric-trajectory legs are determined. With the heliocentric velocity vectors determined, the respective planetocentric vectors (e.g., the hyperbolic excess velocity upon Mars arrival V_{HP}) may be obtained by vector subtraction

as discussed in the section "Venus swing-by mode." Then, for a given Mars parking orbit, this hyperbolic excess velocity V_{HP} may be translated into the periapsis velocity V_p by using the conservation of energy principle. That is,

$$\text{Specific energy} = \text{Constant} = \frac{|V|^2}{2} - \frac{\mu}{|r|}$$

and therefore,

$$|V_p| = \left(|V_{HP}|^2 + \frac{2\mu}{|r_p|} \right)^{1/2}$$

The required value of ΔV is determined by subtracting the required orbital velocity. This is done with the assumption that the arrival maneuver is performed tangential to the velocity vector of the parking orbit periapsis. The values of ΔV at Earth departure, Mars departure, and Earth return may be determined in a similar manner. In an aerobraking scenario, a similar procedure is followed to determine the magnitude of the entry velocity V_{atm} at the atmospheric interface r_{atm}. In this case,

$$|V_{atm}| = \left(|V_{HP}|^2 + \frac{2\mu}{|r_{atm}|} \right)^{1/2}$$

With all the propulsive maneuvers defined by their respective values of ΔV and with the vehicle dry mass known (table 1), the rocket equation may be applied to compute the vehicle propellant requirements and thus the initial vehicle weight in LEO. This equation may be expressed as

$$\Delta V = I_{sp}g \ln \left[\frac{m_i}{m_f} \right] - \begin{array}{l} \text{(Losses due to gravity, drag,} \\ \text{and thrust misalignment)} \end{array}$$

In this analysis, thrust misalignment and drag losses were neglected, and a 5-percent gravity loss was included in the calculations of ΔV.

The heliocentric trajectory optimization process is performed in terms of windows of mission dates; that is, (for a direct mission) a window of possible Earth-departure, Mars-arrival, and Earth-return dates. (For a Venus swing-by mission, a window of Venus swing-by dates is also included.) By specifying a constant 60-day Mars stopover, the Mars-departure dates are implicitly specified by the Mars-arrival window. For convenience, the range of total trip time was divided into 6-month increments (i.e., 1.0 to 1.5, 1.5 to 2.0, and 2.0 to 2.5). For a particular 3-month launch window and subset of total trip times (e.g., 2.0 to 2.5 years), the 3-month Earth-return window is

specified. As shown in figure 31, selecting a bracket of possible stopover dates completely defines both legs of the round-trip trajectory. Unfortunately, there is no general method to determine the optimal position of the stopover bracket or the most efficient length of each trajectory leg. Therefore, a stopover bracket was initially placed fairly close to the Earth-return window. By moving this bracket backward in time toward the Earth-departure window, all the possible trajectories within this total time class can be simulated (fig. 31).

With the use of SWISTO, each window and bracket was subdivided into 20 uniformly spaced increments. Thus, within each 3-month launch window, 20 launch opportunities (1 every 5 days) were defined and all the possible round-trip trajectory combinations were simulated (400 for each launch opportunity, corresponding to the possible combinations of 20 Mars-arrival dates and 20 Earth-return dates). From this, the transfer that resulted in the minimum initial LEO weight was identified. At this point, the most weight-efficient trajectory for the given stopover bracket is known. However, as mentioned previously, this may not be the most efficient placement of the stopover bracket. Thus, the stopover bracket is moved and the process is repeated until all possible trajectories in a particular launch window and within a given total trip-time class are simulated. After moving to the next Earth-departure window, the entire process is repeated. In this manner, LEO launches every 5 days were simulated over a period of 15 years (2010 to 2025) for each of the three sets of total trip time (e.g., 1.0 to 1.5, 1.5 to 2.0, and 2.0 to 2.5 years).

By adding either an inbound or outbound Venus swing-by, the problem becomes even more complex. As shown in figure 32, there are now two brackets whose optimal placement is unknown, and there are three interplanetary legs. This addition creates another dimension to the matrix of data through which SWISTO must sort. Thus, instead of 400 possible transfers, $400 \times N \times M$ transfers were simulated for each launch opportunity and each transfer mode (where N is the number of stopover brackets and M is the number of swing-by brackets). The bounding trajectory cases in terms of hyperbolic excess velocity at both Earth and Mars were identified. These hyperbolic-excess-velocity extrema were translated by using the energy equation to obtain the bounding atmospheric entry conditions in the case of an aerobraking scenario. Bounding estimates were also obtained for the initial required vehicle weight in LEO. Overall, approximately 1.5×10^8 round-trip interplanetary trajectories were simulated.

Atmospheric Trajectory Simulation

The atmospheric passage at Mars was simulated by using the Program to Optimize Simulated Trajectories (POST). This program (ref. 42) was originally written by Martin Marietta in the early 1970's as a Space Shuttle trajectory optimization tool and has since been used to solve a variety of performance problems dealing with ascent, reentry, and orbital maneuvers about a single planetary body. A particular problem is solved by integrating the equations of motion numerically. In a typical problem, there are certain state variables (constraints) that must achieve specific values to insure a successful mission. Any other state variables that are not fixed by the mission requirements (controls) are varied so that the constraints are satisfied. Beginning with the user-input values, POST adjusts the controls until the constraints fall within their prescribed tolerances. The value of each control is modified by first perturbing these variables with respect to each constraint. In this manner, partial derivatives are determined and a weighted-gradient approach is utilized to improve the controls.

The POST is constructed in a modular fashion such that detailed vehicle, planet, and trajectory models are relatively simple to adjust. Although POST has been used to study aerobraking problems before, these problems have generally involved lower energy trajectories; therefore, several modifications were required to complete this study. These modifications included adding viscous aerodynamic effects as a function of Knudsen number, adding convective and radiative stagnation-point heat-rate calculations, and adding the capability to input the initial state in terms of orbital elements for hyperbolic trajectories (previously possible only for closed orbits).

The planetocentric simulation was initiated at the Mars SOI. Neither the initial-position vector (control variables) nor the orbital inclination is specified; however, the problem must start at the edge of the SOI. (Thus, the magnitude of the initial-position vector is a constraint.) The vehicle initially follows a hyperbolic trajectory whose periapsis is at some unknown altitude within the Martian atmosphere. Once in the atmosphere, the vehicle begins to lose energy and its trajectory gradually becomes elliptic. The simulation is concluded as the vehicle exits the atmosphere; at this time, the vehicle must have the proper energy and orbital inclination (two constraint variables) to achieve its specified orbit. Thus, this problem is defined by three constraints (exit energy, exit inclination, and magnitude of the initial-position vector) and three control variables (the three components of the initial-position vector).

Stagnation-Point Radiative Heating

The inviscid equilibrium code, Radiating Inviscid Flow Stagnation Point (RIFSP), discussed in references 36 and 43, was used to calculate the stagnation-point radiative heating during the Mars atmospheric passage. This approach solves a radiatively coupled set of conservation equations for the stagnation streamline by using a time-marching computational scheme. The time-asymptotic technique assumes that the initial values for the flow field are the properties behind a normal shock without radiation. It then follows the development of the flow in an iterative fashion, with periodic updates of the chemistry and radiation properties, until a steady-state solution is achieved.

The radiation model used in this code is an enhanced version of the radiation (RAD) model developed by Nicolet. (See ref. 44.) The effects of molecular-band, atomic-continuum, and atomic-line transitions are included. The frequency variation of the absorption coefficient is taken into account using the line group concept. In this approach, each line in a group is computed in detail, and an integrated absorption coefficient over a finite frequency interval is generated for use in the radiative transport solution. The transport is computed using the tangent-slab approximation, which is valid for the stagnation streamline of a large blunt body such as the one investigated in this study.

Rather than integrating this routine, which requires significant computation time, into POST, a single three-dimensional table was computed and input with each atmospheric trajectory simulation. This table contained the predicted stagnation-point, inviscid, equilibrium, radiative heat rate as a function of density, velocity, and effective nose radius for the atmospheric conditions present at discrete points along a nominal atmospheric pass. (See table 6.) The stagnation-point radiative heat rate along other trajectories was obtained with this table by interpolation.

The atmospheric composition used in these calculations was 97-percent CO_2 and 3-percent N_2, by mass.

Vehicle Packaging

The vehicle was packaged using the Solid Modeling Aerospace Research Tool (SMART), a solid geometry manipulation tool (ref. 45) developed at NASA Langley Research Center. This software package provides the capability to accurately generate and manipulate complex, three-dimensional vehicle geometries. It is user-friendly and operates in a real-time environment. In this investiga-

tion, the component generation, manipulation, shading, and mass distribution options within SMART were utilized. By providing a realistic, interactive, three-dimensional visual capability, this analysis tool greatly enhanced the aerobrake sizing and packaging process.

Initially, SMART was used to create scaled three-dimensional models of the payload elements (the habitation modules, propellant tanks, MEM, and the Earth-return capsule), AFE surface, and subsonic wake region. The payload elements were generated by first creating primitive shapes (i.e., spheres, cones, and cylinders) that were integrated into more complex geometries. These elements were sized according to references 5 and 18. The AFE surface and wake region were generated by creating two-dimensional cross sections that matched the existing models in references 19, 30, and 33. These cross sections were then integrated to form the final three-dimensional surfaces.

Once the individual payload elements were generated, their respective volumes were fixed and they were grouped together. Then, while holding the volume of each payload element constant, the wake region was enlarged until it completely enclosed the required payload. (The required payload was dependent on the Earth-return mode and on the aerobrake that was being packaged—Mars or Earth.) At this point, the payload elements were manipulated to satisfy the vehicle center-of-gravity requirement. This requirement caused the subsonic wake region to be enlarged slightly. When the final configuration was obtained (figs. 29 and 30), the size of the AFE wake region was utilized to specify a minimum aerobrake size. Although figures 29 and 30 are orthogonal, SMART may also be used to create three-dimensional perspective views.

Results and Discussion

Interplanetary Trajectory Simulation

The interplanetary portion of this analysis was simulated so that not only the potential types of Earth-Mars transfers, but also the characteristics associated with each type of trajectory, could be identified. For a direct mission (Earth-Mars-Earth) with a total trip time between 1.0 and 1.5 years, the variations in entry velocities and vehicle weight ratios are shown in figures 33(a) and 33(b), respectively, as a function of LEO launch date. Figure 33(a) shows the variation in atmospheric entry velocity at Earth and Mars. This is the inertial velocity at either 122 or 76 km altitude for Earth and Mars. In figure 33(b), the minimum vehicle weight ratio W_i/W_f is shown. This ratio represents the minimum mass that must be

initially placed in LEO for every kilogram of payload returned to LEO at the end of the mission.

In all of the interplanetary trajectory results, the weight ratios are given for the all-propulsive option, which returns the habitation modules and truss structure to LEO (propulsive option, Earth-return mode 1). As an example, a vehicle sized for a trip of 1.0 to 2.0 years has a mass of 6.1×10^4 kg at Earth return (table 1). Thus, a W_i/W_f of 20.0 would require an initial LEO mass of 1.22×10^6 kg. The weight ratio of the other all-propulsive option, which returns only a crew capsule (propulsive option, Earth-return mode 2), is slightly lower and is not discussed until the section "Atmospheric Entry Conditions." (The initial LEO weight of the aerobraking option is also presented in the section "Atmospheric Entry Conditions.")

For each 3-month launch window, in which at least one mission is possible, data are shown in figure 33(a) that represent the limits on atmospheric entry velocity for any direct mission of 1.0 to 1.5 years. Also, the most efficient trajectory from a weight standpoint within each 3-month launch window is denoted in figure 33(b). Launch dates for which no data appear indicate a period in which the vehicle could not accomplish the mission because of a poor planetary alignment. For example, in the years 2010 and 2011 a direct mission of 1.0 to 1.5 years cannot be performed by this class of vehicle.

Direct mode. As mentioned previously, figure 33 is illustrative of a direct mission of 1.0 to 1.5 years. A close look at this figure shows the effect of the 26-month synodic variation discussed previously; that is, the data are grouped together in potential launch opportunities that are separated by approximately 26 months. Furthermore, the effect of the longer 15- to 17-year variation is also evident. These figures show that careful launch-date selection is not only important to assure a low weight ratio, but also to provide an acceptable Earth-reentry velocity. The extreme variation in Earth-reentry velocity versus launch date (11.5 to 21.0 km/sec) should be noted. In a high-thrust interplanetary mission, the minimum Earth-reentry speed (assuming a parabolic entry trajectory and an atmospheric interface of 122 km altitude) is approximately 11.1 km/sec. Unlike the Earth-reentry velocities, the Mars-entry velocities remain within a fairly narrow range (5.8 to 11.0 km/sec). The minimum Mars-entry speed is approximately 5.1 km/sec (assuming a parabolic entry transfer and an atmospheric interface of 76 km).

A wide range of weight ratios from as low as 50 to as high as 800 appear (fig. 33(b)). Because a Mars mission that requires a large initial LEO weight

may be too costly to perform, a maximum vehicle weight ratio of 100 was selected as a constraint in all subsequent work. As shown in figure 33(b), weight-efficient trajectories were defined as those characterized by vehicle weight ratios below 50.0. The results illustrated in figure 33 closely match those from reference 46.

With the inclusion of the weight ratio limit (i.e., $W_i/W_f \leq 100$), the 1.0- to 1.5-year direct mission scenario was reevaluated and the results are shown in figure 34. As seen in the figure, only a few missions are now practical. However, those missions that remain feasible also tend to have lower Earth-entry velocities (11.5 to 17.0 km/sec).

Trajectory characteristics of a very efficient direct mission class (2.0 to 2.5 years long) are illustrated in figure 35. A chemically propelled direct mission of this length yields low vehicle weight ratios over much of the 15-year launch span (fig. 35(b)) and results in a greater frequency of achievable mission opportunities. Because only the effect of the 26-month cycle is represented in the entry conditions, the atmospheric entry velocity becomes less date-dependent (fig. 35(a)). Although the Earth-reentry speeds still range from 11.5 to 16.5 km/sec, fairly low entry velocities can be achieved at least once every 26 months (as opposed to once every 15 to 17 years for the 1.0- to 1.5-year direct transfer). Also, within each mission opportunity, a wider launch window exists over which low Earth-reentry velocities are attainable.

These advantageous trajectory characteristics appear at the expense of an increased trip time. For the inverted direct mission (fig. 13), an increased total trip time allows the vehicle to follow a longer, but more energy-efficient, outbound transfer to Mars before a near-Hohmann inbound transfer is performed. For a short (1.0- to 1.5-year) direct mission, this was not the case. Accomplishing an inbound near-Hohmann trajectory required a very quick inefficient outbound trajectory, which resulted in a large vehicle weight ratio. The Mars-entry velocities for the 2.0- to 2.5-year round trip, which range from 5.5 to 12.0 km/sec, vary in a fairly regular manner, similar to those of the shorter trip.

From a weight standpoint, a mission of 2.0 to 2.5 years is the most practical of all the direct transfer modes studied. The majority of the weight ratios in this mission class are less than 50.0, and many are less than 20.0. Also, because the high number of launch opportunities uniformly spans the entire 15-year cycle, mission flexibility is increased. The efficiency of this mission class is reflected in the fact that in the 1.5- to 2.0-year class transfer, the optimal trajectories were clustered about the 1.9- to 2.0-year

range. Furthermore, when a few missions in the 2.5- to 3.0-year class were simulated, the optimal trajectories were all 2.5 to 2.6 years long. Because the results of the 1.5- to 2.0-year round-trip transfers were similar to the 2.0- to 2.5-year case in figure 35, they are not shown.

Although direct missions within this time class (2.0 to 2.5 years) are characterized by low weight ratios, they are considered rather long for an initial excursion type of manned Mars mission. However, the 2.0- to 2.5-year direct transfers are well suited for a Mars base strategy. If such a base exists or is being assembled, this mission may be flown by a number of vehicles in approximate 26-month cycles. Such a scenario could be used as the basis for personnel transfer and cargo exchange. For this strategy, the 2.0- to 2.5-year mission is the most weight-efficient opposition-class mission. However, if a longer mission time is not a significant factor, the 2.5- to 3.0-year conjunction class missions (which were not studied in this analysis) may be a more suitable option because of the longer Mars staytime and lower required initial LEO weight. (See ref. 11.)

Inbound Venus swing-by mode. In the inbound swing-by trajectory mode (Earth-Mars-Venus-Earth), the mission is generally composed of an efficient near-Hohmann outbound leg and a decelerating Venus swing-by prior to Earth return. The results of the 1.0- to 1.5-year mission cases are presented in figure 36. The effect of involving a third celestial body is immediately made evident by the relatively sparse number of possible missions. However, compared with the 1.0- to 1.5-year direct transfers, inclusion of an inbound Venus swing-by has resulted in both a lower weight ratio (as low as 22) and reduced Earth-reentry velocities. (Compare figs. 34 and 36.) The majority of these missions include Earth-reentry velocities less than 14.0 km/sec, whereas the Mars-entry velocity varies over essentially the same range as in the direct mode (6 to 10 km/sec).

The data in figure 37 illustrate the results from the 1.5- to 2.0-year inbound swing-by mode. Although not shown, most of these missions are of 1.6 to 1.8 years in duration. Compared with the 1.0- to 1.5-year case, approximately twice as many missions are possible. Furthermore, these missions are characterized by low Earth-reentry velocities and even lower weight ratios than the 1.0- to 1.5-year mission (as low as 16). Figure 37(a) shows that although the Earth-reentry speed varies from 11.5 to 15.0 km/sec, most of the possible missions include a reentry velocity in the low end of that range. The Mars-entry velocity varies over roughly the same range as noted previously (5.5 to 10.0 km/sec). Figure 37(b) shows that

a possible mission exists near each celestial opposition, or on a cycle of approximately 21 to 30 months. These results correlate well with those of reference 11.

The results of inbound swing-by missions of 2.0 to 2.5 years are presented in figure 38. A swing-by mission requires the optimization of three interplanetary legs, and, because three efficient legs that also total 2.0 to 2.5 years are difficult to achieve, fewer possible missions within this time class exist. Those that are shown tend to be 1.9 to 2.1 years long; thus, results similar to those in figure 38 are depicted. Once again, the missions are characterized by low Earth-reentry speeds (11.5 to 14.0 km/sec), steady Mars-entry velocities (6.0 to 9.0 km/sec), and fairly low weight ratios (as low as 40.0).

When all possible inbound swing-by missions are compared without regard to flight time, an interesting feature is noted. In contrast to the direct mode, the longest swing-by missions are not necessarily the most efficient from a weight standpoint. In a majority of the launch opportunities in which the 1.5- to 2.0-year mission was possible, it was the most efficient type of inbound swing-by transfer. Most of the 1.5- to 2.0-year inbound swing-by missions include a vehicle weight ratio under 50, and a few are characterized by a weight ratio under 20. Although not as frequent as the 2.0- to 2.5-year direct transfers, these missions do span the entire 15-year cycle and are well suited to the initial manned excursion strategy.

Outbound Venus swing-by mode. In the outbound swing-by trajectory mode (Earth-Venus-Mars-Earth), the mission is generally composed of a short transfer to Mars with an accelerating Venus swing-by and an efficient near-Hohmann inbound leg. The results of the 1.0- to 1.5-year case are illustrated in figure 39. The Earth-reentry velocities range from 11.5 to 14.5 km/sec, whereas the Mars-entry speeds range from 8 to 12 km/sec. Furthermore, these missions could be accomplished with weight ratios as low as 27.0. These results are similar in trend to the inbound transfers of the same time class (fig. 36).

The next set of data, shown in figure 40, illustrates the results from the 1.5- to 2.0-year outbound swing-by mode. As with the inbound swing-by mode, the majority of these missions are clustered about the 1.6- to 1.8-year time frame, and, when compared with the 1.0- to 1.5-year outbound case, approximately twice as many missions are possible. These outbound swing-by missions are characterized by low to midrange Earth-reentry velocities (11.5 to 16.5 km/sec) and very low weight ratios (as low as 17.0). The Mars-entry speeds range from 8 to 12 km/sec. These results also correlate well with reference 11. For reasons similar to those

18

discussed in the section "Inbound Venus swing-by mode," the missions of 2.0 to 2.5 years are difficult to achieve. The few that were successfully performed ranged from 1.9 to 2.1 years and could be grouped with the 1.5- to 2.0-year class mission. These results are not shown.

As in the case of the inbound swing-by mission scenario, the 1.5- to 2.0-year outbound swing-by mission is the most efficient from a weight standpoint. These missions not only span the entire 15-year cycle, but do so in a manner that complements the existing inbound swing-by launch dates. Therefore, when the inbound and outbound missions are combined, the total range of launch opportunities for a 1.0- to 2.0-year initial-excursion-class mission is nearly doubled.

Efficient exploration strategies. From the interplanetary results presented, two efficient opposition-class transfer modes have emerged: the 2.0- to 2.5-year direct transfer, and the 1.0- to 2.0-year Venus swing-by transfer. Both of these transfer modes result in efficient opposition-class transfers to Mars. However, each is better suited for a particular mission strategy. The 1.0- to 2.0-year Venus swing-by mission is well suited for the initial-excursion-class mission, while the longer, direct mission is a better choice for the Mars base approach.

Figure 41 shows the minimum weight ratio possible as a function of trip time, transfer mode, and braking method. Because this weight parameter is of major significance to the mission planner, it is important that, regardless of the braking method, the minima in this figure correspond to each of the strategies discussed. For the longer mission scenario (2.0 to 2.5 years), the proper launch-date choice is not critical; for this trajectory class, an efficient transfer exists over the entire 15-year time span. These missions are characterized by not only low weights, but also low entry velocities. On the other hand, the shorter, 1.0- to 2.0-year Venus swing-by mission scenarios are more date dependent. Although inclusion of both inbound and outbound swing-by modes allows the range of potential launch dates to span the entire 15-year period, the launch opportunities are neither as frequent nor as long.

Launch Opportunities

At this point in the analysis, a subset of the previously discussed interplanetary trajectories was identified. The limiting characteristics of this group of transfers were selected such that modest advances in technology are required. Ideally, the mission planner would like to minimize the required initial weight in LEO, the Earth- and Mars-entry velocities,

and the total trip time. Maximizing the number of possible launch opportunities and the length of each opportunity is also desired. Unfortunately, all these trajectory characteristics cannot be satisfied by a given set of transfers; therefore, trade-offs must be made.

Because this investigation is directed towards the initial-excursion-class mission, for which a short trip time is desired, further study was limited to trajectories with trip times under 2.0 years. A maximum vehicle weight ratio of 50.0 was also established as a constraint on the trajectory efficiency. Because the aerothermal environment at Earth return is generally thought of as more severe than at Mars arrival (as noted by the larger and more varied range of potential Earth-reentry velocities), the trajectories were limited to an Earth-reentry velocity below 12.5 km/sec. Because the Mars-entry velocity varies in a relatively benign fashion, no restrictions were placed on this parameter. Finally, a minimum launch opportunity of 20 days was imposed on the analysis.

As shown in figure 42, 11 potential mission opportunities exist that adhere to the four defined constraints. One of these opportunities is based on a direct transfer, whereas the others are roughly split between the inbound and outbound Venus swing-by modes. Although not continuous, these mission opportunities do span the entire 15-year period of LEO launch dates. In this figure, the size of each LEO launch period is given in days. Figure 42 defines the launch opportunities for a subset mission class within the initial excursion scenario. Any trajectory contained within this subset is characterized as (1) being efficient from a weight standpoint ($16.1 \leq W_i/W_f \leq 50.0$), (2) having a low Earth-return entry velocity ($11.44 \leq V_{atm} \leq 12.47$ km/sec), (3) having a total trip time of 1.0 to 2.0 years (as low as 1.2 years), and (4) having a LEO launch period of at least 20 days (maximum of 192 days). Also, the Mars-entry velocity varies between 6.11 and 9.90 km/sec. These trajectory characteristics are summarized in table 7.

Atmospheric Entry Conditions

The range of atmospheric flight conditions encountered by the trajectories just described is shown in figure 43 at both Earth and Mars. By using a Venus swing-by, the entry conditions at Earth are generally below 14.0 km/sec. (See ref. 8.) However, by careful selection of the interplanetary trajectory at the mission planning stage, entry is limited to the shaded regions of the figure (below 12.5 km/sec at Earth return). By maintaining an entry velocity as low as possible, the structural and thermal requirements placed on the aerobrake system are reduced. This reduction is an example of the influence that

the interplanetary trajectory selection has on the technical systems required to support an aerobraking mission.

Because the Mars-entry velocity is not considered a mission-enabling criterion, it is not constrained. As a result, this parameter varies over a fairly wide range (table 7). Of the 11 launch opportunities (fig. 42), the four inbound swing-by missions are characterized by Mars-entry velocities from 6.11 to 9.20 km/sec, while the six outbound swing-by missions are characterized by a slightly higher range of Mars-entry conditions (7.38 to 9.90 km/sec). This discrepancy exists because an outbound swing-by is generally used to accelerate the Earth-Mars transfer leg (thereby increasing the Mars-entry velocity), whereas an inbound swing-by uses an energy-efficient near-Hohmann transfer for the Earth-Mars leg.

At Mars arrival, the vehicle consists of payload, structure, two aerobrakes, and the Mars-departure propellant and tankage (figs. 29 and 30). For a fixed payload and structural configuration, weight variations in the two aerobrakes and Mars-departure propellant requirements affect the vehicle ballistic coefficient. As the spacecraft ballistic coefficient increases, the vehicle tends to fly lower in the Martian atmosphere. (See ref. 27.) As a result of flying through a more dense atmospheric region, the aerothermal environment becomes more severe and is another example of the effect that the interplanetary trajectory has on the feasibility of Mars aerocapture.

For the trajectories within the 11 launch opportunities, the ΔV requirement of Mars departure (calculation presented in the section "Interplanetary Trajectory Simulation") varies from 0.905 km/sec to 5.055 km/sec. The Earth and Mars aerobrakes were assumed to weigh 15 percent of the weight that is inserted into orbit; thus, the weight of the Earth aerobrake depends on the Earth-return option chosen. Referring to aerobrake Earth-return mode 1 as the option in which the habitation modules are returned to LEO and to aerobrake Earth-return mode 2 as the option in which only a small crew capsule is returned to LEO, table 8 lists the four combinations used to bound the vehicle weight at Mars arrival. This table also lists the required size of each Mars aerobrake to protect its cargo (see section "Vehicle Packaging") and the resulting ballistic coefficients. The Mars-arrival ballistic coefficient varies from 136.0 kg/m^2 (aerobake Earth-return mode 1, ΔV = 0.905 km/sec) to 376.2 kg/m^2 (aerobrake Earth-return mode 2, ΔV = 5.055 km/sec). In this analysis, three ballistic coefficient configurations were simulated; these configurations corresponded to the two extreme values and a midrange value of

276.9 kg/m^2 (aerobrake Earth-return mode 1, ΔV = 5.055 km/sec).

Mars Atmospheric Trajectory Simulation

The Mars planetocentric simulation begins as the vehicle enters the planet SOI on a hyperbolic path. Because the COSPAR atmospheric models include high-altitude data, the atmospheric interface is specified at an altitude of 300 km during the atmospheric simulation. In the interplanetary simulation, an interface altitude of 76 km was specified because most of the vehicle deceleration occurs below this altitude. This variation in entry altitude has a minor effect on the calculated entry velocity (a variance on the order of 2 percent). For a successful aeromaneuver, the vehicle flight path is elliptic at atmospheric exit with an apoapsis altitude of 3.2972 × 10^4 km and an inclination of 90°. When apoapsis is reached, a minor propulsive maneuver is performed to raise the orbit periapsis to 500.0 km in altitude. Rather than arbitrarily selecting entry velocities between 6 and 10 km/sec, the atmospheric simulation was based upon the interplanetary trajectories that included either an Earth- or Mars-entry velocity extrema, the minimum initial vehicle weight, or the minimum total trip time. This practice provided a realistic, complete trajectory depiction of the particular trajectory scenarios of interest to the mission planner. For example, of all the interplanetary trajectories simulated, the minimum Earth-entry velocity of 11.44 km/sec was achieved by an outbound Venus swing-by mission that departs LEO in October 2021 (Julian date of 2459504) on a round-trip transfer of 1.40 years (table 9). Because this trajectory is characterized as achieving the lowest Earth-reentry velocity, it is of interest to the mission planner. Therefore, the corresponding Mars-entry velocity of 9.46 km/sec is chosen as a potential entry condition for the atmospheric trajectory simulation. The characteristics of this transfer and the others that correspond to extreme interplanetary trajectory conditions are listed in table 9.

Atmospheric entry of a vehicle with a midrange ballistic coefficient. With the entry conditions provided in table 9, the Mars atmospheric passage was simulated using POST. The results of this simulation for a ballistic coefficient of 276.9 kg/m^2 are presented in table 10; performance data along both the entry corridor boundaries are included. As illustrated in figure 44, a full lift-up passage encounters a higher deceleration than the corresponding full lift-down trajectory; thus, maximum deceleration is partially a function of bank

angle. Furthermore, as the Mars-entry velocity is increased, the vehicle maximum encountered deceleration increases. This increased deceleration occurs because, as the entry velocity increases, the vehicle is required to deplete a larger amount of velocity in only a slightly longer period of time.

As the entry velocity increases, the full lift-up trajectory exceeds a $5g$ deceleration for an entry velocity of approximately 7.3 km/sec. Below this speed, the entry corridor is bound by the full lift-up and full lift-down trajectories; however, for entry velocities above 7.3 km/sec, the entire corridor is not considered flyable and the lower corridor bound is specified by a constant bank-angle trajectory that achieves $5g$. As shown in figure 44, the minimum possible deceleration for a given entry velocity is achieved by flying a full lift-down trajectory that (for any entry velocity below 10 km/sec) does not exceed the imposed $5g$ constraint. However, if a lower deceleration limit had been selected (e.g., $3g$), Mars entry above 8.5 km/sec would not be possible for a vehicle with this L/D. Because an entry-velocity limit would restrict the number of possible Earth-Mars interplanetary transfers, it is important that the interplanetary and atmospheric trajectories are not examined independently, but in an integrated manner.

The entry corridor, as defined by the atmospheric-interface flight-path angle, is shown in figure 45. The entry corridor increases in width with entry velocity until the full lift-up trajectory reaches the $5g$ limit at 7.3 km/sec. At this point, the flyable entry corridor achieves its maximum width of 0.93° in flight-path angle. As the entry velocity increases above 7.3 km/sec, the flyable corridor begins to narrow because of the $5g$ constraint. Therefore, as the entry velocity increases, the flyable corridor initially increases, achieves its maximum value when the full lift-up trajectory encounters $5g$, and then decreases in width.

As shown in figure 45, the achievable aerodynamic corridor continues to increase in width with entry velocity. Because this achievable corridor is defined as the corridor limited by the full lift-up and full lift-down trajectories, its bounds are aerodynamically determined and are not constrained to meet an imposed deceleration limit. Physically, the increase in the possible aerodynamic corridor size with entry velocity is a result of requiring the vehicle to lose more energy as its entry velocity is increased, such that it reaches the specified conditions upon atmospheric exit. To achieve this exit velocity at increasing entry velocities, the vehicle must remain in the atmosphere longer, thereby exerting more aerodynamic control over its flight path. (See section "Entry-corridor definition.") A similar result may be obtained by altering the specified capture orbit and thereby altering the required energy loss. (See ref. 29.) Thus, the entry corridor size is affected by atmospheric conditions as well as interplanetary requirements such as the Mars-arrival velocity and the selected exit orbit.

When the interplanetary guidance requirements are placed on the entry corridor, the range of entry velocities for a successful aerocapture is restricted. As shown in figure 45, the maximum corridor width is 0.93° at an entry velocity of 7.3 km/sec. If the guidance requirements associated with the MRSR mission are assumed (minimum 1.0° corridor width, 3-σ accuracy), high-energy aerobraking at Mars is not feasible for a low L/D vehicle like the configuration modeled in the present study. Furthermore, because this result is valid over the entire range of entry velocity, a low L/D Mars aerobrake is not feasible regardless of the interplanetary transfer chosen. This limitation can be alleviated by allowing the vehicle to generate more aerodynamically induced control. To accomplish this, either the vehicle L/D must be increased, or an exit orbit that requires a greater energy loss must be selected. Of the two proposed techniques, the second method will result in increased deceleration and increased aerothermal environment. Therefore, if the guidance errors on the order of those associated with the MRSR mission are assumed, the vehicle L/D must be increased.

If measurements obtained from the optical navigation system can be utilized until entry, aerobraking at Mars with this vehicle is feasible from a navigation standpoint, but the corridor is restricted to entry below 8.6 km/sec (fig. 46). This estimate of navigation error (minimum 0.5° corridor width, 3-σ accuracy) does not incorporate the effects of atmospheric, midcourse correction or trim angle-of-attack uncertainties. Inclusion of these error sources could drive the 0.5° corridor width to approximately 0.8° and will further limit the allowable entry-velocity range. (See ref. 28.) Increasing the minimum allowable corridor width creates an interesting effect. If the minimum required corridor width is above 0.51° (the corridor width for entry at 5.95 km/sec), the entry-velocity envelope is restricted from both ends of the velocity range. As shown in figure 46, imposing a 0.8° guidance constraint requires the entry velocities to be between 6.6 and 7.8 km/sec. Therefore, in general, not only does a maximum entry velocity exist (above which the $5g$ constraint yields a corridor width that is too small), but a minimum entry velocity also exists (below which the vehicle cannot exert enough aerodynamic control over its trajectory).

These entry-velocity restrictions imposed by the interplanetary guidance requirements impact the total number of potential missions. As shown in figure 47, several of the launch windows that met the imposed interplanetary requirements (fig. 42) do not adhere to a minimum corridor width of 0.5°; therefore, these missions are not possible in an aerobraking scenario that utilizes a low L/D shape at Mars. Also, several other launch windows have been reduced in size. This situation becomes worse as the guidance requirements increase (fig. 48), until no interplanetary trajectory possibilities remain for a required corridor width above 0.93°, as in the MRSR scenario. Hence, the width of the flyable entry corridor is another factor that affects the selection of a complete trajectory. Because a Mars-entry velocity constraint was not applied to the interplanetary analysis (in which minimum LEO weight was the primary concern), more trajectories than those shown in figures 47 and 48 actually exist; however, these trajectories require the vehicle initial LEO weight to be significantly increased.

Also listed in table 10 are the maximum stagnation-point heat rates for various entry velocities (including both convective and radiative effects). For this configuration, which is characterized by an effective nose radius of 20 m, the aerothermal environment varies from negligible to approximately 360 W/cm^2. In general, a reusable heat shield (ref. 27) is not feasible for a heat rate above 50 W/cm^2; therefore, the majority of these atmospheric passages require either an ablative thermal protection system or some form of active cooling (e.g., transpiration cooling). As shown in figure 49, for a vehicle with a given ballistic coefficient, the maximum stagnation-point heat rate is largely a function of entry velocity. Some minor control over the magnitude of the stagnation-point heat rate can be achieved by varying the bank angle and thus flying in a different atmospheric region; however, the primary factor affecting the maximum achieved heat rate is entry velocity.

Figures 50 to 52 show the relative roles of convective and radiative heating in the total stagnation-point heat-rate picture. As shown in figure 50, the heating is almost completely the result of convection (only 4 percent of the total heat rate may be attributed to the radiative shock layer) at an entry velocity of 5.95 km/sec. However, as shown in figure 51 for an entry velocity of 7.08 km/sec, the radiative effects account for approximately 53 percent of the maximum total heat rate. At an entry velocity of 9.79 km/sec (fig. 52), the radiative effects dominate the aerothermal environment, which has become about 84 percent radiative. Because radiative heating increases more rapidly than convective heating

with velocity, when the radiative contribution to the total heat rate becomes significant, the aerothermal environment can become relatively severe.

If entry is limited to less than 8.6 km/sec (by the most optimistic guidance requirements), the maximum stagnation-point heat rate is below 190 W/cm^2 (depending on the precise entry velocity and the selected bank angle). Therefore, over a majority of the entry corridor, either an ablative heat shield or an active cooling system is warranted. If a reusable thermal protection system (TPS) is a mission constraint, the number of mission opportunities is significantly reduced to those characterized by a Mars-entry velocity below 6.7 km/sec. The opportunities that meet the 0.5° corridor width constraint and experience very little radiative heating are shown in figure 53. If a required corridor width of 0.8° is included as a mission constraint, addition of the reusable TPS requirement severely limits the number of possible mission opportunities. That is, the majority of missions that allow a reusable TPS (entry below 6.7 km/sec) do not meet the minimum corridor requirements imposed by guidance inaccuracies (entry between 6.6 and 7.8 km/sec). Hence, a reusable TPS mission constraint severly hampers mission flexibility.

Atmospheric entry of a vehicle with a high ballistic coefficient. Performance data obtained by simulating the atmospheric passage of a vehicle with a ballistic coefficient of 376.2 kg/m^2 are listed in table 11. When the vehicle maximum encountered deceleration is examined, a striking similarity to the vehicle with the midrange ballistic coefficient is apparent. (See fig. 44.) Once again, the full lift-up trajectory reaches the 5g constraint for an entry velocity of approximately 7.3 km/sec. Therefore, as in the simulations with a midrange ballistic vehicle, the entry corridor is bound by the full lift-up and full lift-down cases as long as the entry velocity is below 7.3 km/sec. Above this limiting entry velocity, the corridor is bound by the full lift-down and 5g constraining trajectories.

Figure 54 shows the resulting entry corridor in terms of the flight-path angle at the Martian atmospheric interface. In comparison to figure 46, the size of the entry corridor has not been changed (to within 0.01°) by increasing the vehicle ballistic coefficient. Once again, the entry corridor increases in width until its maximum value of 0.93° (for an entry velocity of 7.3 km/sec) is reached; as the entry velocity is increased above 7.3 km/sec, the corridor narrows as a result of the imposed 5g limit. The shape of this curve is similar in trend to that in figure 46; however, the two curves differ in the magnitude of γ_{atm}. For the same entry conditions, a

vehicle with a higher ballistic coefficient decelerates in a lower atmospheric region; therefore, the entry flight-path angle is steeper (more negative). The fact that the vehicle is flying deeper into the atmosphere is shown by comparing the minimum altitude columns in tables 10 and 11.

Because the two corridors in figures 46 and 54 are approximately the same width, the use of a higher ballistic coefficient has not altered the interplanetary guidance restrictions imposed on entry velocity. Thus, only missions that yield the acceptable range of Mars-entry velocities (below 8.6 km/sec for the 0.5° corridor width) should be considered feasible (fig. 47). In the same manner, if a 0.8° corridor width is required, the entry velocity must be between 6.6 and 7.8 km/sec (mission opportunities shown in fig. 48). Once again, if a flight-path-angle tolerance on the order of that used by the MRSR program is a constraint (minimum 1.0° corridor width), this configuration is not a feasible Mars aerobrake shape.

As mentioned previously, a vehicle with a higher ballistic coefficient decelerates deeper into the atmosphere, and therefore, into a more dense atmospheric region. This configuration ($S = 700$ m^2) is slightly smaller than the midrange ballistic coefficient configuration ($S = 1060$ m^2), which would tend to decrease the radiative contribution to the total heat rate while slightly increasing the convective heat rate. However, the effect of this small change in nose radius is relatively minor compared with the effect of density on the stagnation-point heat rate. As shown in figure 55, the maximum stagnation-point heat rate for this configuration varies from negligible to approximately 550 W/cm^2. Compared with figure 49, the encountered heat rate increases substantially with ballistic coefficient. Once again (see table 11), the heating is mainly convective at the lower entry velocities but gradually becomes radiative until these effects dominate at the higher entry velocities. Furthermore, when the atmospheric passage is limited by either set of guidance constraints (to velocities below 8.6 km/sec or between 6.6 and 7.8 km/sec), an ablative heat shield is required over the majority of the remaining entry conditions. A reusable TPS would restrict the entry-velocity envelope to below 6.7 km/sec where radiative effects are negligible. Once again, this constraint does not mesh well with either set of guidance requirements; this incompatibility causes a significant reduction in the number of possible missions.

Atmospheric entry of a vehicle with a low ballistic coefficient. The performance data obtained by simulating the atmospheric trajectories for a vehicle with a ballistic coefficient of 136.0 kg/m^2

are listed in table 12. Once again, when the maximum encountered deceleration is examined, similar results to those presented in tables 10 and 11 are obtained (fig. 44). As shown in figure 56, the full lift-up trajectory for this configuration reaches the 5g constraint for an entry velocity of 7.3 km/sec. Therefore, over the entire range of possible ballistic coefficients, the corridor is bounded by the full lift-up and full lift-down cases for any entry velocity below 7.3 km/sec. Above this velocity, the flyable entry corridor is only a portion of the achievable corridor and is bounded by the full lift-down and 5g limiting trajectories. Although this aerobrake configuration decelerates higher in the atmosphere, the trajectory periapsis is still in the continuum flow regime; therefore, transitional and free-molecular effects are minimal for Martian aerocapture.

By decelerating higher in the atmosphere, the aerothermal environment is reduced such that it varies from being negligible to approximately 130 W/cm^2 (fig. 57). As with the midrange ballistic coefficient, this vehicle has an effective nose radius of 20 m; however, a comparison of figures 49 and 57 shows that the maximum stagnation-point heat rate experienced by this less-massive configuration is greatly reduced. Once again, convective effects dominate the thermodynamic environment at lower velocities, whereas radiative effects become significant at the higher entry velocities. However, as is evident from table 12, the radiative contribution to the total stagnation-point heat rate is not as strong as in the other two cases that decelerate in denser regions of the Martian atmosphere.

For entry velocities below 8.6 km/sec (as dictated by the most optimistic navigation requirements), the maximum heat rate is below 85 W/cm^2. Furthermore, if a reusable aerobrake TPS is a mission requirement, a lower ballistic coefficient configuration allows a broader range of entry velocities to be considered. In this case, the entry-velocity envelope is below 7.6 km/sec, which is a substantially different thermodynamic scenario than in the midrange and high ballistic coefficient cases (where an ablative surface was required over all entries above 6.7 km/sec). Compared with figure 53, a wider range of mission opportunities exists that can meet this Mars-entry-velocity constraint ($V_{atm} < 7.6$ km/sec); these mission opportunities are presented in figure 58. However, the number of possible missions is still significantly lower than if an ablative aerobrake is used. This same effect is noted if the 0.8° corridor constraint is imposed. That is, a broader overlap exists between the navigation requirements (entry between 6.6 and 7.8 km/sec) and the TPS constraints (entry below 7.6 km/sec). Thus, a low ballistic

coefficient configuration experiences an aerothermal environment in which a reusable thermal protection system may be used over a slightly broader range of entry conditions than with the midrange or high ballistic coefficient. However, based on guidance considerations, requiring a reusable TPS may still be a major constraint upon the total number of allowable missions. Furthermore, because the ballistic coefficient (defined as $m/C_D S$) is a function of both the interplanetary (m) and atmospheric trajectories (S and C_D), it is another means by which these two trajectories are coupled.

Effect of ballistic coefficient on atmospheric passage. In this investigation, a relatively wide range of ballistic coefficients was simulated during the Mars aerocapture. Because of the Mars-departure propulsive requirements (which vary with interplanetary trajectory between 0.905 and 5.055 km/sec), the ballistic coefficient ranged from 136.0 to 376.2 kg/m^2. As shown in figure 44, the maximum deceleration is not significantly affected by the range of ballistic coefficients that are applicable to a manned Mars mission (the greatest variation is $0.06g$ or 0.588 m/sec^2). To further illustrate this point, a particular atmospheric trajectory was simulated (full lift-down, $V_{atm} = 9.79$ km/sec) over a wider range of ballistic coefficients (i.e., $m/C_D S = 2769.0$, 276.9, and 27.69 kg/m^2). As shown in figures 59 and 60, the three vehicle configurations follow different atmospheric flight paths while losing the same amount of velocity. However, because the atmospheric passage times are approximately the same (to within 50 sec in 700), the maximum encountered decelerations are approximately equal. Hence, for a low L/D vehicle, if the aerobraking maneuver involves a fixed velocity decrement, the maximum deceleration is mainly specified by velocity and bank angle, not ballistic coefficient.

The effect of ballistic coefficient on the entry-corridor width is also minimal. The ballistic coefficient does not affect the corridor size, because all three vehicle configurations ($m/C_D S = 136.0$, 276.9, and 376.2 kg/m^2) achieve a majority of the required deceleration under continuum flow conditions. Hence, transitional and free-molecular aerodynamic effects are of minor importance in a Mars aerobraking analysis. This result is shown in figure 61, which superimposes the entry corridors of figures 46, 54, and 56.

Although the entry-corridor width is unaffected by ballistic coefficient, its placement in the atmosphere is largely a function of this parameter. For a given flight condition (fig. 61), as the ballistic coefficient is increased, the entry flight-path angle

becomes steeper (more negative); therefore, the vehicle decelerates at lower altitudes. Thus, the ballistic coefficient is largely responsible for the encountered atmospheric density profile. By influencing the encountered density regime, the ballistic coefficient significantly affects the severity of the encountered aerothermal environment. This fact is evident when figures 49, 55, and 57 are compared. In this analysis, the effective nose radius was held fairly constant (between 16.3 and 20 m). Thus, the major influence of the ballistic coefficient on the maximum stagnation-point heat rate is the specification of the density regime. In addition to controlling the magnitude of the total heat rate, the ballistic coefficient affects the relative contributions of the radiative and convective heat rates. However, the significance of radiative and convective heating in the stagnation region is also a function of the atmospheric entry velocity.

As the entry velocity increases, the maximum stagnation-point heat rate increases, as does the relative contribution of the radiative effects; this result is shown in figure 62. In this figure, the fraction of the total maximum heat rate due to radiative effects is plotted versus entry velocity for each of the three ballistic-coefficient configurations. It is evident that at very low Mars-entry velocities (below 6.2 km/sec), the aerothermal environment may be assumed to be purely convective regardless of ballistic coefficient. That is, the radiative effects account for less than 20 percent of the total heat rate. However, as the entry velocity is increased, the significance of radiative heating varies with ballistic coefficient. For entry of a configuration with a high ballistic coefficient, radiation is the source of at least 80 percent of the total heat rate at entry velocities above 8.5 km/sec; for a midrange ballistic coefficient, this is not true until the entry velocity is above 9.0 km/sec. For the low ballistic coefficient, radiative effects never dominate the aerothermal environment (radiation never accounts for 80 percent or more of the total heat rate).

One of the objectives of this analysis was to establish some general guidelines for the type of heating present in the stagnation region of a large, blunt vehicle aerobraking at Mars. For an aerobrake configuration consistent with the requirements of a manned Mars mission, the magnitude of the aerothermal environment and the type of heating present at the stagnation point are functions of both entry velocity and ballistic coefficient. General guidelines can be established as to the significance of including convective and radiative calculations in the heating analysis. These guidelines should not be taken as rigidly defined rules, but rather as an estimate of the relative effects of radiative and convective heating

during Mars aerocapture. As listed in table 13, these guidelines are dependent upon ballistic coefficient. Also, the magnitudes of the convective and radiative stagnation-point heat rates are presented along with the potential atmospheric flight domain in figure 63. From figures 62 and 63, it is clear that unless the atmospheric passage is performed at a very low entry velocity (below 6.2 km/sec), the effects of radiation should be included in the stagnation-region flow-field analysis. As the entry velocity is increased, the radiative effects dominate the aerothermal environment. Because interplanetary missions with a Mars-entry velocity below 6.2 km/sec are relatively sparse and are limited in corridor width, the effect of radiation on the total heat rate should not be neglected in Mars aerobraking studies that utilize a large, blunt shape.

Comparison of Propulsive and Aerobraking Options

If no constraint is placed on the type of Mars aerobrake TPS, the possible mission scenarios (those that meet the interplanetary and atmospheric entry constraints) are shown in figure 47 for a minimum corridor width of 0.5°. To compare the initial LEO weight saved by aerobraking at Mars, the most weight-efficient propulsive trajectory was identified within each launch window. For each of these trajectories, the required LEO weight in an aerobraking scenario was calculated. Table 14 shows the weight comparison for the two Earth-return modes. As demonstrated in figure 41, the aerobraking missions require a significantly lower initial LEO weight. This weight reduction ranges from 19 percent to 59 percent and is shown graphically for each of the two Earth-return modes in figures 64(a) and 64(b). In addition to reducing the required initial LEO weight, aerobraking upon Mars arrival tends to lower the variance in initial weight and provide increased mission flexibility (table 14).

From these results it is evident that the most efficient propulsive mission is not necessarily the most efficient aerobraking mission. In a propulsive option, the optimal trajectory is the one that minimizes the initial LEO weight based on four major burns. For a specific planetary alignment, the most weight-efficient trajectory may require relatively large Earth- and Mars-departure burns compared with the Mars-arrival and Earth-return ΔV requirements. On the other hand, under the constraints of a different planetary alignment, the most efficient trajectory may utilize relatively large Mars-arrival and Earth-return burns compared with the departure requirements.

In an aerobraking scenario, the Mars-arrival and Earth-return propulsive requirements are assumed to be negligible. Thus, the most weight-efficient trajectory is the one that minimizes the initial LEO weight based on the departure burns only; in general, this trajectory does not correspond to the most weight-efficient all-propulsive trajectory. Therefore, in an aerobraking scenario, to obtain the optimal mission based on initial weight considerations, the interplanetary optimization process must be altered. This is another example of the interdependency of the interplanetary and atmospheric trajectory characteristics in a mission that features high-energy aerobraking.

Conclusions

Manned Mars missions departing low-Earth orbit (LEO) in the time frame 2010 to 2025 were analyzed to identify preferred mission opportunities and the associated vehicle and trajectory characteristics. Two chemically propelled vehicle options were considered: (1) an all-propulsive configuration, and (2) a configuration that employs aerobraking at Earth and Mars with low lift-drag (L/D) shapes. The major findings of this investigation are as follows:

1. *Two distinct types of weight-efficient Mars mission strategies have been identified.* These strategies are a 1.0- to 2.0-year mission that generally involves the use of a Venus swing-by and a 2.0- to 2.5-year direct transfer. Efficient transfers as short as 1.2 years were found; however, most of the swing-by missions are clustered about 1.6 to 1.8 years in total trip time. Because of its cyclic nature, the 2.0- to 2.5-year direct scenario is applicable to an interplanetary program that has a permanently manned Mars base as its goal, whereas the 1.6- to 1.8-year Venus swing-by transfer is better suited for the initial manned exploration of Mars.

2. *Eleven 1.0- to 2.0-year round-trip mission opportunities were identified between 2010 and 2025.* The interplanetary transfers within each opportunity are characterized by a vehicle weight ratio W_i/W_f below 50. Also, these transfers are characterized by relatively low Earth-return velocities (11.5 to 12.5 km/sec) and Mars-entry velocities between 6.0 and 10.0 km/sec. Although these launch opportunities are neither as frequent nor as wide as for the longer transfers, a major portion of the 15-year launch-date cycle is spanned.

3. *A low L/D Mars aerobrake configuration (L/D $\leq$ 0.28) is not feasible without substantial improvements in the interplanetary navigation system.* If the present Mars Rover Sample Return (MRSR) navigation tolerance is selected as a mission constraint (minimum 1.0° corridor width, 3-σ accuracy), this study shows that, regardless of entry velocity, a low L/D vehicle cannot exert enough control authority to be considered feasible. Hence, a hypersonic L/D

significantly greater than 0.28 is required for Mars aerocapture.

4. *Even with a reduction in the interface flight-path-angle error, aerodynamic requirements significantly restrict the number of mission opportunities.* Whether this reduction is achieved through advanced technology or the use of optical measurements until just prior to entry, a low L/D shape is only feasible over a limited range of entry conditions because of the effect of the $5g$ limit incorporated in this study for physiological concerns. The extent of this entry-velocity restriction depends on the increase in navigation accuracy achieved. Mars entry was shown to be restricted to velocities below 8.6 km/sec for a minimum corridor width of 0.5° and to velocities between 6.6 km/sec and 7.8 km/sec for a minimum corridor width of 0.8°.

5. *For a large, blunt Mars aerobrake configuration, radiative heating is a significant issue.* These effects should not be neglected in a Mars aerocapture thermodynamic analysis unless the entry velocity is very low. Depending on the ballistic coefficient, the radiative contribution to the total stagnation-point heat rate can be significant for entry velocities as low as 6.2 km/sec. Furthermore, the stagnation-point aerothermal environment may become dominated by radiative effects (at least 80 percent of the total heat rate due to radiation) at entry velocities as low as 8.5 km/sec.

6. *The large stagnation-point heat rates associated with radiative heating dictate the use of an ablative or actively cooled thermal protection system (TPS) for a majority of the Mars aerocapture maneuvers.* If the mission profile includes the use of a reusable TPS, the range of allowable entry velocities is significantly reduced. The extent of this restriction is largely a function of ballistic coefficient. For ballistic coefficients of 276.9 kg/m^2 and 376.2 kg/m^2, use of a reusable TPS required the entry velocity to be below 6.7 km/sec. However, because entry at such a low velocity does not allow the vehicle much corridor width, this constraint does not mesh well with guidance requirements. This problem is partially alleviated by use of a lower ballistic-coefficient configuration. For a ballistic coefficient of 136.0 kg/m^2, entry was limited to below 7.6 km/sec; thus, a slightly larger overlap existed between thermal and guidance requirements. However, use of such a low ballistic coefficient is not generally possible while achieving an efficiently packaged vehicle configuration.

7. *In an aerobraking scenario, the mission and optimization process must be altered to include the integrated interplanetary and atmospheric trajectory effects.* By defining the range and variation of en-

try velocities at both Earth and Mars, the possible variance of these velocities has been shown to be a significant concern. For example, when the transfer is properly chosen, a weight-efficient trajectory with entry-condition ranges as low as 6.0 to 7.0 km/sec at Mars arrival and 11.5 to 12.5 km/sec upon Earth return may be achieved. On the other hand, a poor trajectory choice may result in Mars-entry speeds as high as 13.0 km/sec or an Earth-reentry velocity as high as 18.0 km/sec. This investigation has also shown that the interplanetary transfer influences the atmospheric flight path by specifying the Mars-arrival weight and thus affecting the ballistic coefficient. Conversely, the atmospheric trajectory places constraints upon the interplanetary transfer. These restrictions limit the allowable entry velocity and stem from: (1) an imposed maximum deceleration requirement, (2) a minimum corridor-width requirement, and (3) TPS requirements. Therefore, if the benefits associated with high-energy aerobraking are featured in a mission scenario, the relationship between the interplanetary and atmospheric trajectories must be included at the mission planning stage, and the optimization process must be altered based on whether the mission is purely propulsive or features aerobraking.

In summary, by substantially reducing the required initial LEO weight, aerobraking is an attractive feature of manned Mars missions. Compared with an all-propulsive configuration, the use of aerobraking at Mars entry and Earth reentry resulted in initial LEO weight savings as high as 59 percent. The variance in initial LEO weight is also lowered and thereby provides mission flexibility. However, by including aerobraking in the mission profile, several additional requirements that pertain to the atmospheric passage must be satisfied. Finally, based on near-term technology, an aerobrake configuration with a hypersonic L/D higher than 0.28 is required for Mars aerocapture.

References

1. National Commission on Space: *Pioneering the Space Frontier—An Exciting Vision of Our Next Fifty Years in Space.* Bantam Books, Inc., May 1986.

2. Ride, Sally K.: *Leadership and America's Future in Space—A Report to the Administrator.* NASA, Aug. 1987.

3. Babb, Gus R.; and Stump, William R.: Comparison of Mission Design Options for Manned Mars Missions. *Manned Mars Missions*, NASA TM-89320, 1986, pp. 37–52.

4. Braun, Robert D.; and Blersch, Donald J.: Propulsive Options for a Manned Mars Transportation System. AIAA-89-2950, July 1989.

5. Tucker, Michael; Meredith, Oliver; and Brothers, Bobby: Space Vehicle Concepts. *Manned Mars Missions*, NASA TM-89320, 1986, pp. 316–341.

6. Young, Archie C.: Mission and Vehicle Sizing Sensitivities. *Manned Mars Missions*, NASA TM-89320, 1986, pp. 87–102.

7. Walberg, Gerald D.: A Survey of Aeroassisted Orbit Transfer. *J. Spacecr. & Rockets*, vol. 22, no. 1, Jan. Feb. 1985, pp. 3–18.

8. Walberg, Gerald D.: *A Review of Aerobraking for Mars Missions*. Paper No. IAF-88-196, Oct. 1988.

9. Jones, Jim J.: The Rationale for an Aeroassist Flight Experiment. AIAA-87-1508, June 1987.

10. Clark, Benton C.: Manned Mars Missions: Perspectives and Options. AIAA-90-0001, Jan. 1990.

11. Young, Archie C.; Mulqueen, John A.; and Skinner, James E.: *Mars Exploration, Venus Swingby and Conjunction Class Mission Modes, Time Period 2000 to 2045*. NASA TM-86477, 1984.

12. Roberts, Barney B.: A Transportation System for Routine Visits to Mars. *Vol. 71 of American Astronautical Soc. Science and Technology Series*, Duke B. Reiber, ed., Univelt, Inc., c.1988, pp. 433–453. (Available as AAS 86-174.)

13. Welch, Steven: Mission Strategy and Spacecraft Design for a Mars Base Program. *Vol. 62 of American Astronautical Soc. Science and Technology Series*, Christopher P. McKay, ed., Univelt, Inc., c.1985, pp. 345–375. (Available as AAS 84-169.)

14. French, James R.: The Impact of Martian Propellant Manufacturing on Early Manned Exploration. *Vol. 62 of American Astronautical Soc. Science and Technology Series*, Christopher P. McKay, ed., Univelt, Inc., c.1985, pp. 519 526. (Available as AAS 84-178.)

15. Hoffman, Stephen J.; McAdams, James V.; and Niehoff, John C.: Round Trip Trajectory Options for Human Exploration of Mars. *Vol. 69 of American Astronautical Soc. Advances in the Astronautical Sciences*, Jerome Teles, ed., Univelt, Inc., c.1989, pp. 663 679. (Available as AAS 89-201.)

16. Babb, Gus R.; and Stump, William R.: Mars Orbit Selection. *Manned Mars Missions*, NASA TM-89320, 1986, pp. 78–86.

17. Langley Research Center Staff: *A Report on the Research and Technological Problems of Manned Rotating Spacecraft*. NASA TN D-1504, 1962.

18. Stump, William R.; Babb, Gus R.; and Davis, Hubert P.: Mars Lander Survey. *Manned Mars Missions*, NASA TM-89320, 1986, pp. 239 251.

19. Cheatwood, F. McNeil; DeJarnette, Fred R.; and Hamilton, H. Harris, II: *Geometrical Description for a Proposed Aeroassist Flight Experiment Vehicle*. NASA TM-87714, 1986.

20. Bate, Roger R.; Mueller, Donald D.; and White, Jerry E.: *Fundamentals of Astrodynamics*. Dover Publications, Inc., 1971.

21. Sohn, Robert L.: Venus Swingby Mode for Manned Mars Missions. *J. Spacecr. & Rockets*, vol. 1, no. 5, Sept. Oct. 1964, pp. 565–567.

22. Deerwester, Jerry M.: Initial Mass Savings Associated With the Venus Swingby Mode of Mars Round Trips. AIAA Paper No. 65-89, Jan. 1965.

23. Sohn, Robert L.: Manned Mars Trips Using Venus Swingby Modes. *Third Manned Space Flight Meeting*, American Inst. of Aeronautics & Astronautics, Nov. 1964, pp. 330–338.

24. Striepe, Scott A.; and Braun, Robert D.: Effects of a Venus Swingby Periapsis Burn During an Earth-Mars Trajectory. Paper AAS 89-426, American Astronautical Soc., Aug. 1989.

25. Kwok, Johnny H.; and Friedlander, Alan: Mars Rover and Sample Return Mission Design. Paper AAS 89-198, American Astronautical Soc., Apr. 1989.

26. Chapman, Dean R.: *An Analysis of the Corridor and Guidance Requirements for Supercircular Entry into Planetary Atmospheres*. NASA TR R-55, 1960.

27. Hill, Oliver; and Wallace, Rodney O.: Manned Mars Mission Vehicle Design Requirements for Aerocapture. *Manned Mars Missions*, NASA TM-89320, 1986, pp. 114–128.

28. Willcockson, Bill: Application of Aeroassist to the Mars Rover Sample Return Mission. *Vol. 69 of American Astronautical Soc. Advances in the Astronautical Sciences*, Jerome Teles, ed., Univelt, Inc., c.1989, pp. 625 650. (Available as AAS 89-199.)

29. Brand, Timothy J.; Fuhry, Douglas P.; and Shepperd, Stanley W.: An Onboard Navigation System Which Fulfills Mars Aerocapture Guidance Requirements. AIAA-89-0629, Jan. 1989.

30. Wells, William L.: *Measured and Predicted Aerodynamic Coefficients and Shock Shapes for Aeroassist Flight Experiment (AFE) Configuration*. NASA TP-2956, 1990.

31. Celenligil, M. Cevdet; Moss, James N.; and Blanchard, Robert C.: Three-Dimensional Flow Simulation About the AFE Vehicle in the Transitional Regime. AIAA-89-0245, Jan. 1989.

32. Bird, G. A.: *Molecular Gas Dynamics*. Oxford Univ. Press, 1976.

33. Gnoffo, Peter A.: A Code Calibration Program in Support of the Aeroassist Flight Experiment. AIAA-89-1673, June 1989.

34. Sutton, Kenneth; and Graves, Randolph A., Jr.: *A General Stagnation-Point Convective-Heating Equation for Arbitrary Gas Mixtures*. NASA TR R-376, 1971.

35. Anderson, John D., Jr.: *Hypersonic and High Temperature Gas Dynamics*. McGraw-Hill Book Co., 1989.

36. Sutton, Kenneth: Characteristics of Coupled Nongray Radiating Gas Flows With Ablation Product Effects About Blunt Bodies During Planetary Entries. Ph.D. Thesis, North Carolina State Univ. at Raleigh, 1973. (Available as NASA TM X-72078.)

37. Moss, James N.; Zoby, E. Vincent; Sutton, Kenneth; and Anderson, E. Clay: A Study of the Aerothermal Environment for the Pioneer Venus Multiprobe Mission. AIAA Paper No. 77-766, June 1977.

38. Wilson, K. H.: Massive Blowing Effects on Viscous, Radiating, Stagnation-Point Flow. AIAA Paper No. 70-203, Jan. 1970.

39. Moss, James N.: Radiative Viscous-Shock-Layer Solutions With Coupled Ablation Injection. *AIAA J.*, vol. 14, no. 9, Sept. 1976, pp. 1311-1317.

40. Tolson, Robert H.: *Geometrical Characteristics of Lunar Orbits Established From Earth-Moon Trajectories.* NASA TN D-1780, 1963.

41. Mead, Charles W.; and Jones, Max F.: *Optimization of "Ephemeridal" Parameters for Minimum Propellant Requirements on Multiplanet Roundtrip Swingby-Stopover Missions.* TM 54/30-189, LMSC/HREC A791436 (Contract NAS8-20082), Lockheed Missiles & Space Co., May 1968.

42. Bauer, G. L.; Cornick, D. E.; and Stevenson, R.: *Capabilities and Applications of the Program To Optimize Simulated Trajectories (Post).* NASA CR-2770, 1977.

43. Sutton, Kenneth: Coupled Nongray Radiating Flow About Ablating Planetary Entry Bodies. *AIAA J.*, vol. 12, no. 8, Aug. 1974, pp. 1099-1105.

44. Nicolet, William E.: *Advanced Methods for Calculating Radiation Transport in Ablation-Product Contaminated Boundary Layers.* NASA CR-1656, 1970.

45. McMillin, M. L.; Rehder, J. J.; Wilhite, A. W.; Schwing, J. L.; Spangler, J.; and Mills, J. C.: A Solid Modeler for Aerospace Vehicle Preliminary Design. AIAA-87-2901, Sept. 1987.

46. Pritchard, E. Brian: Velocity Requirements and Re-Entry Flight Mechanics for Manned Mars Missions. *J. Spacecr. & Rockets*, vol. 1, no. 6, Nov.-Dec. 1964, pp. 605-610.

Table 1. Vehicle Component Dry-Mass Estimate

Vehicle component	Mass for 1- to 2-year round-trip mission, kg	Mass for 2- to 2.5-year round-trip mission, kg
2 habitation modules (ref. 5)	50×10^3	57×10^3
Truss structure and support equipment	11	14
Lab module (ref. 5)	...	16
MEM* (refs. 5 and 18)	76	100
Probes	—	7
Outbound payload	137×10^3	194×10^3
Terminal payload	61	87
$m_{\text{dropped at Mars}}$	76	107

*Sized for operation from 500 km × 32 972 km orbit, Inclination = 90°.

Table 2. Celestial Data

Parameter	Sun	Earth	Mars	Venus
Equatorial radius, km	696 000	6 378	3 380	6 187
Gravitational parameter, km^3/s^2	1.327×10^{11}	3.986×10^5	4.305×10^4	3.257×10^5
Mass relative to Earth	333 432	1	0.108	0.817
Mean distance from Sun, km	—	1.495×10^8	2.278×10^8	1.081×10^8
Sphere-of-influence radius, km	—	9.235×10^5	5.777×10^5	6.159×10^5
Mean orbital speed, km/sec	—	29.79	24.14	35.04
Atmospheric interface altitude, km	—	121.92	300.00	—
Rotation rate, rad/sec	—	7.2722×10^{-5}	7.07763×10^{-5}	—

Table 3. Mars Atmospheric Properties

Composition,* percent mass:

CO_2	96.68
N_2	1.74
Ar	1.47
O_2	0.11

Mean molecular weight, kg/kg-mole 43.54
Average γ 1.2966
Nominal molecular diameter (ref. 32), m . . . . . 4.64 $\times 10^{-10}$

*A 97% CO_2, 3% N_2 composition was assumed in radiative heating calculations.

Table 4. Interplanetary Guidance-System Performance

System	3-σ error in Mars-entry flight-path angle
Earth-based radio tracking (ref. 28)	$\pm 1.8°$
Earth-based radio tracking supplemented by optical sightings of Deimos until 2 hours prior to entry (ref. 29)	$\pm 0.5°$
Earth-based radio tracking supplemented by optical sightings of Deimos until entry (ref. 29)	$\pm 0.25°$

Table 5. Aerobrake Size Comparison Survey

Parameter	This study	MSFC* (fig. 1)	SAIC* (fig. 2)	Boeing[†] (fig. 3)	MMC[‡] (fig. 4)
Mars aerobrake surface area, m^2	700.0 or 1060.0	460.0	460.0	485.0	2498.3
Mars aerobrake base diameter, m	30.0 or 37.0	24.4	24.4	25.0	56.4
Earth aerobrake surface area, m^2	18.5 or 395.0	460.0	102.0	380.0	34.6
Earth aerobrake base diameter, m	4.9 or 22.9	24.4	11.4	22.2	6.64

* No artificial gravity provided.
† Provides varied level or artificial gravity with use of tethers.
‡ Provides $1g$ artificial gravity by spinning entire aerobrake system.

Table 6. Stagnation-Point, Inviscid, Equilibrium, Radiative Heat Rates

Altitude, km	Density, kg/m^3	V_{atm}, km/sec	r_n, m	$\dot{q}_{s,rad}$, W/m^2
30.00	9.80×10^{-4}	4.50	10	1.301×10^2
		4.50	20	2.388×10^2
		6.15	10	1.286×10^5
		6.15	20	2.071×10^5
		8.00	10	3.898×10^6
		8.00	20	5.951×10^6
39.66	3.56×10^{-4}	4.50	10	2.094×10^1
		4.50	20	3.994×10^1
		6.51	10	2.035×10^5
		6.51	20	3.193×10^5
		8.20	10	1.233×10^6
		8.20	20	1.867×10^6
43.72	2.31×10^{-4}	4.50	10	9.426
		4.50	20	1.820×10^1
		6.65	10	1.644×10^5
		6.65	20	2.504×10^5
		8.39	10	8.291×10^5
		8.39	20	1.193×10^6
52.00	8.85×10^{-5}	4.50	10	1.563
		4.50	20	3.065
		6.20	10	1.718×10^4
		6.20	20	2.398×10^4
		9.80	10	6.390×10^5
		9.80	20	8.528×10^5
62.11	2.55×10^{-5}	4.50	10	1.490×10^{-1}
		4.50	20	2.960×10^{-1}
		6.28	10	6.198×10^3
		6.28	20	9.326×10^3
		9.85	10	1.108×10^5
		9.85	20	1.921×10^5
68.28	1.15×10^{-5}	4.50	10	3.290×10^{-2}
		4.50	20	6.560×10^{-2}
		6.00	10	5.529×10^2
		6.00	20	9.148×10^2
		9.90	10	3.221×10^4
		9.90	20	5.712×10^4
73.89	5.43×10^{-6}	4.50	10	7.930×10^{-3}
		4.50	20	1.580×10^{-1}
		6.00	10	2.272×10^2
		6.00	20	3.964×10^2
		9.90	10	9.278×10^3
		9.90	20	1.643×10^4

<p align="center">Table 7. Entry Condition During Launch Windows</p>

Approximate calendar launch window	First launch date, Julian	Launch window, days	Minimum W_i/W_f	Earth-reentry velocity* Min, km/sec	Earth-reentry velocity* Max, km/sec	Mars-entry velocity[†] Min, km/sec	Mars-entry velocity[†] Max, km/sec
Direct mode							
2016.75 to 2017.00	2457663	20	27.9	11.70	11.70	8.33	8.99
Inbound swing-by mode							
2016.00 to [‡]2016.25	2457395	90	35.3	12.20	[§]12.47	7.79	9.20
2020.50 to [‡]2020.75	2459032	70	21.6	12.33	12.33	6.15	6.96
2013.75 to 2014.25	2456521	[§]192	[§]16.1	11.66	12.04	6.13	7.58
2020.00 to 2020.50	2458865	167	19.1	11.96	12.20	[§]6.11	7.52
Outbound swing-by mode							
2011.00 to [‡]2011.25	2455546	26	30.7	11.84	11.90	7.67	7.98
2021.75 to [‡]2022.00	2459499	40	42.5	[§]11.44	11.47	9.45	[§]9.90
2023.75 to [‡]2024.00	2460219	25	26.7	11.94	11.94	8.22	8.51
2011.00 to 2011.25	2455511	35	25.2	11.83	11.90	7.60	8.15
2017.00 to 2017.50	2457819	81	17.0	11.55	11.90	7.38	9.73
2023.50 to 2023.75	2460178	41	21.8	11.50	11.93	8.03	8.53

* Velocity at 122-km altitude.

[†] Velocity at 76-km altitude.

[‡] Total trip time 1 to 1.5 years; otherwise total trip time 1.5 to 2.0 years.

[§] Extrema.

<p align="center">Table 8. Range of Ballistic Coefficients</p>

Earth-return mode	Mars-departure ΔV requirements, km/sec 0.095 $m_{\text{aerobraked}}$ (at Mars), kg	Mars-departure ΔV requirements, km/sec 0.095 Ballistic coefficient, kg/m^2	Mars-departure ΔV requirements, km/sec 5.055 $m_{\text{aerobraked}}$ (at Mars), kg	Mars-departure ΔV requirements, km/sec 5.055 Ballistic coefficient, kg/m^2	Mars aerobrake reference area, m^2
Mode 1 (Earth-return aerobrake)	195.0×10^3	136.0	398.0×10^3	276.9	1060.0
Mode 2 (Earth-return capsule)	182.0×10^3	192.0	357.0×10^3	376.2	700.0

Table 9. Extrema Trajectory Characteristics

Trajectory extrema	LEO launch date, Julian (calendar)	Interplanetary transfer mode	Total trip time, years	W_i/W_f	Mars-entry velocity,[*] km/sec	Earth-reentry velocity,[†] km/sec
Minimum weight in LEO	2456617 (11/2013)	Inbound Venus swing-by	1.74	16.1	6.31	11.96
Minimum Mars-entry velocity	2458966 (5/2020)	Inbound Venus swing-by	1.71	19.4	6.11	11.96
Maximum Mars-entry velocity	2459539 (11/2021)	Outbound Venus swing-by	1.30	49.5	9.90	11.45
Minimum Earth-reentry velocity	2459504 (10/2021)	Outbound Venus swing-by	1.40	46.9	9.46	11.44
Maximum Earth-reentry velocity	2457439 (2/2016)	Inbound Venus swing-by	1.32	35.7	7.81	12.47
Minimum total trip time, including 60-day stopover	2457479 (4/2016)	Inbound Venus swing-by	1.20	46.7	8.03	12.47

[*] Velocity at 76-km altitude.
[†] Velocity at 122-km altitude.

Table 10. Mars Atmosphere Passage Simulation Data
for Midrange Ballistic Coefficient (276.9 kg/m^2)

Entry velocity,[*] km/sec	Corridor bound	γ_{atm}, deg	G_{max}, g units	Minimum altitude, km	Maximum heat rate,[†] W/cm^2	Major heat class
5.95	Lift-up	−17.91	1.76	41.18	13.26	Conv
	Lift-down	−17.40	1.00	46.25	10.13	Conv
6.15	Lift-up	−18.28	2.11	39.66	15.98	Conv
	Lift-down	−17.68	1.14	45.34	11.89	Conv
7.68	5g	−19.84	5.01	34.15	105.77	Both
	Lift-down	−19.12	2.41	41.67	61.86	Both
9.79	5g	−20.13	5.04	38.17	363.64	Rad
	Lift-down	−20.06	4.46	39.36	318.18	Rad
Additional data points						
7.08	Lift-up	−19.60	4.29	34.54	70.81	Both
	Lift-down	−18.67	1.90	42.75	36.76	Both
7.37	5g	−19.83	5.00	33.74	86.50	Both
	Lift-down	−18.91	2.15	42.18	42.91	Both
8.48	Lift-down	−19.56	3.14	40.55	112.23	Both

[*] Inertial velocity at 300-km altitude.
[†] $r_n = 20.0$ m.

Table 11. Mars Atmosphere Passage Simulation Data
for High Ballistic Coefficient (376.2 kg/m^2)

Entry velocity,* km/sec	Corridor bound	γ_{atm}, deg	G_{max}, g units	Minimum altitude, km	Maximum heat rate,[†] W/cm^2	Major heat class
5.95	Lift-up	−18.01	1.75	38.46	16.97	Conv
	Lift-down	−17.49	1.00	43.58	12.85	Conv
6.15	Lift-up	−18.37	2.13	36.99	20.69	Conv
	Lift-down	−17.78	1.16	42.72	14.95	Conv
7.68	5g	−19.94	5.03	31.37	123.55	Both
	Lift-down	−19.22	2.38	38.84	71.98	Both
9.79	5g	−20.24	5.04	35.25	556.41	Rad
	Lift-down	−20.17	4.50	36.66	451.57	Rad

* Inertial velocity at 300-km altitude.
[†] $r_n = 16.3$ m.

Table 12. Mars Atmosphere Passage Simulation Data
for Low Ballistic Coefficient (136.0 kg/m^2)

Entry velocity,* km/sec	Corridor bound	γ_{atm}, deg	G_{max}, g units	Minimum altitude, km	Maximum heat rate,[†] W/cm^2	Major heat class
5.95	Lift-up	−17.68	1.78	47.42	10.91	Conv
	Lift-down	−17.20	1.03	52.27	8.18	Conv
6.15	Lift-up	−18.04	2.16	45.96	9.14	Conv
	Lift-down	−17.48	1.17	51.42	7.01	Conv
7.68	5g	−19.55	5.05	40.81	58.78	Both
	Lift-down	−18.90	2.44	47.84	26.07	Both
9.79	5g	−19.89	5.04	44.43	130.00	Both
	Lift-down	−19.03	4.55	45.73	112.74	Both
Additional data points						
7.08	Lift-up	−19.34	4.47	40.96	38.72	Both
	Lift-down	−18.46	1.91	48.80	17.27	Both
7.38	5g	−19.55	5.00	40.34	51.80	Both
	Lift-down	−18.69	2.16	48.29	21.19	Both

* Inertial velocity at 300-km altitude.
[†] $r_n = 20.0$ m.

Table 13. Entry-Velocity* Guidelines for Stagnation-Point Heating Analysis

$$[r_n = 20 \text{ m}]$$

Ballistic coefficient, kg/m²	Convective heating dominates,[†] km/sec	Both are important, km/sec	Radiative heating dominates,[‡] km/sec
Low (136.0)	$V_{atm} \leq 6.5$	$V_{atm} > 6.5$	—
Mid (276.9)	$V_{atm} \leq 6.3$	$6.3 < V_{atm} < 9.0$	$V_{atm} \geq 9.0$
High (376.2)	$V_{atm} \leq 6.2$	$6.2 < V_{atm} < 8.5$	$V_{atm} \geq 8.5$

* Inertial velocity at 300-km altitude.
† Less than 20 percent radiative effects.
‡ Greater than 80 percent radiative effects.

Table 14. Minimum Mass Trajectories Within Each Launch Opportunity

[Includes navigation constraints, fig. 64]

Approximate calendar launch window	LEO launch date, Julian	Trip time, years*	Initial LEO mass, kg × 10⁶, for—			
			Mode 1 (Earth-return aerobrake)		Mode 2 (Earth-return capsule)	
			All-propulsive	Aero-braking	All-propulsive	Aero-braking
Inbound swing-by mode						
2016.00 to 2016.25	2457395	1.33	2.17	0.89	1.61	0.80
2020.50 to 2020.75	2459032	1.49	1.33	.91	1.02	.82
2013.75 to 2014.25	2456521	1.74	.99	.71	.82	.65
2020.00 to 2020.50	2458865	1.61	1.17	.83	.96	.75
Outbound swing-by mode						
2011.00 to 2011.25	2455546	1.49	1.88	0.97	1.46	0.88
2023.75 to 2024.00	2460219	1.49	1.64	.74	1.40	.68
2011.00 to 2011.25	2455511	1.58	1.55	.81	1.30	.74
2017.00 to 2017.50	2457819	1.61	1.05	.56	.91	.52
2023.75 to 2023.75	2460178	1.58	1.34	.65	1.16	.60

* Includes a 60-day Mars stopover.
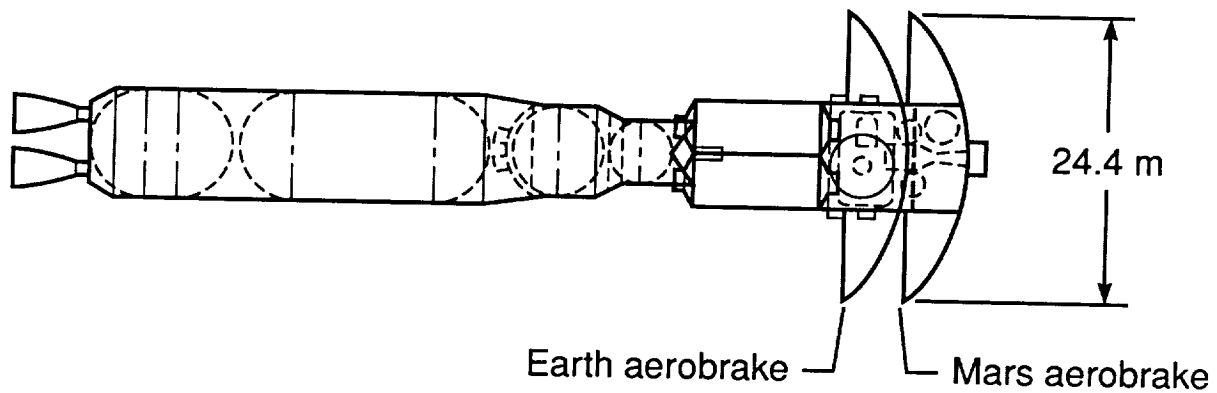
Figure 1. MSFC conceptual design of a manned Mars vehicle (ref. 5). Aerobrake dimensions listed in table 5.
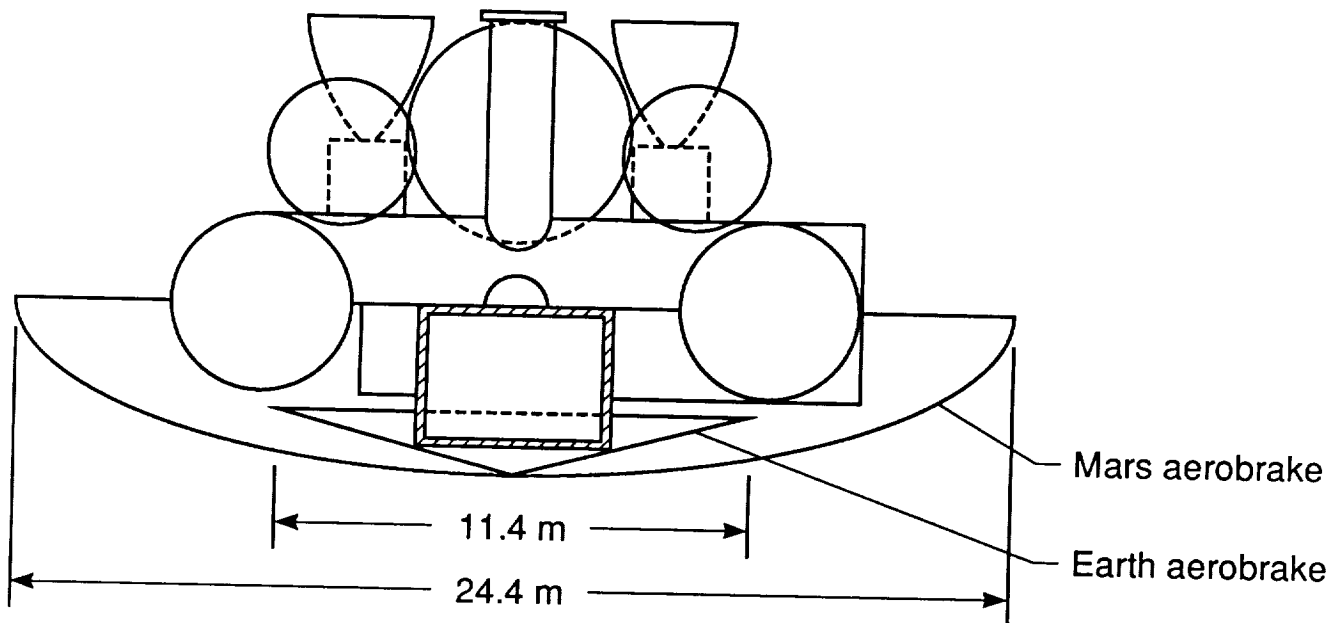
Figure 2. SAIC conceptual design of a manned Mars vehicle (ref. 2). Aerobrake dimensions listed in table 5.

22.2 m 25.0 m

Mars and Earth aerobrake — ⌐ └ — Mars aerobrake
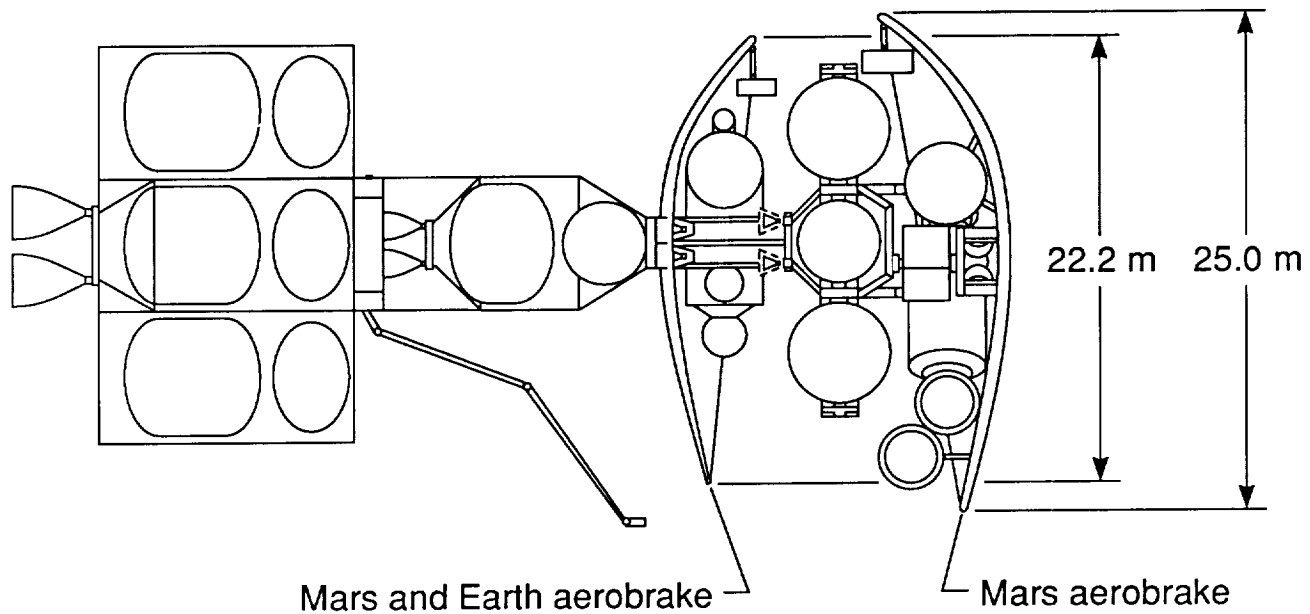
Figure 3. Boeing conceptual design of a manned Mars vehicle. Aerobrake dimensions listed in table 5.

Earth-return capsule ⌐

⌐ Mars aerobrake

← 56.4 m →
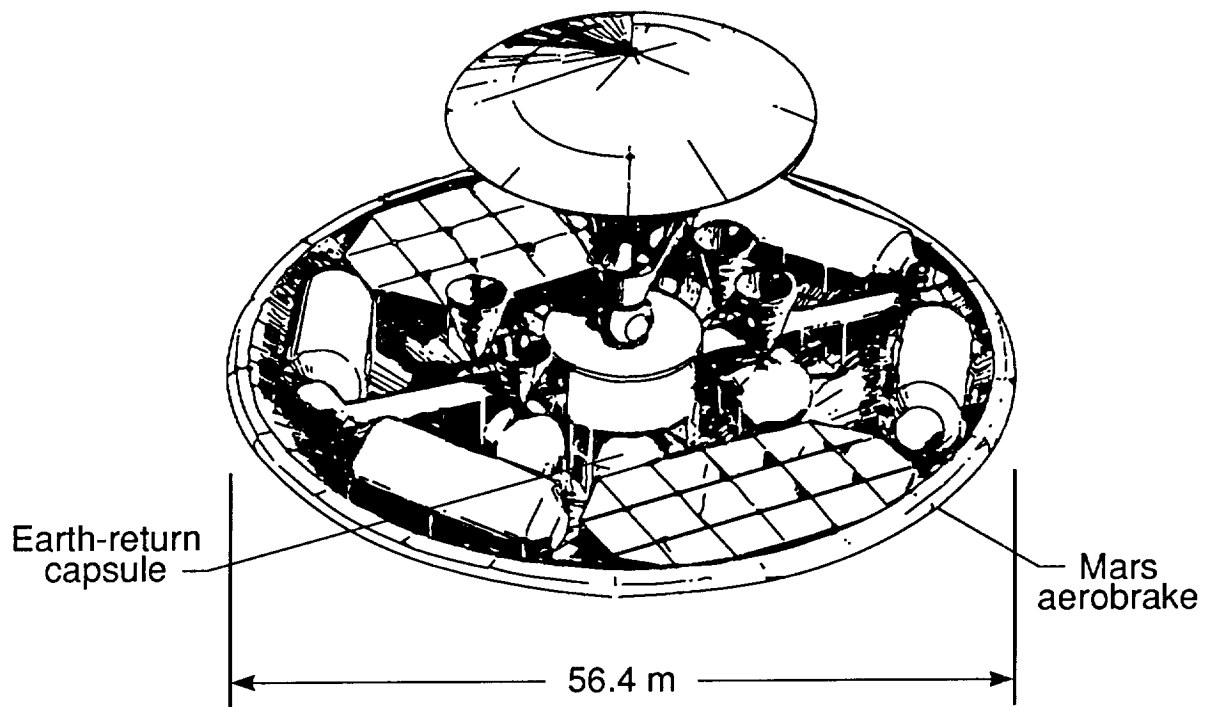
Figure 4. Martin Marietta conceptual design of a manned Mars vehicle. Aerobrake dimensions listed in table 5.

Figure 5. Short-cycle Earth-Mars planetary motion (≈ 25.62 months).

Figure 6. Long-cycle Earth-Mars planetary motion (≈ 15 years).
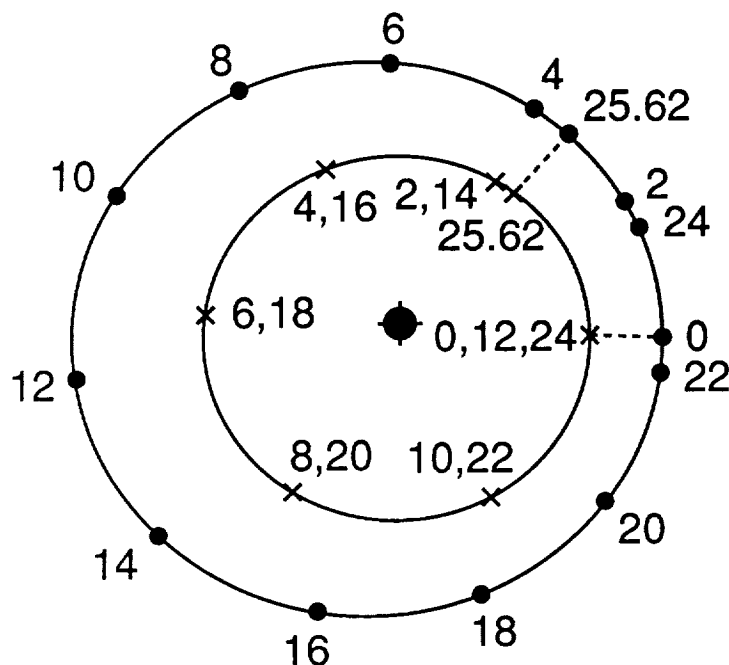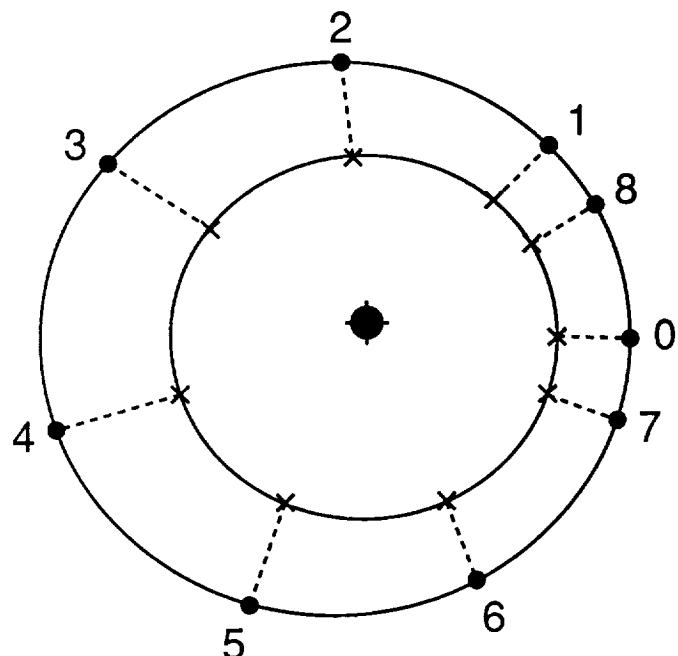
× Earth
● Mars
   Venus
◉ Sun

---- Earth-Mars opposition

—— Earth-Mars opposition and
Earth-Venus opposition

Time interval between each
numbered opposition:
26 months, 2.135 years

Orbits shown to scale
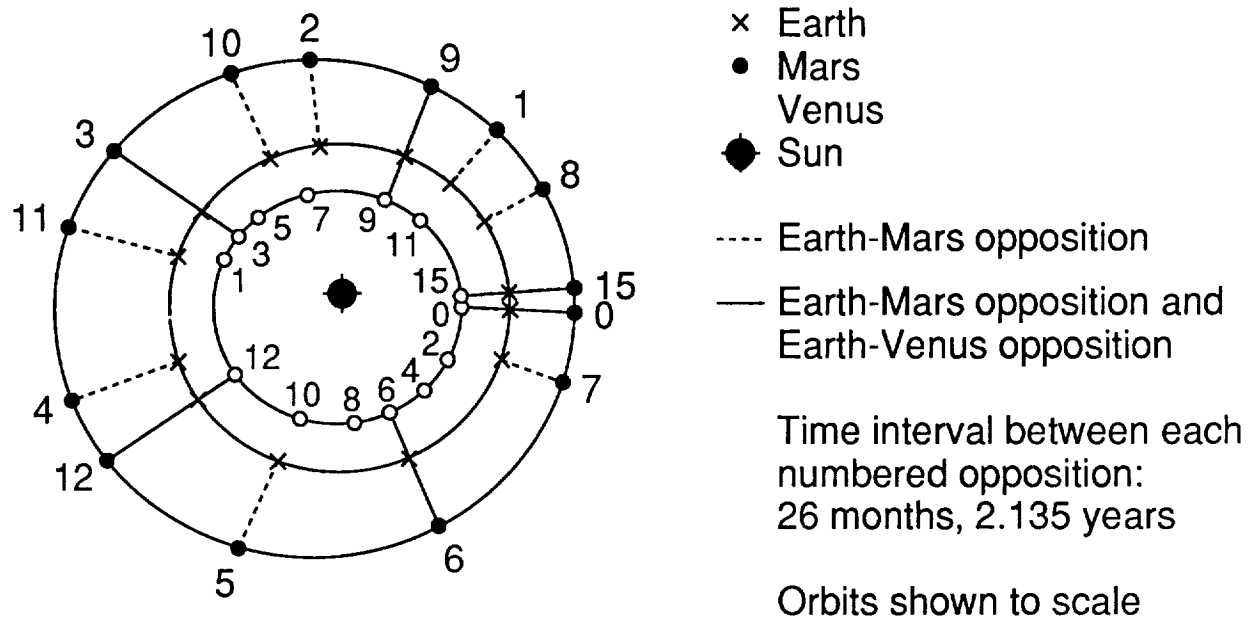
Figure 7. Earth-Mars-Venus planetary motion.
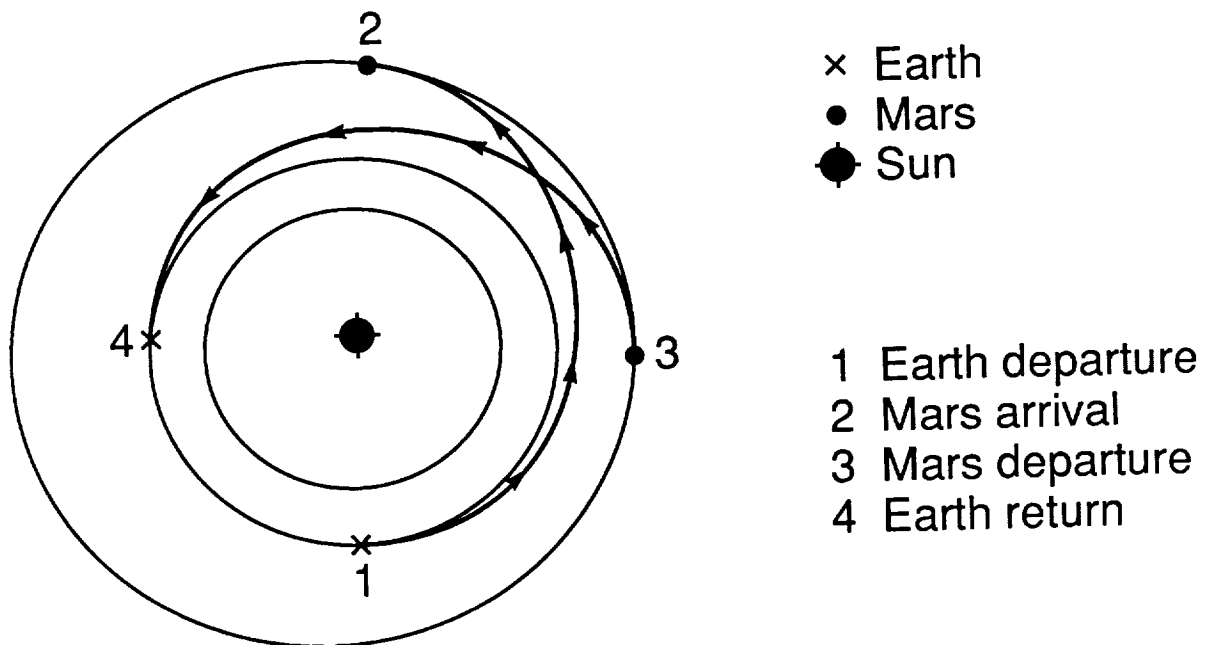
Figure 8. Conjunction-class mission (Mars stopover: 510 days).

x Earth
● Mars
◉ Sun

1 Earth departure
2 Mars arrival
3 Mars departure
4 Earth return
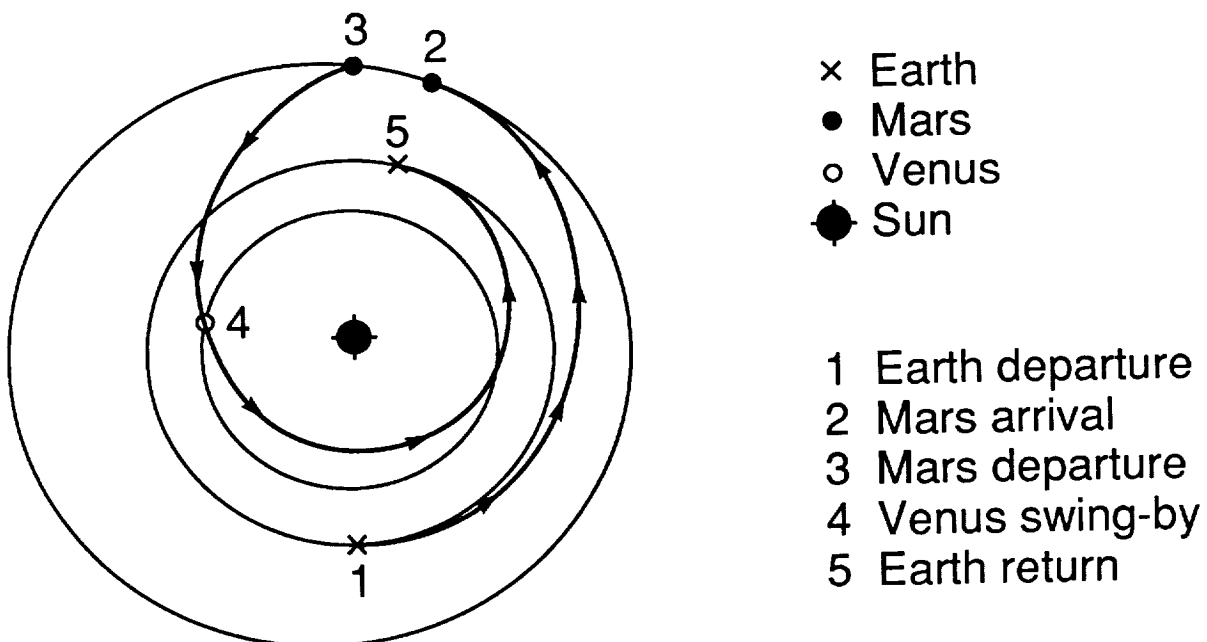
Figure 9. Opposition-class mission, inbound Venus swing-by (Mars stopover: 60 days).

x Earth
● Mars
o Venus
◉ Sun

1 Earth departure
2 Mars arrival
3 Mars departure
4 Venus swing-by
5 Earth return
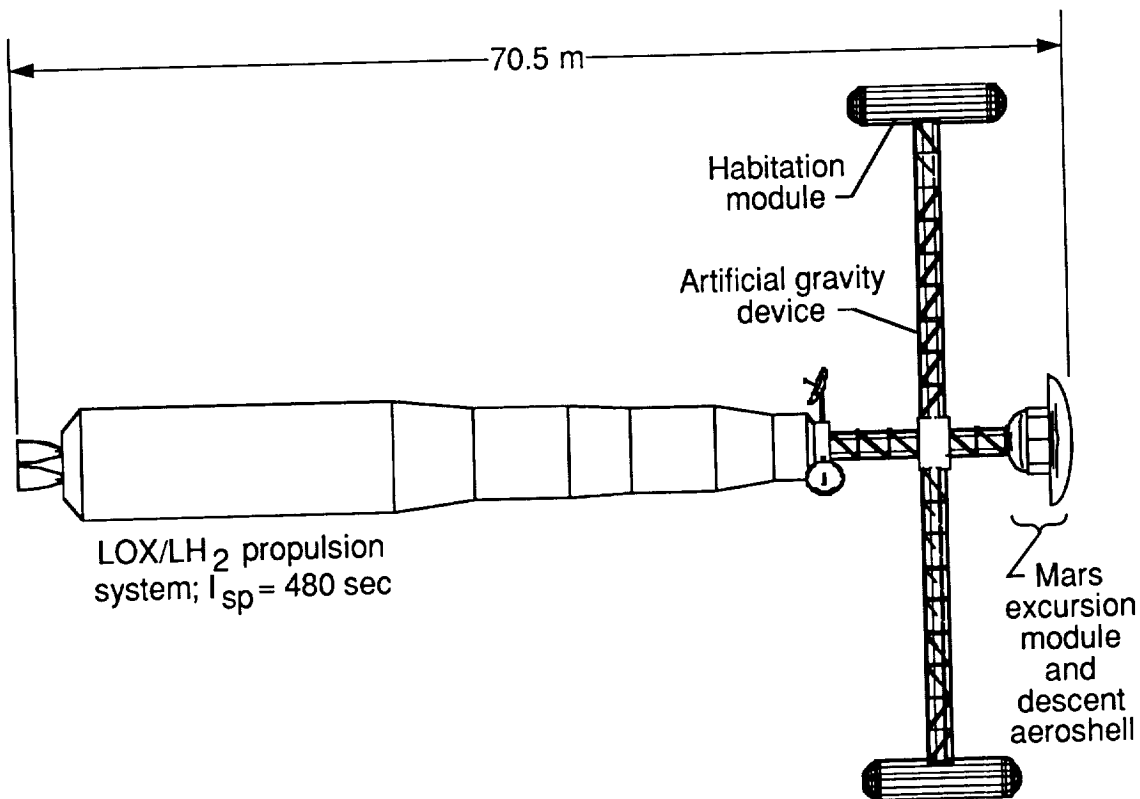
Figure 10. Conceptual all-propulsive vehicle configuration.
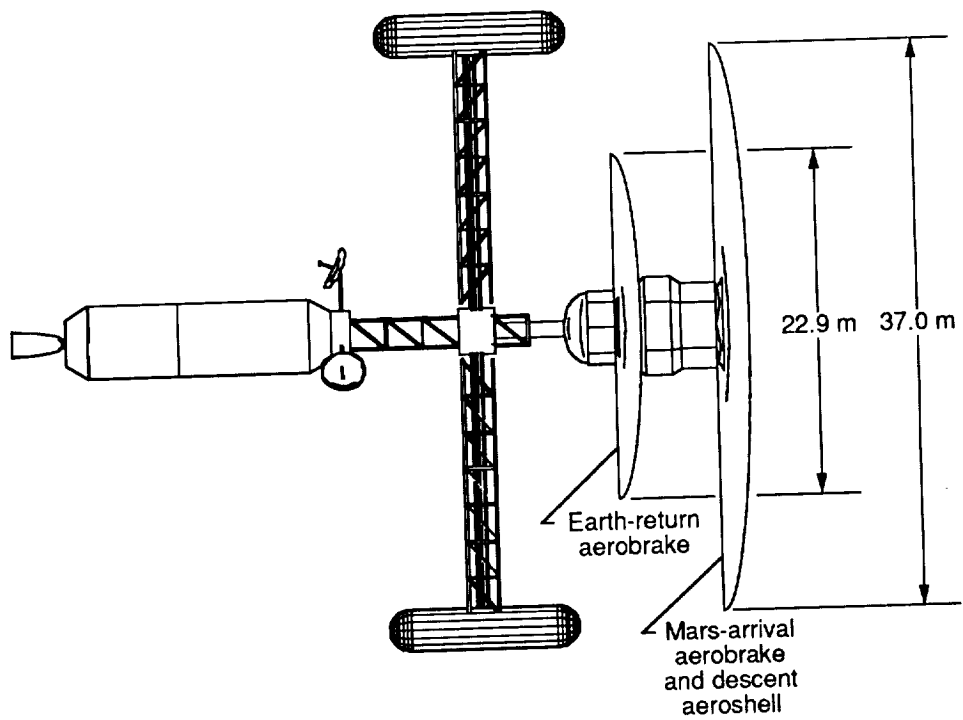
Figure 11. Conceptual aerobraking vehicle configuration.

Figure 12. Direct transfer.

Figure 13. Inverted direct transfer.
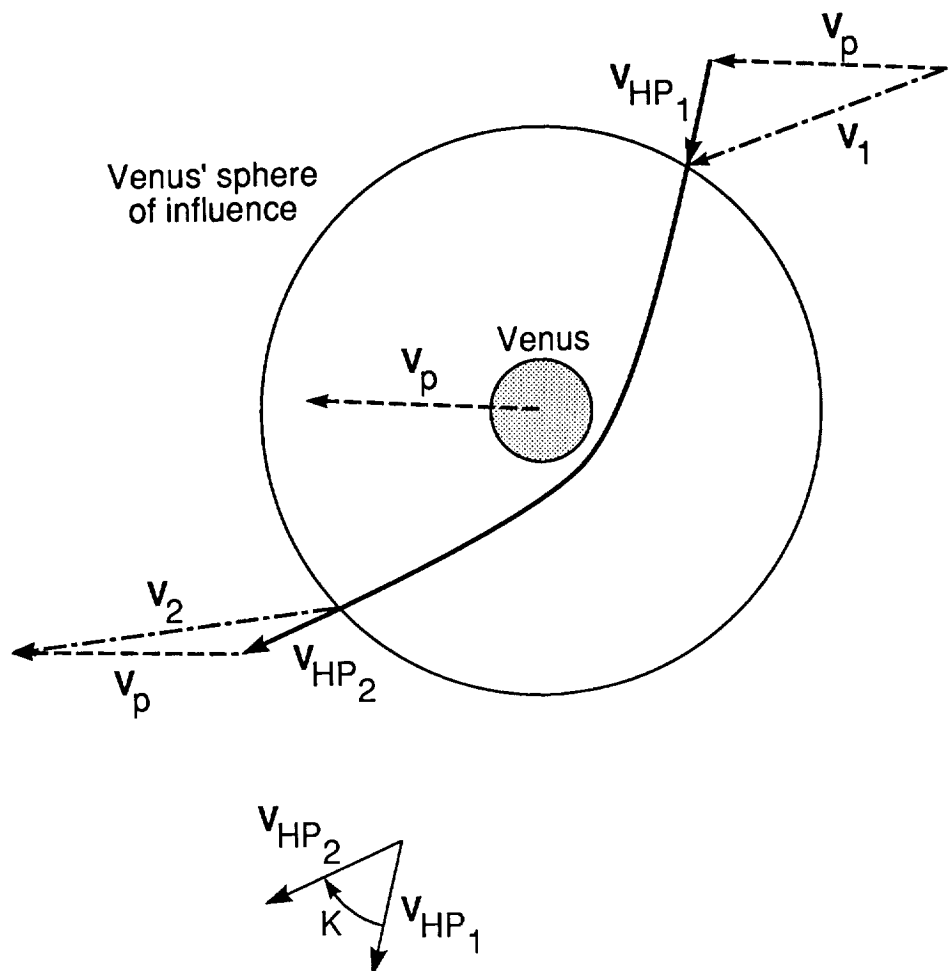
Figure 14. Venus swing-by mechanics.
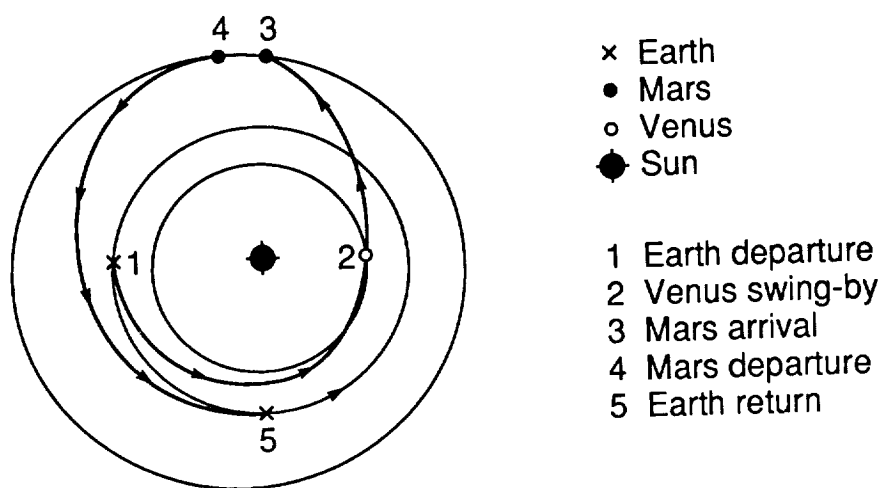
Figure 15. Outbound Venus swing-by.
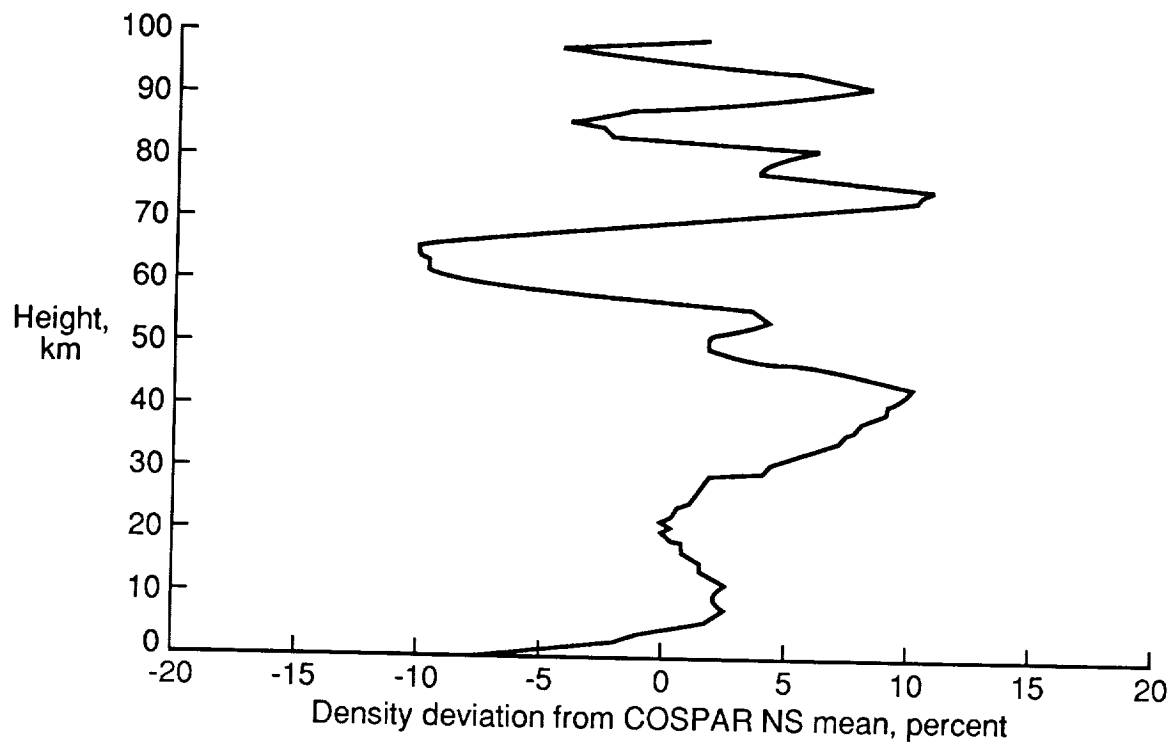
Figure 16. Viking 1 entry data compared with COSPAR NS mean.
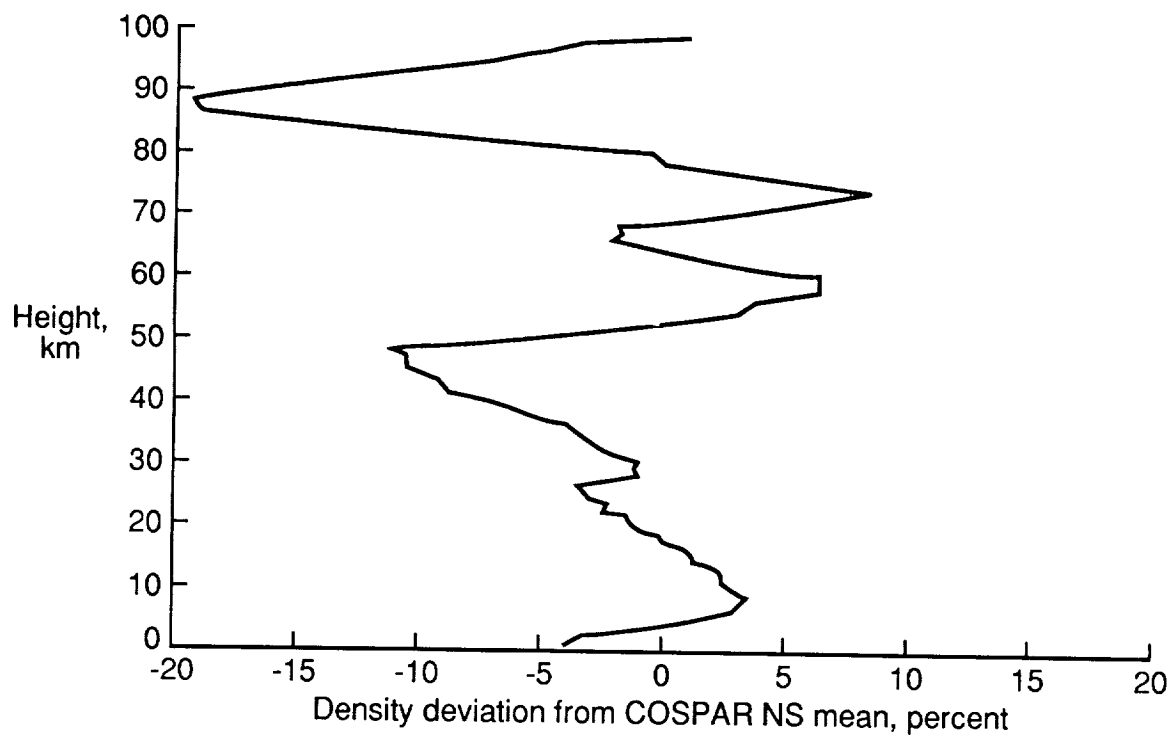
Figure 17. Viking 2 entry data compared with COSPAR NS mean.

44
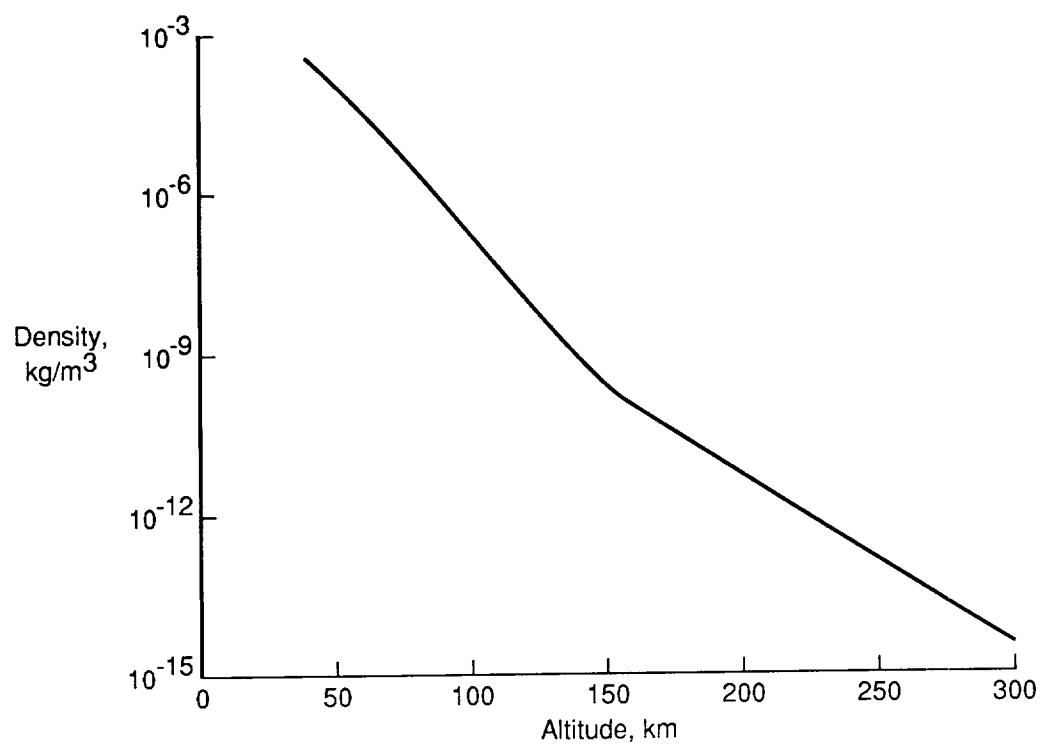
Figure 18. COSPAR NS mean density profile.
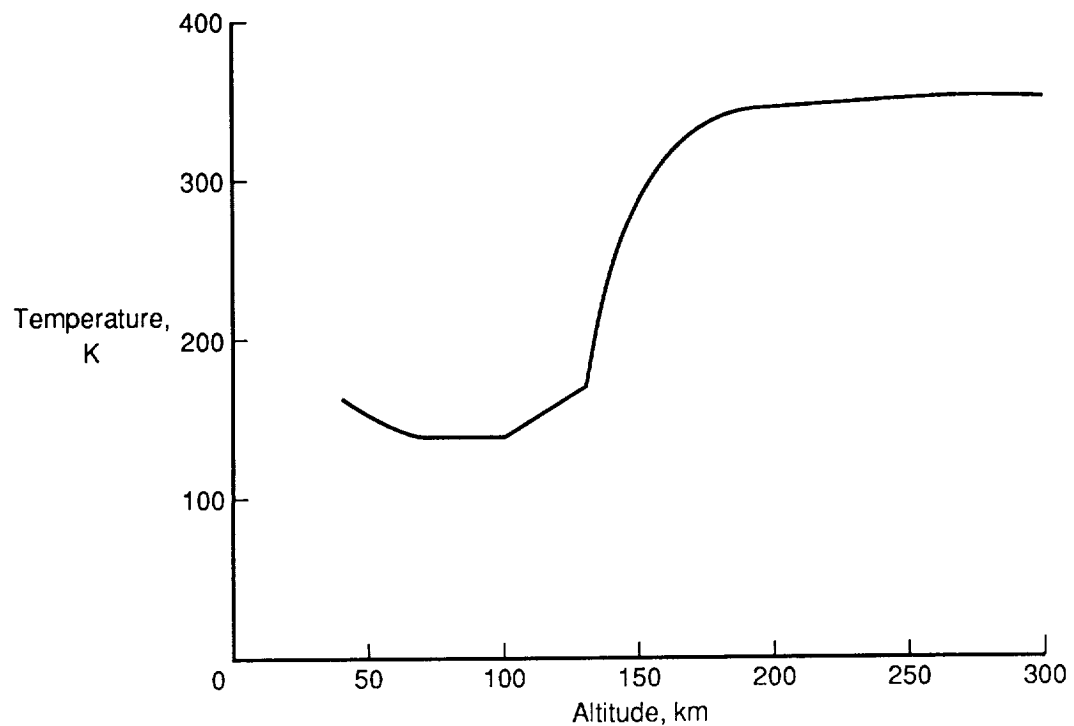
Figure 19. COSPAR NS mean temperature profile.
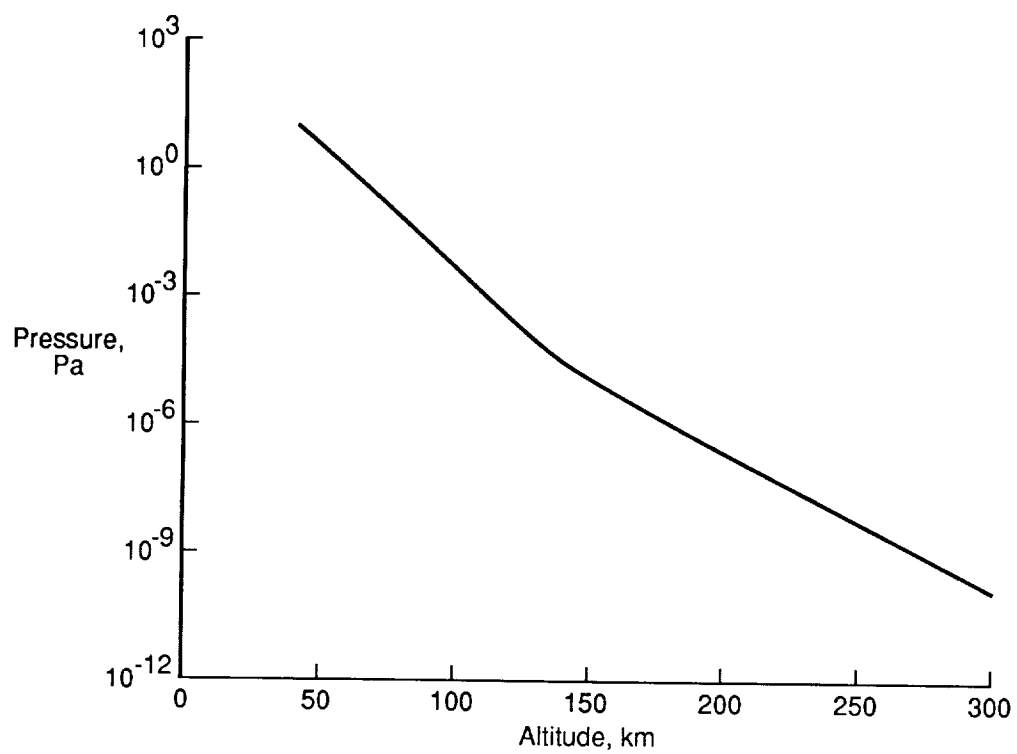
Figure 20. COSPAR NS mean pressure profile.
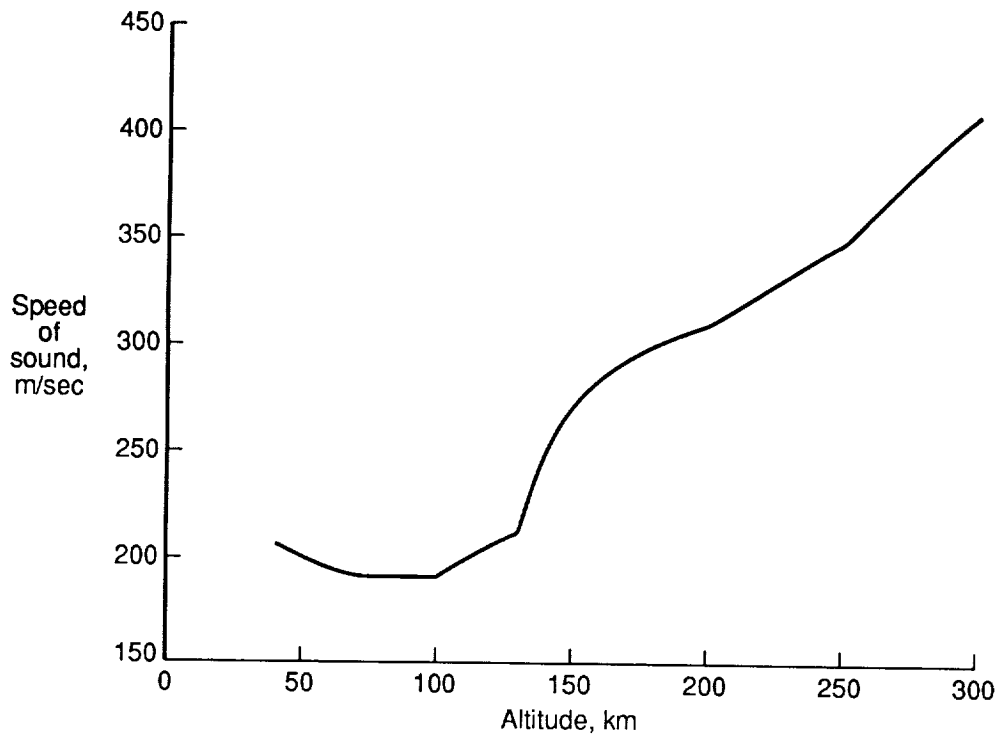
Figure 21. COSPAR NS mean-speed-of-sound profile.
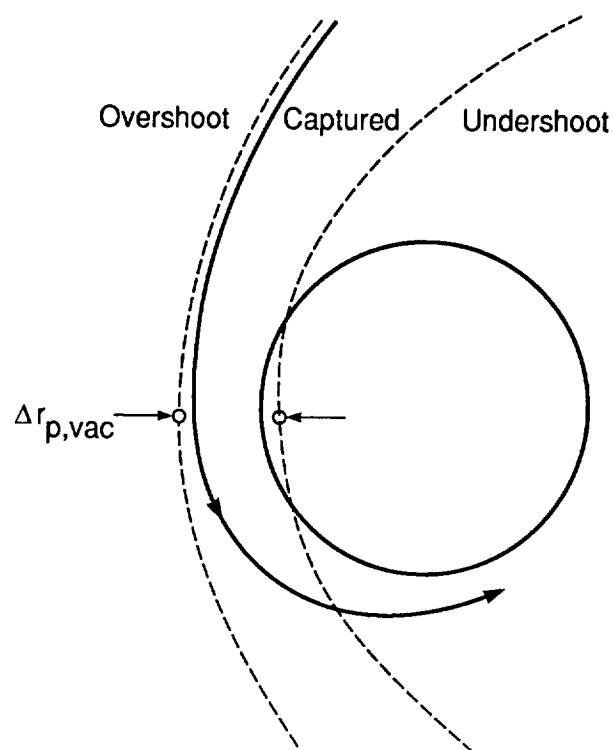
Figure 22. Classical definition of entry corridor (ref. 26).
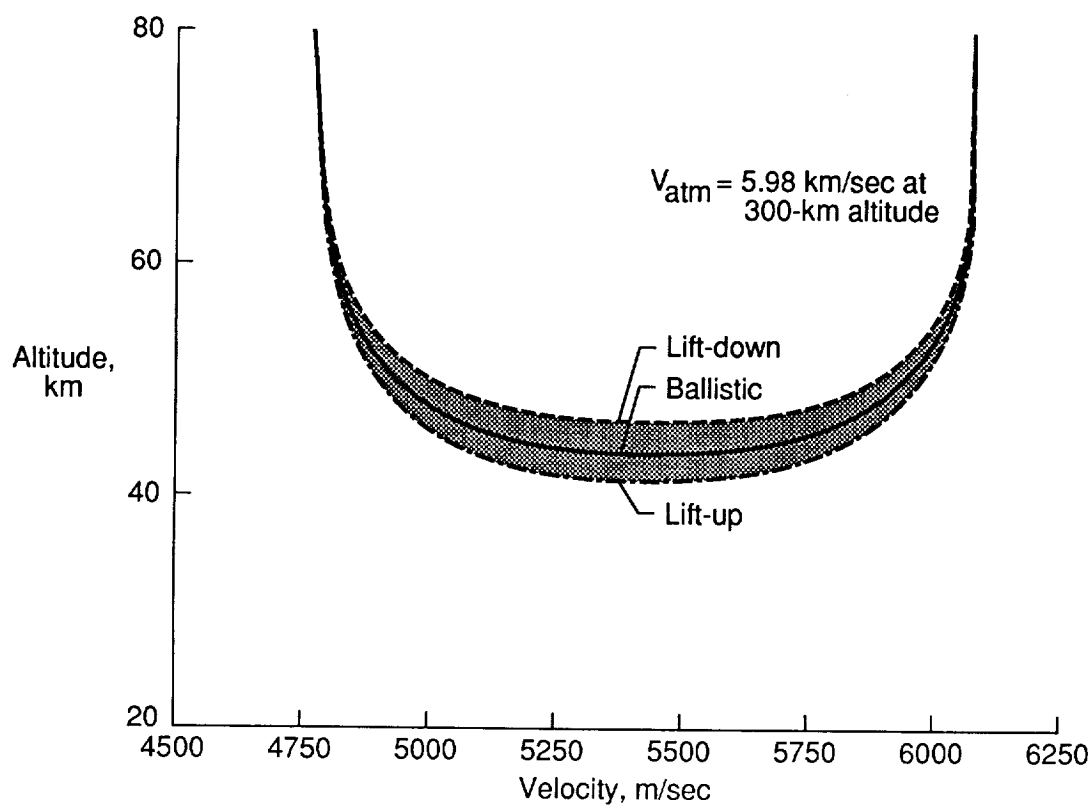
Figure 23. Entry corridor for a specific exit orbit.
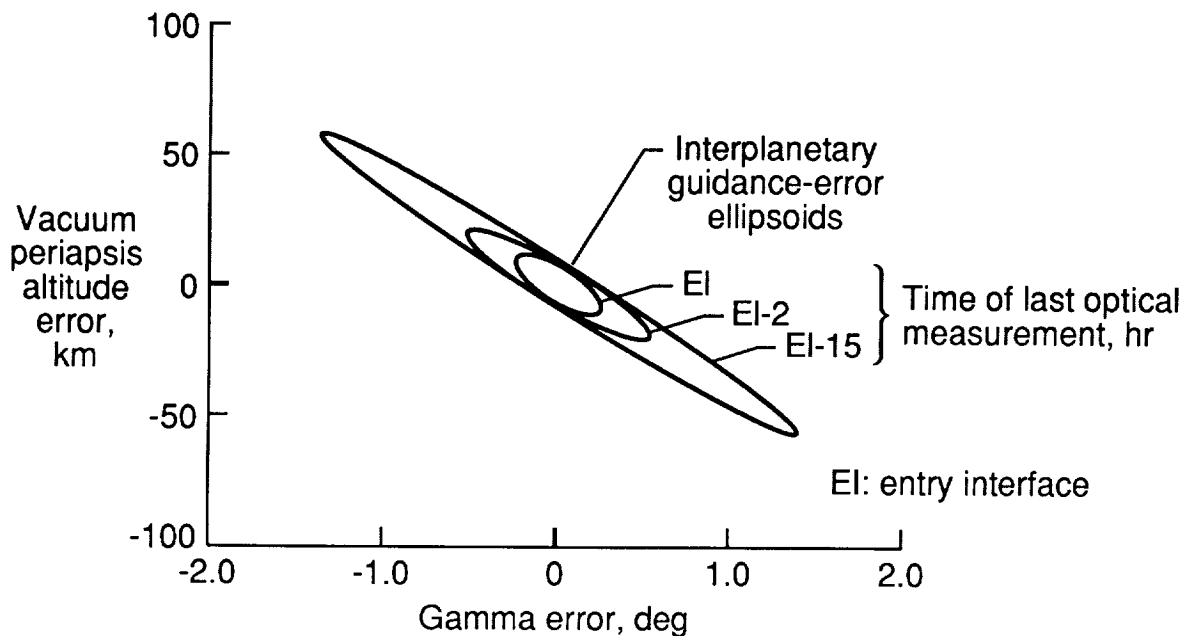
Figure 24. Interplanetary navigation-error ellipsoids with use of an optical, autonomous system (ref. 29).
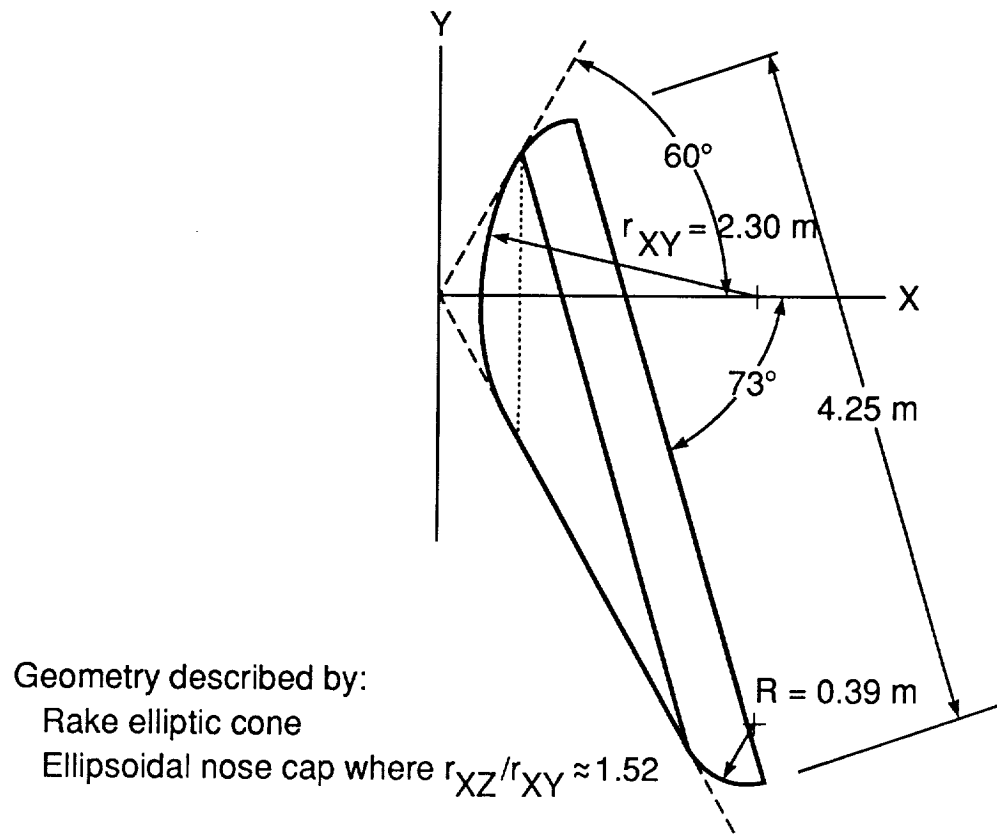
Figure 25. AFE aerodynamic shape (ref. 19).
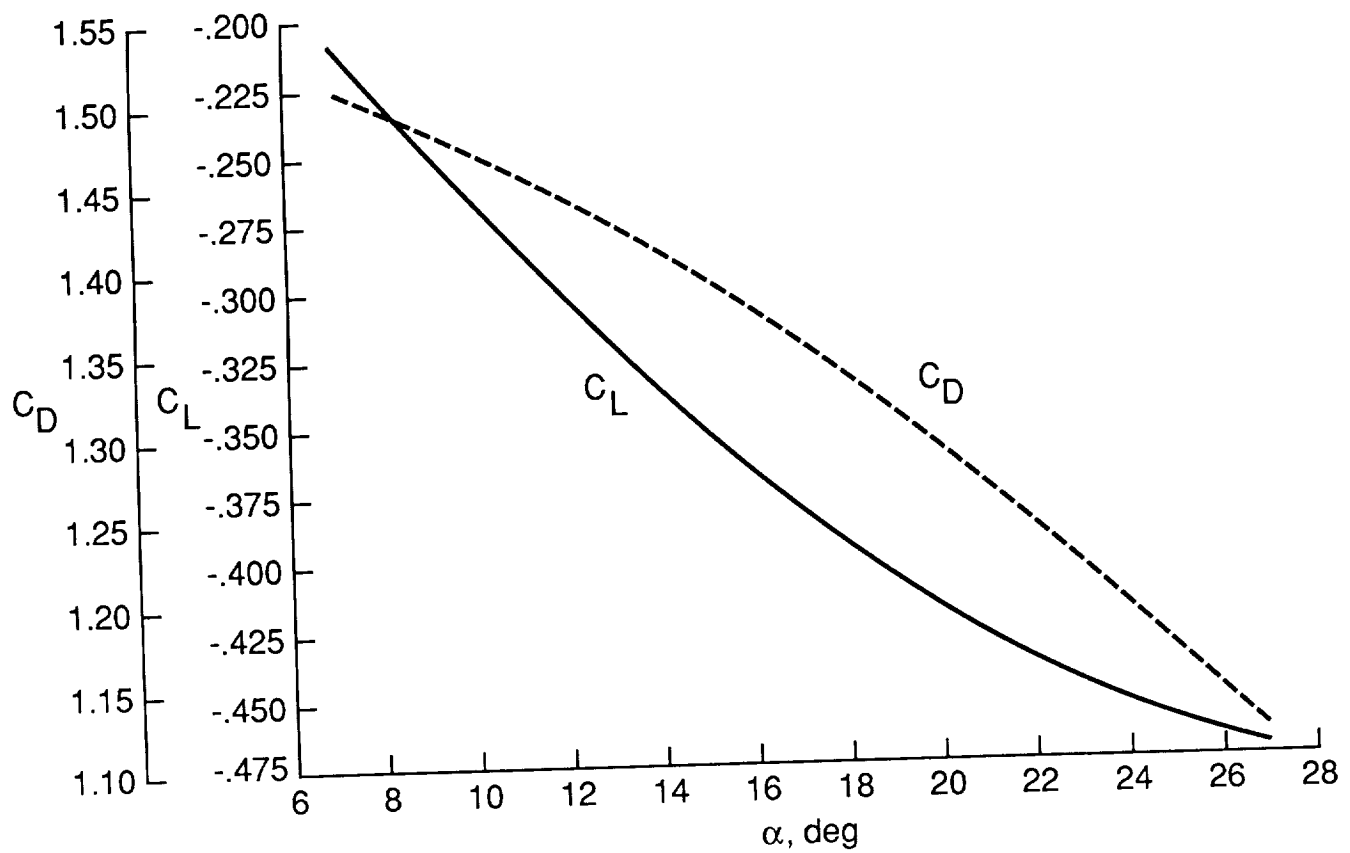
Figure 26. Continuum aerodynamic coefficients.
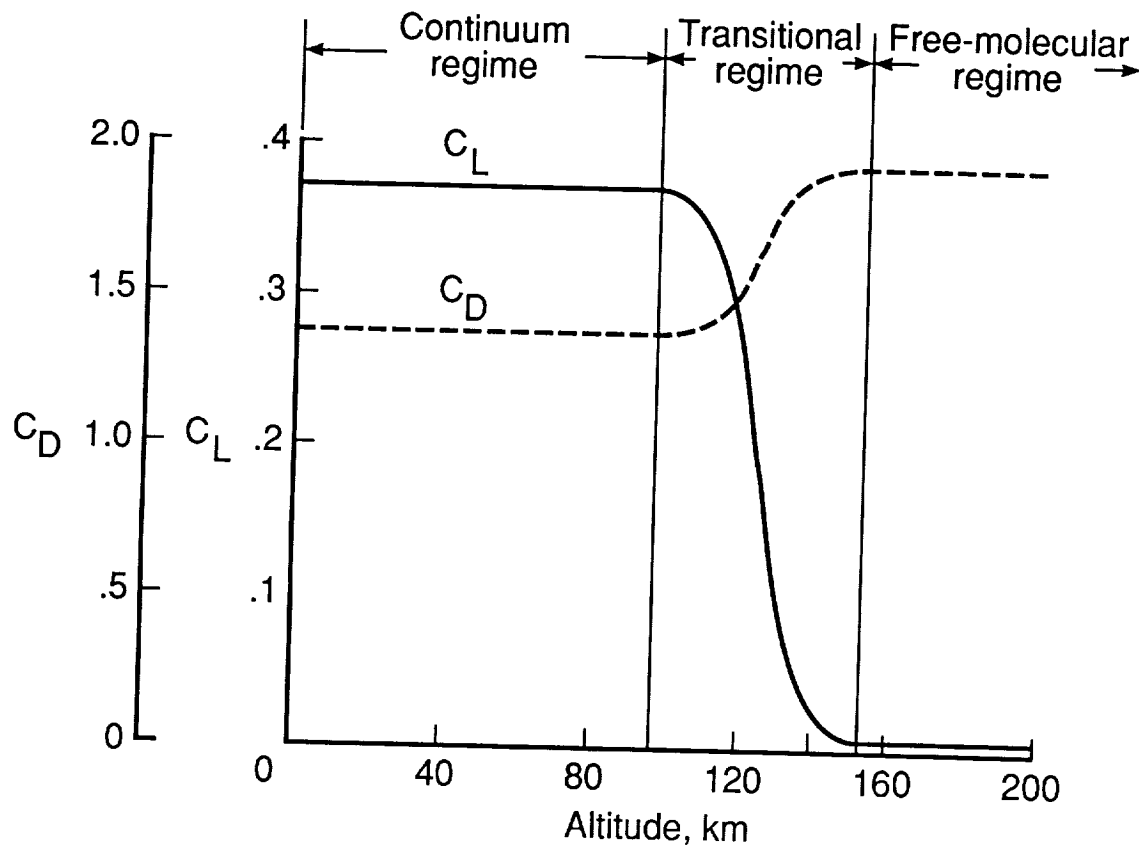
Figure 27. Effect of flow regimes on aerodynamic coefficients, $\alpha = 17°$.
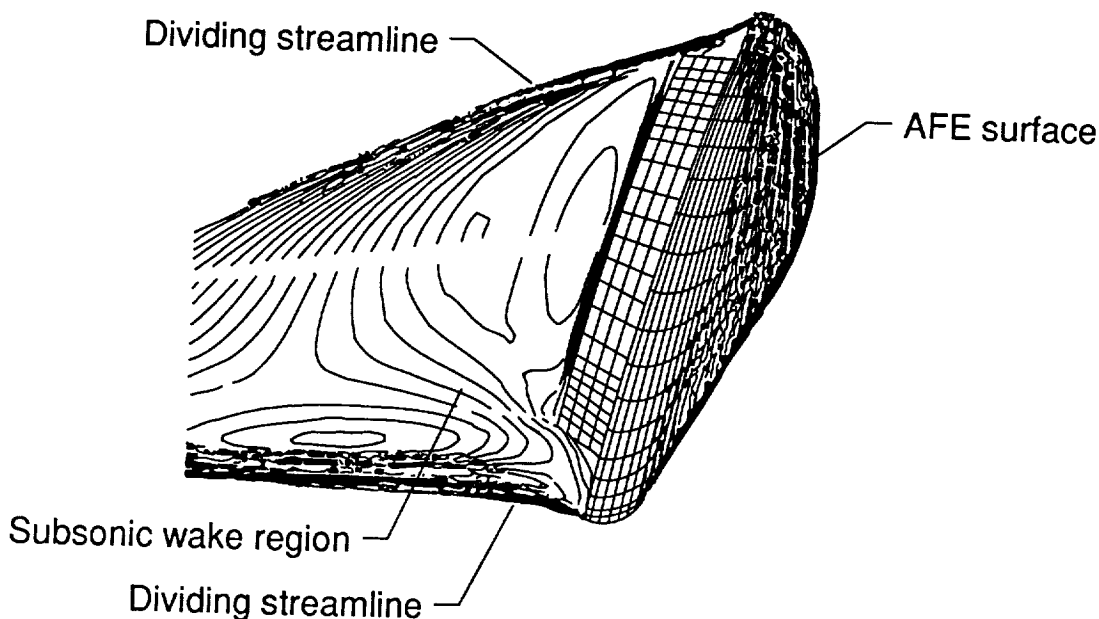
Figure 28. Subsonic flow regime behind AFE configuration (ref. 33).
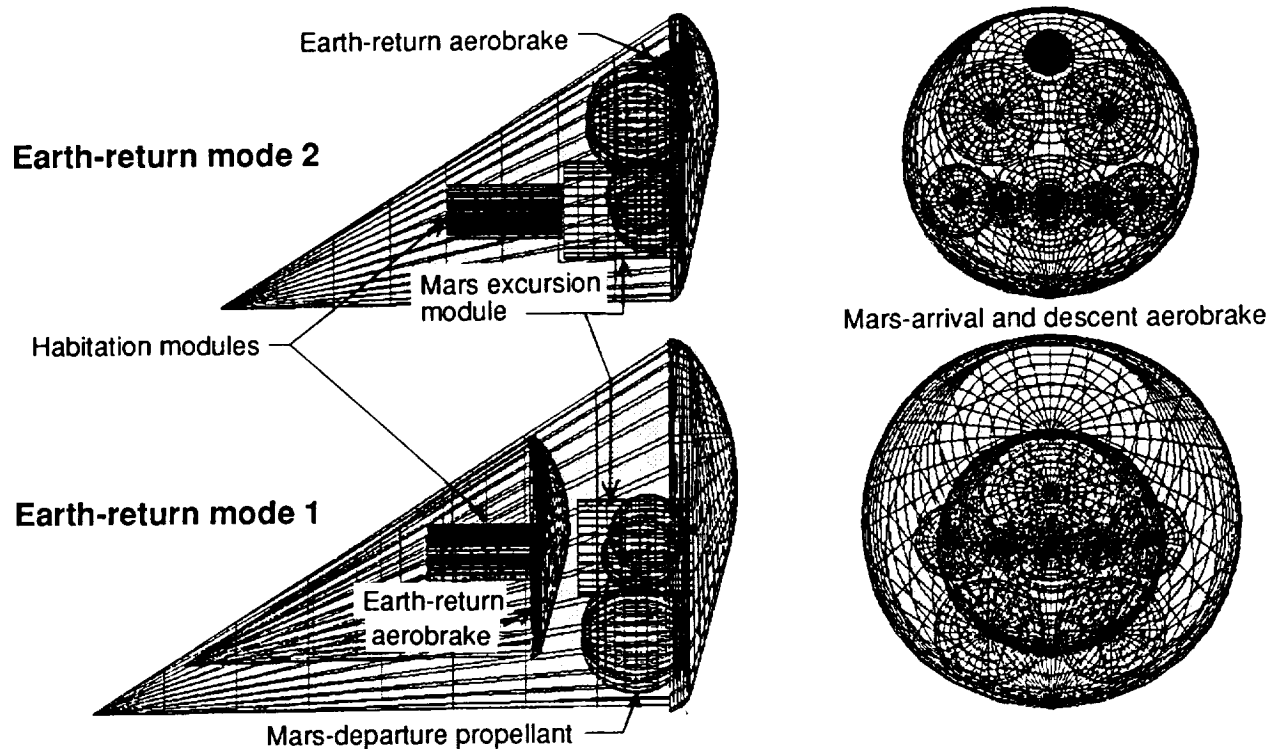
Figure 29. Aerobrake vehicle configurations upon Mars arrival.
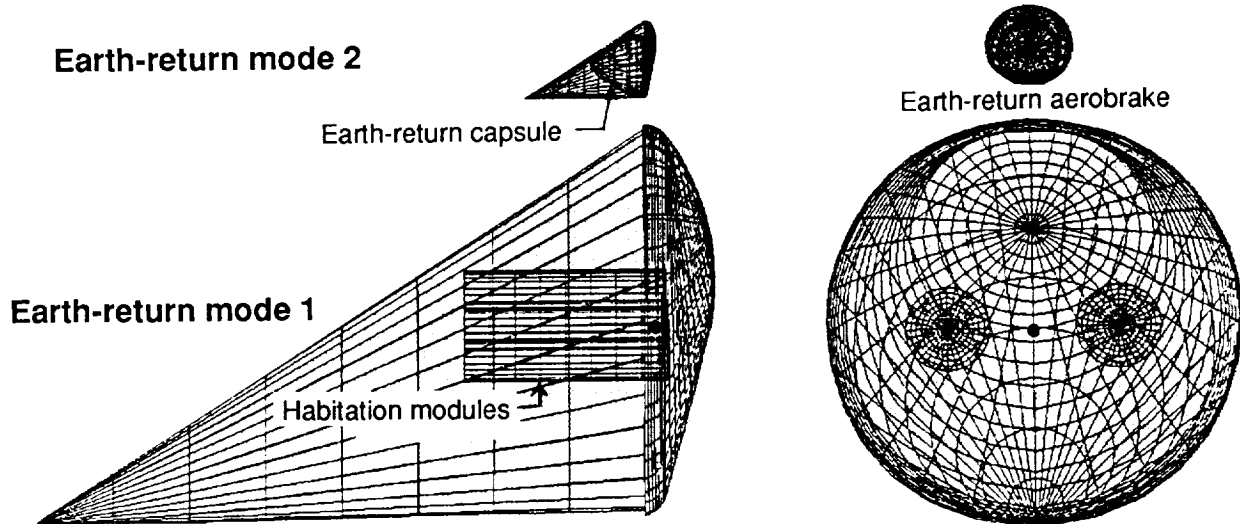
Figure 30. Aerobrake vehicle configurations upon Earth return.
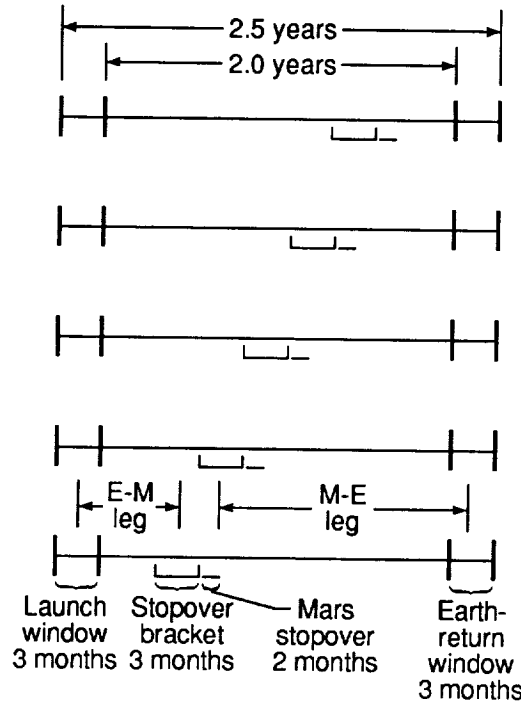
Figure 31. Direct mission simulation procedure. E-M is Earth-Mars; M-E is Mars-Earth.
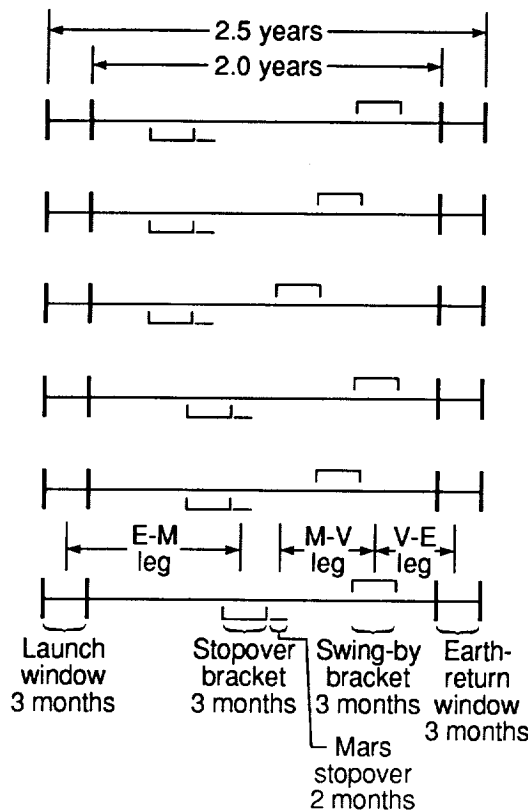
Figure 32. Inbound swing-by mission simulation procedure. E-M is Earth-Mars; M-V is Mars-Venus; V-E is Venus-Earth.
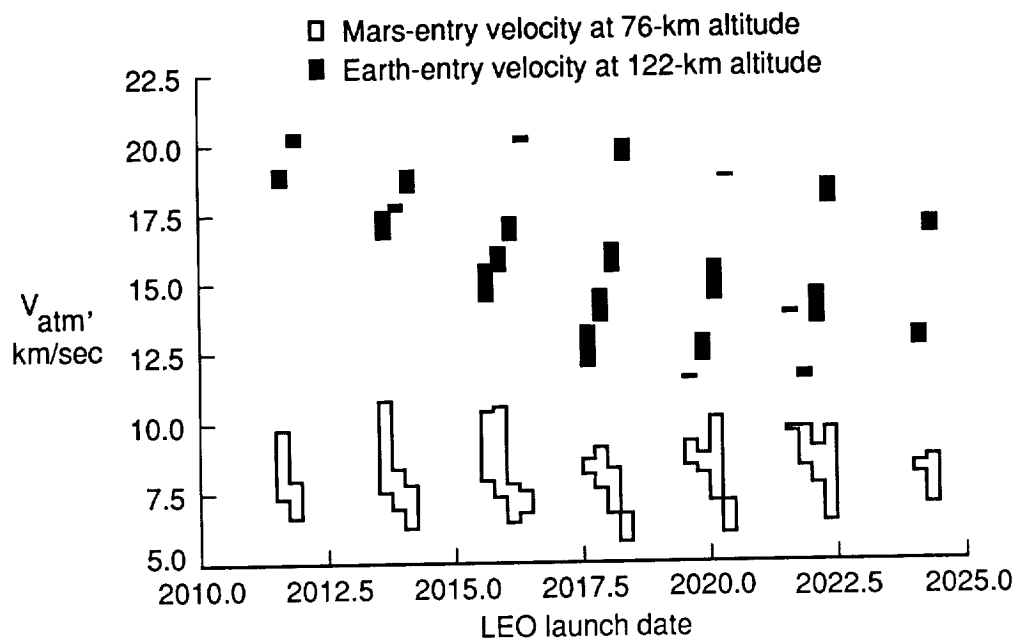
(a) Entry velocity versus launch date.
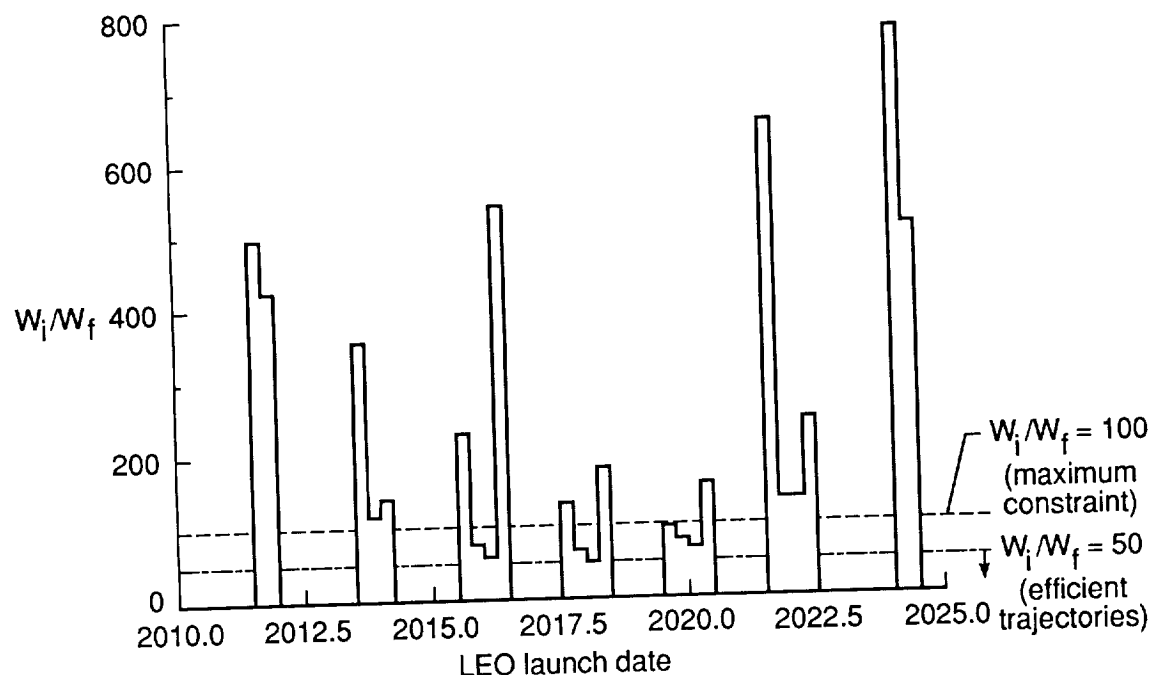
(b) Minimum vehicle weight ratio versus launch date (all-propulsive, Earth-return mode 1).

Figure 33. Direct missions with total trip time of 1.0 years to 1.5 years.
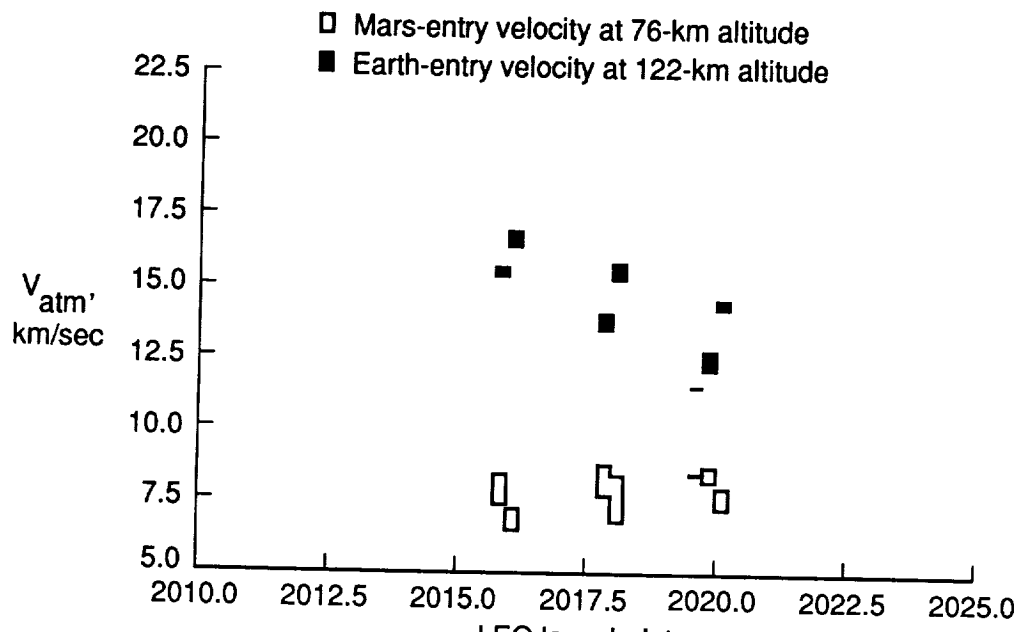
(a) Entry velocity versus launch date.
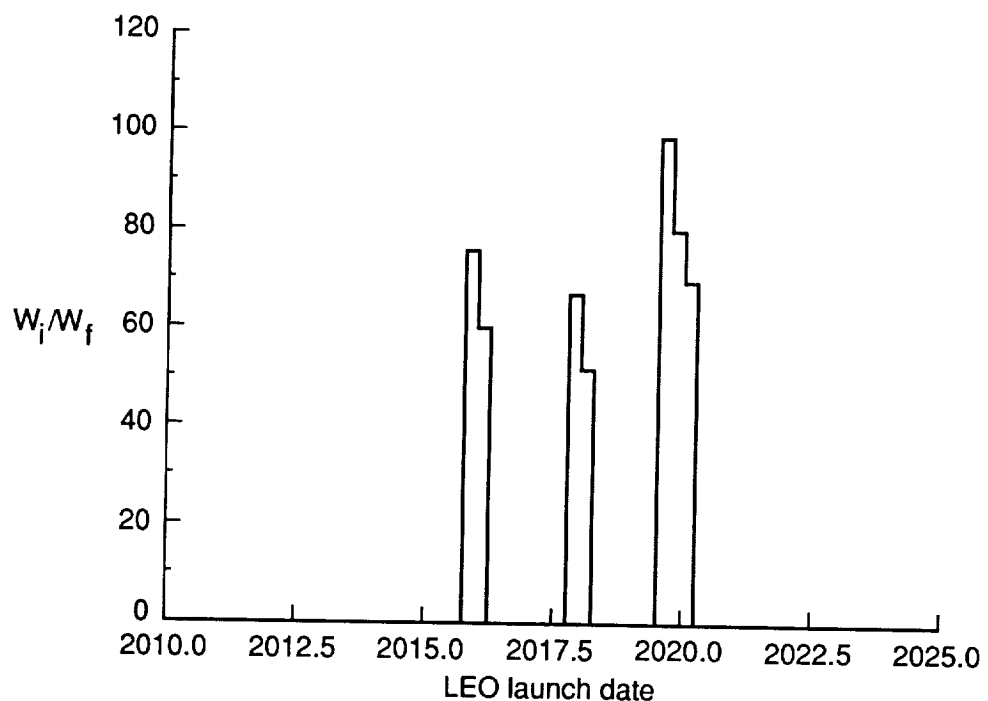
(b) Minimum vehicle weight ratio versus launch date (all-propulsive, Earth-return mode 1).

Figure 34. Direct missions with total trip time of 1.0 to 1.5 years for $W_i/W_f \leq 100$.
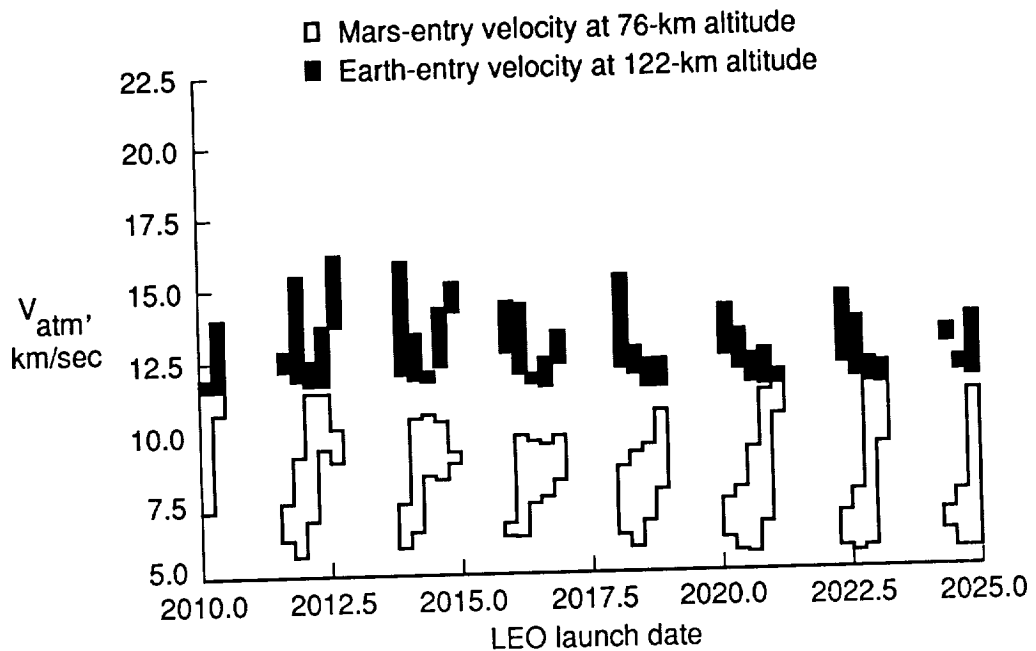
(a) Entry velocity versus launch date.
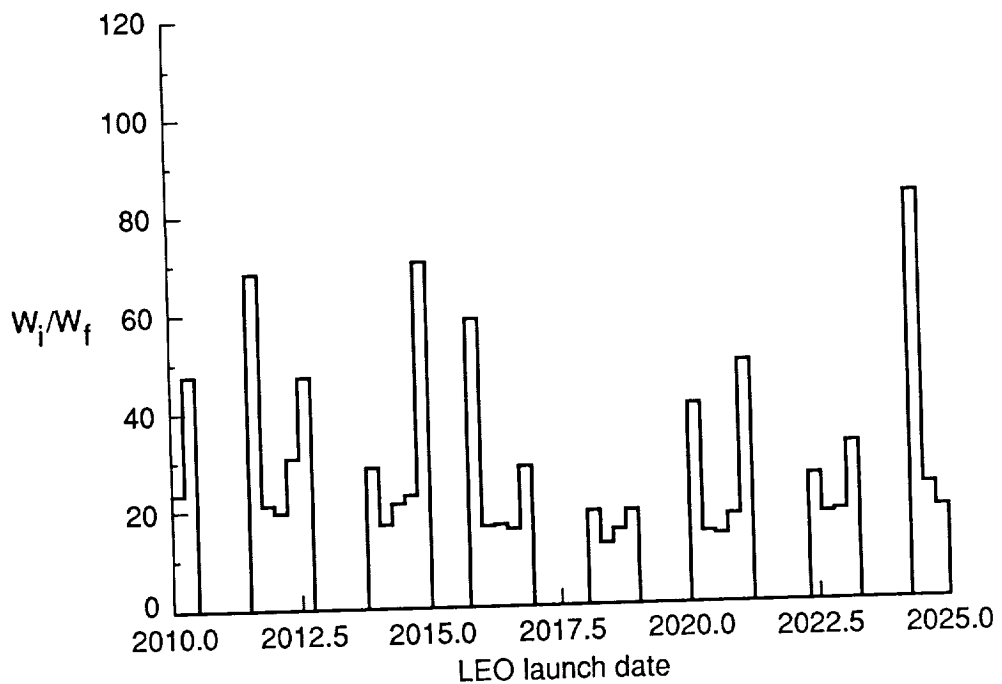
(b) Minimum vehicle weight ratio versus launch date (all-propulsive, Earth-return mode 1).

Figure 35. Direct missions with total trip time of 2.0 to 2.5 years for $W_i/W_f \leq 100$.
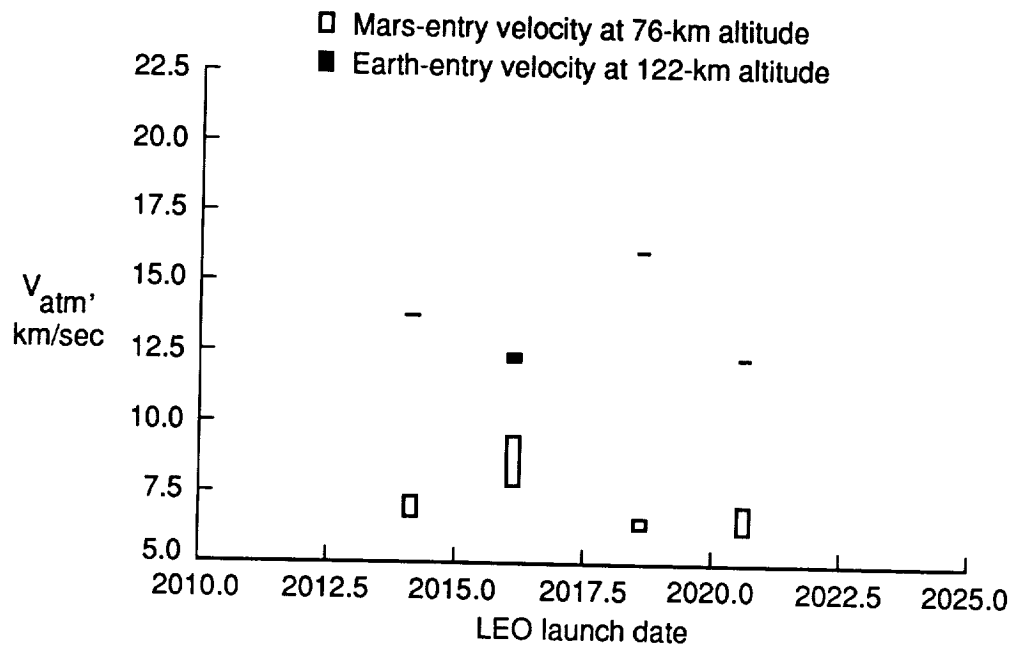
(a) Entry velocity versus launch date.
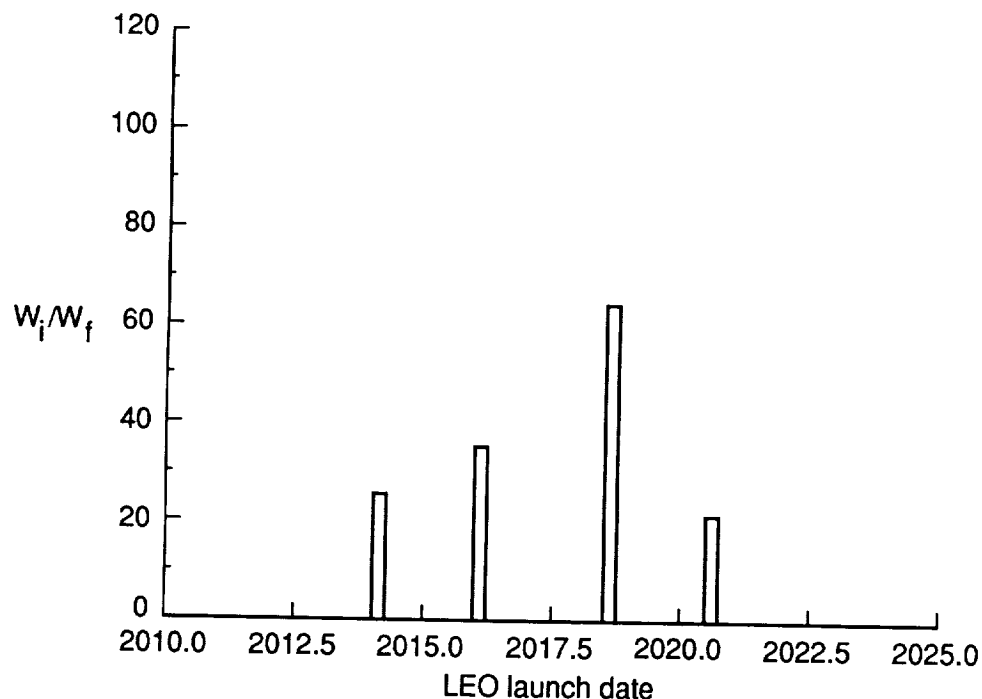
(b) Minimum vehicle weight ratio versus launch date (all-propulsive, Earth-return mode 1).

Figure 36. Inbound Venus swing-by missions with total trip time of 1.0 to 1.5 years for $W_i/W_f \leq 100$.
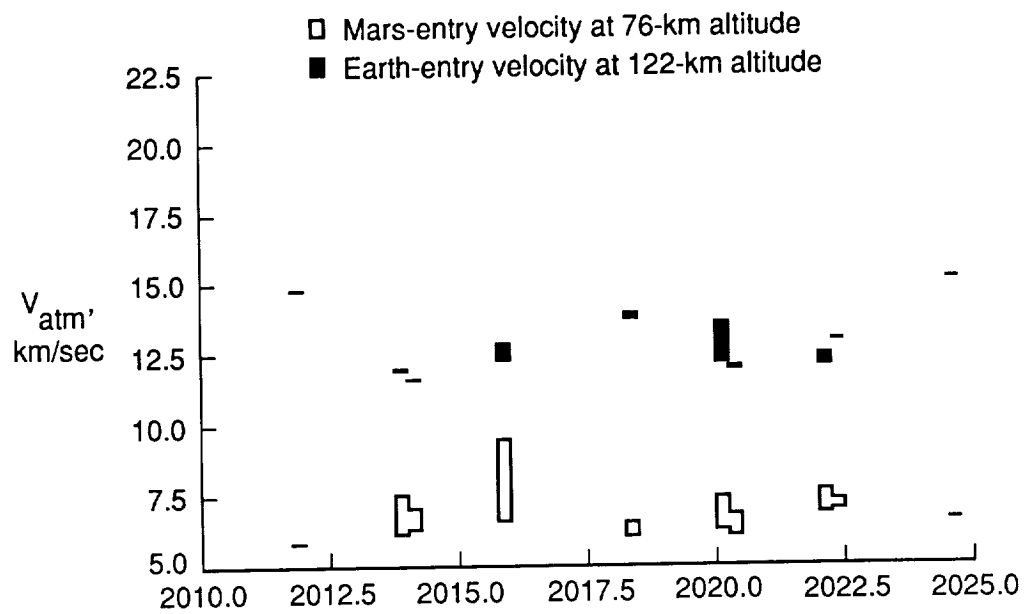
(a) Entry velocity versus launch date.
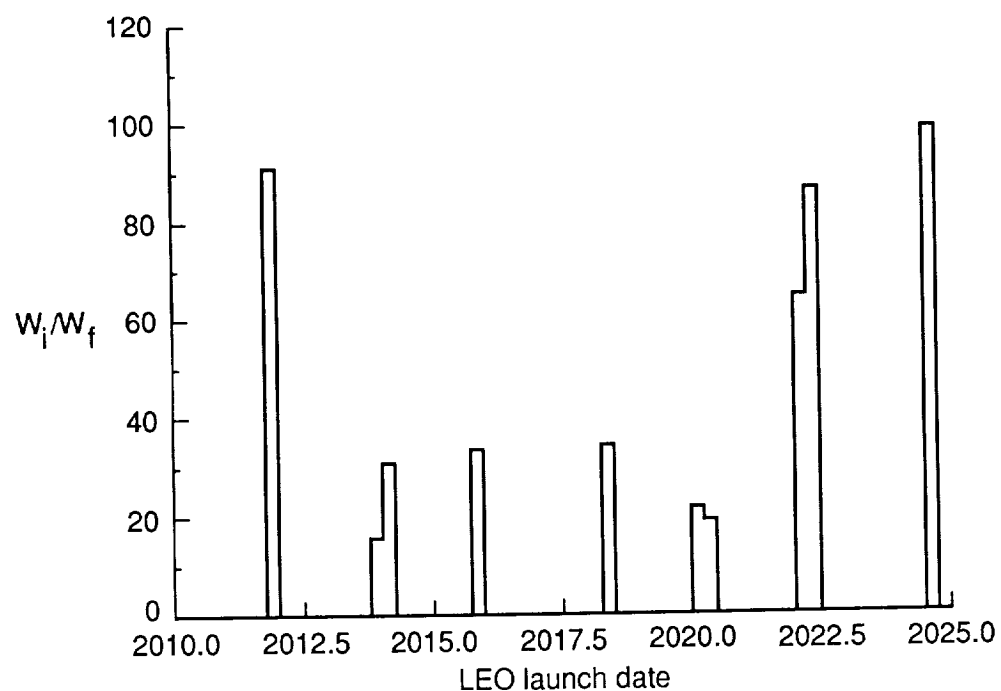
(b) Minimum vehicle weight ratio versus launch date (all-propulsive, Earth-return mode 1).

Figure 37. Inbound Venus swing-by missions with total trip time of 1.5 to 2.0 years for $W_i/W_f \leq 100$.
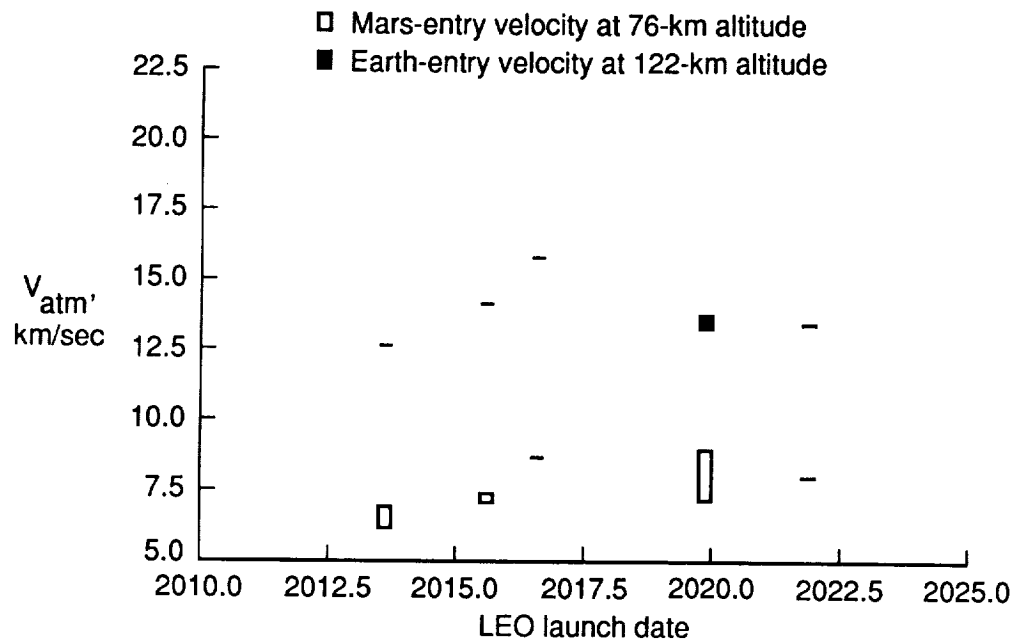
(a) Entry velocity versus launch date.
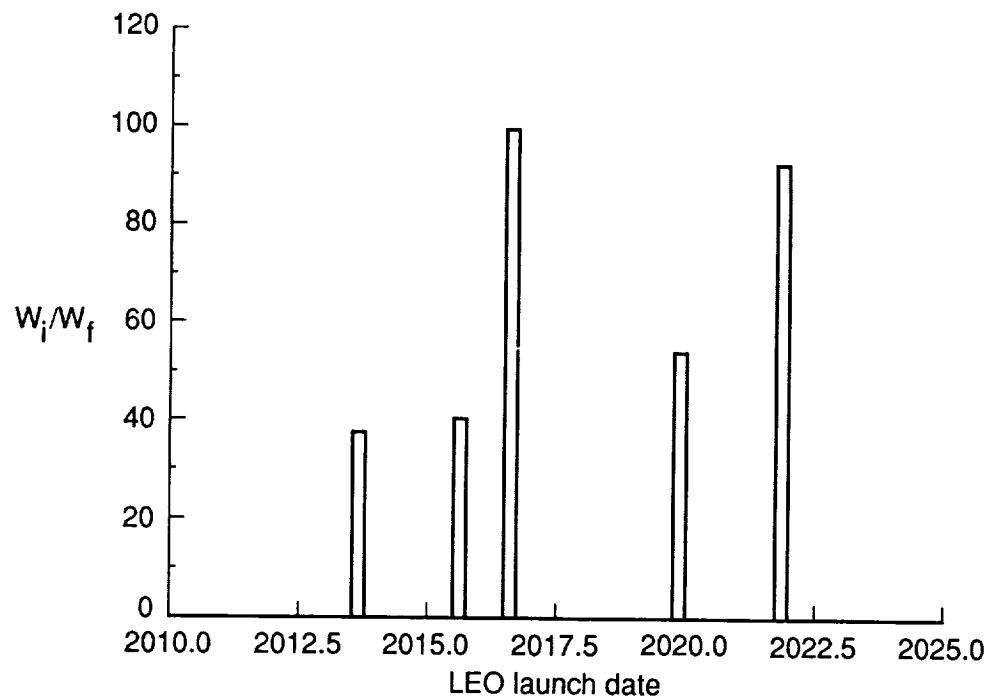
(b) Minimum vehicle weight ratio versus launch date (all-propulsive, Earth-return mode 1).

Figure 38. Inbound Venus swing-by missions with total trip time of 2.0 to 2.5 years for $W_i/W_f \leq 100$.
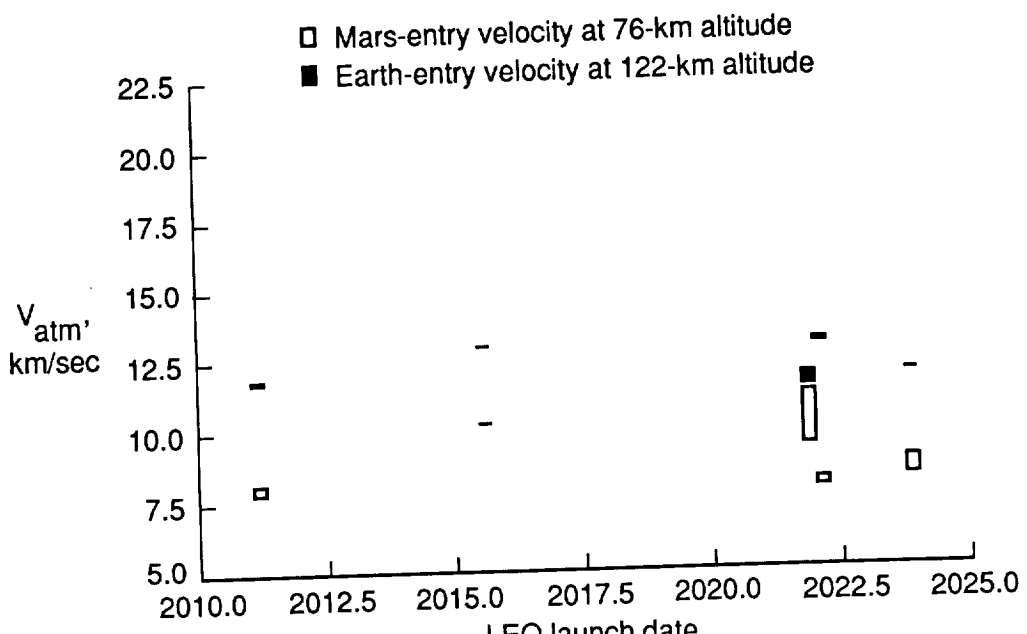
(a) Entry velocity versus launch date.
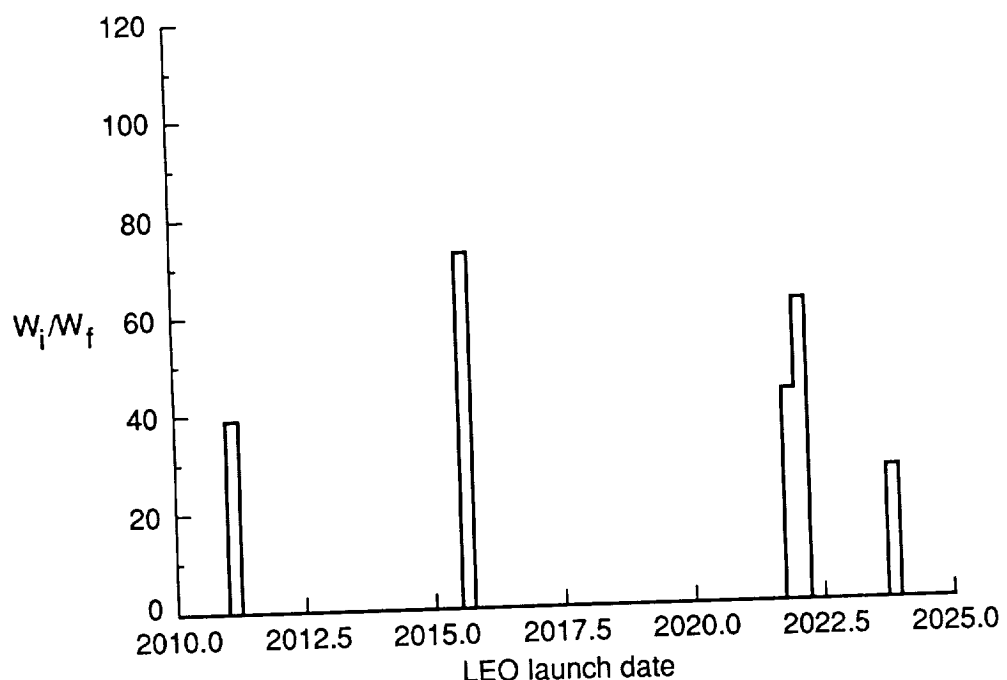
(b) Minimum vehicle weight ratio versus launch date (all-propulsive, Earth-return mode 1).

Figure 39. Outbound Venus swing-by missions with total trip time of 1.0 to 1.5 years for $W_i/W_f \leq 100$.
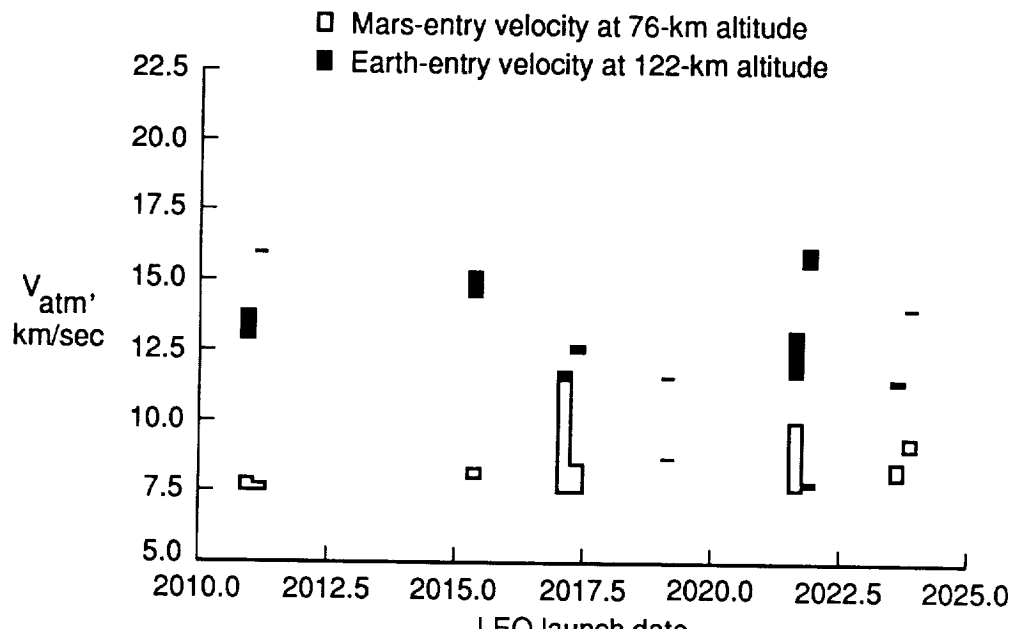
(a) Entry velocity versus launch date.
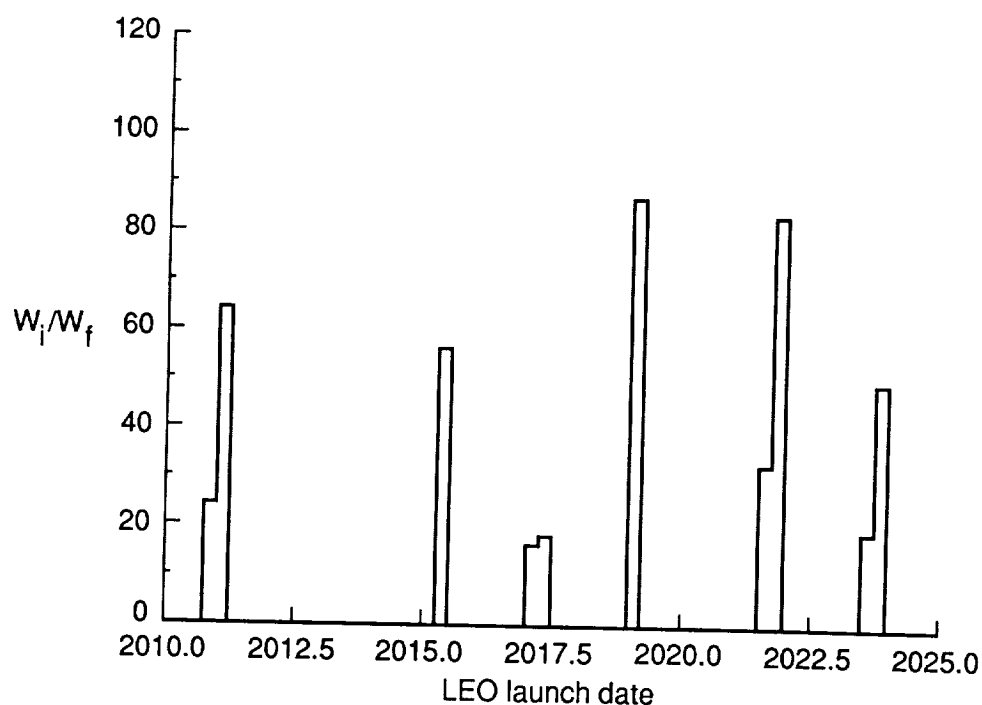
(b) Minimum vehicle weight ratio versus launch date (all-propulsive, Earth-return mode 1).

Figure 40. Outbound Venus swing-by missions with total trip time of 1.5 to 2.0 years for $W_i/W_f \leq 100$.
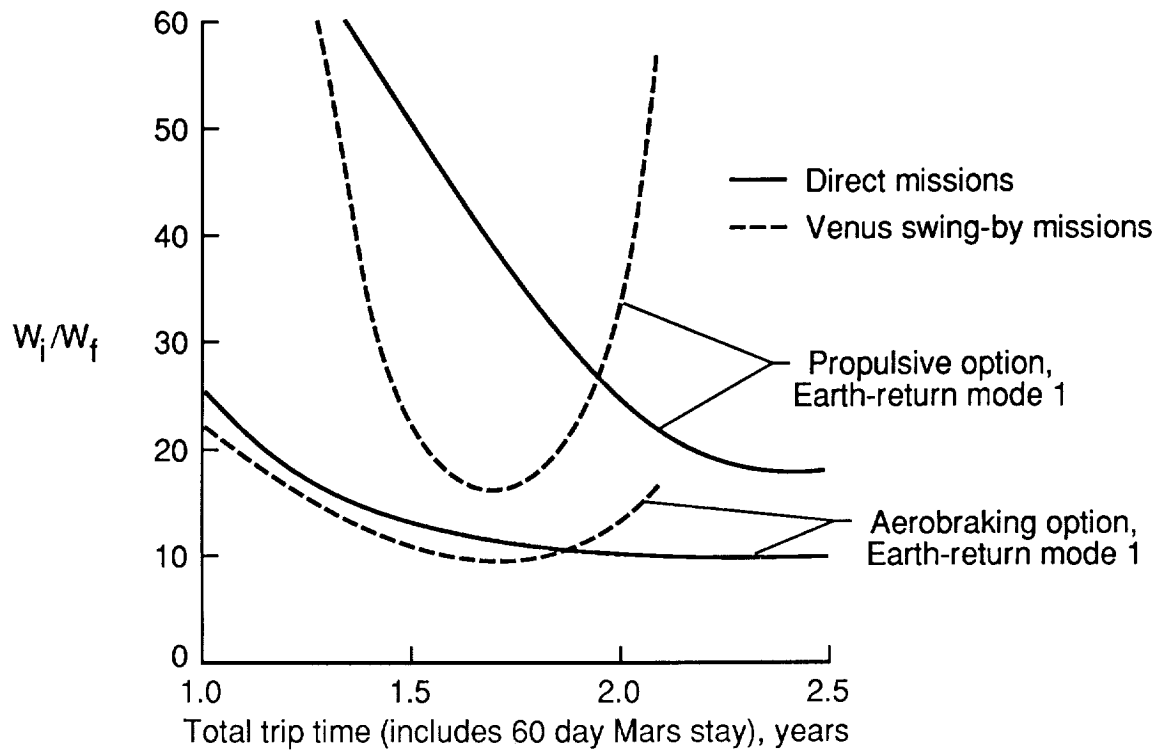
Figure 41. Vehicle weight ratio comparison (direct versus Venus swing-by transfers; propulsive versus aerobraking deceleration).
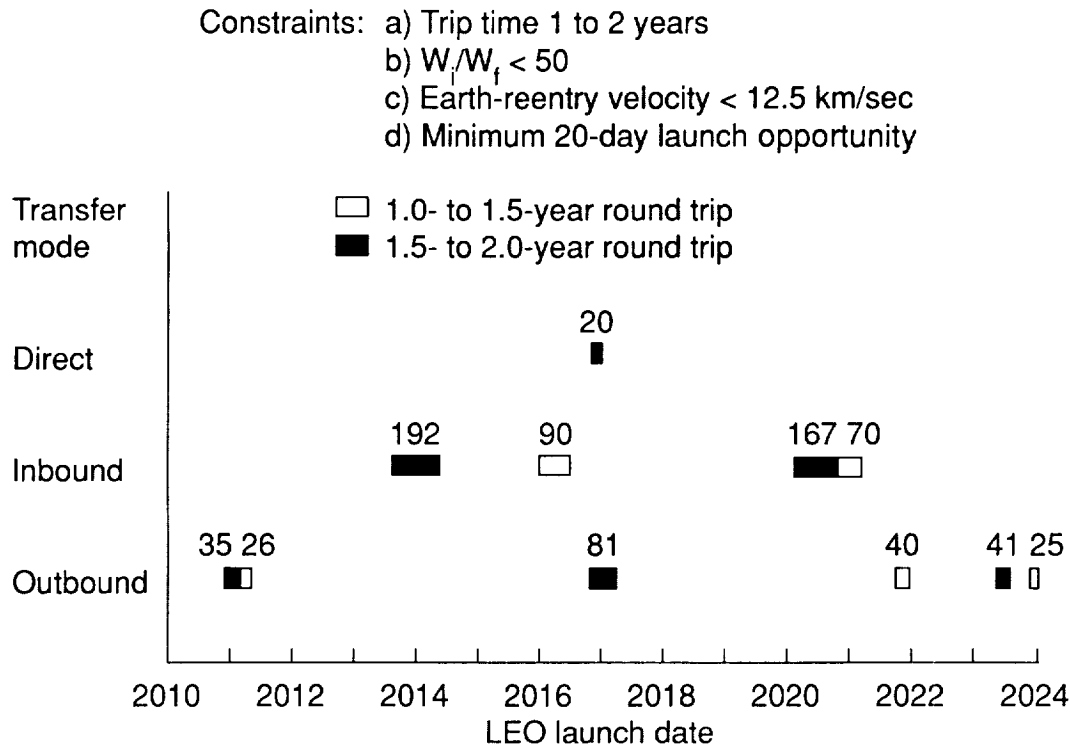
Figure 42. Selected launch opportunities, days.
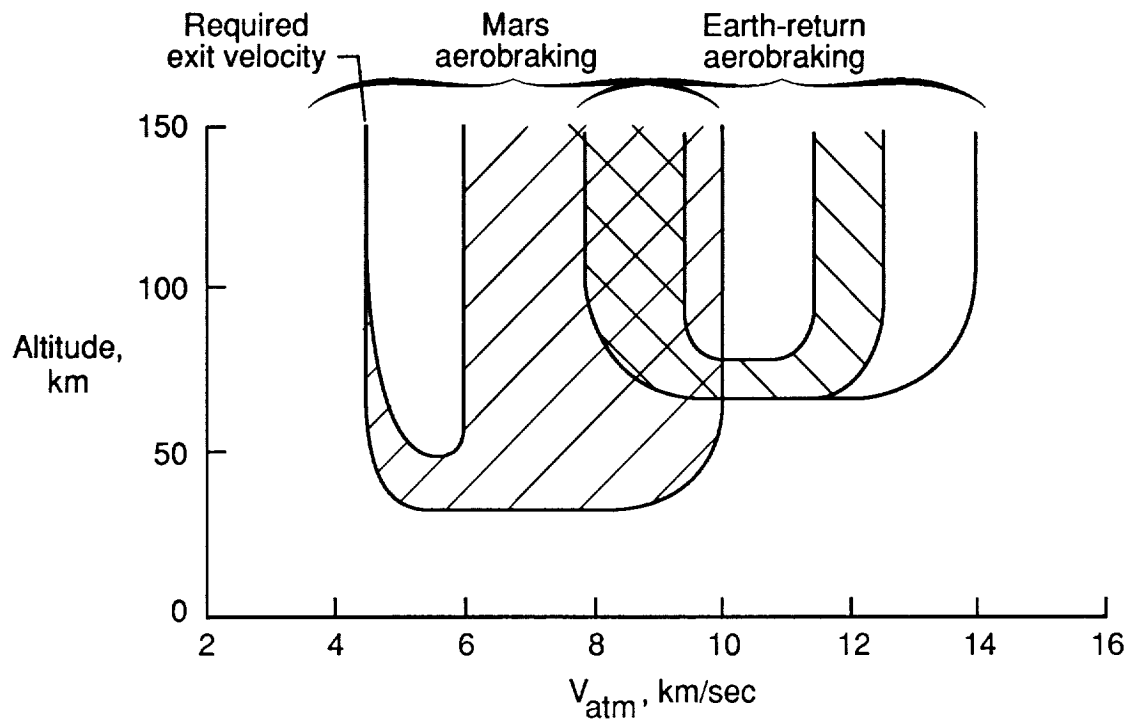
Figure 43. Atmospheric flight domains for selected launch opportunities.
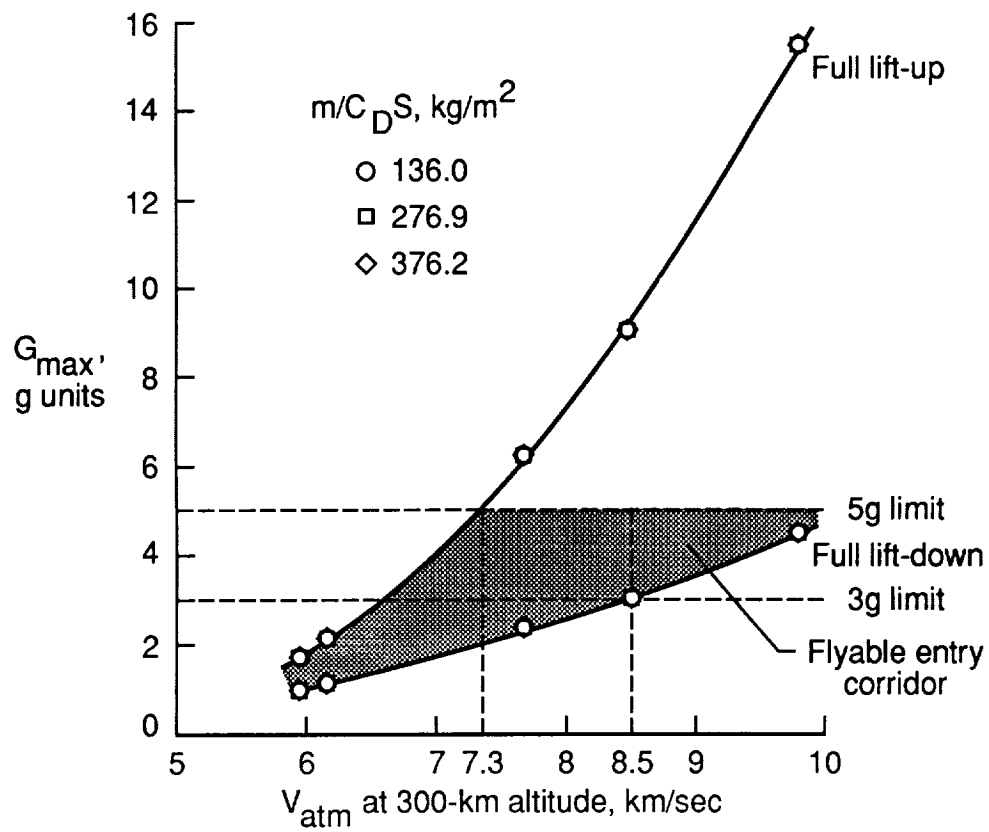
Figure 44. Maximum encountered deceleration for various ballistic-coefficient configurations.
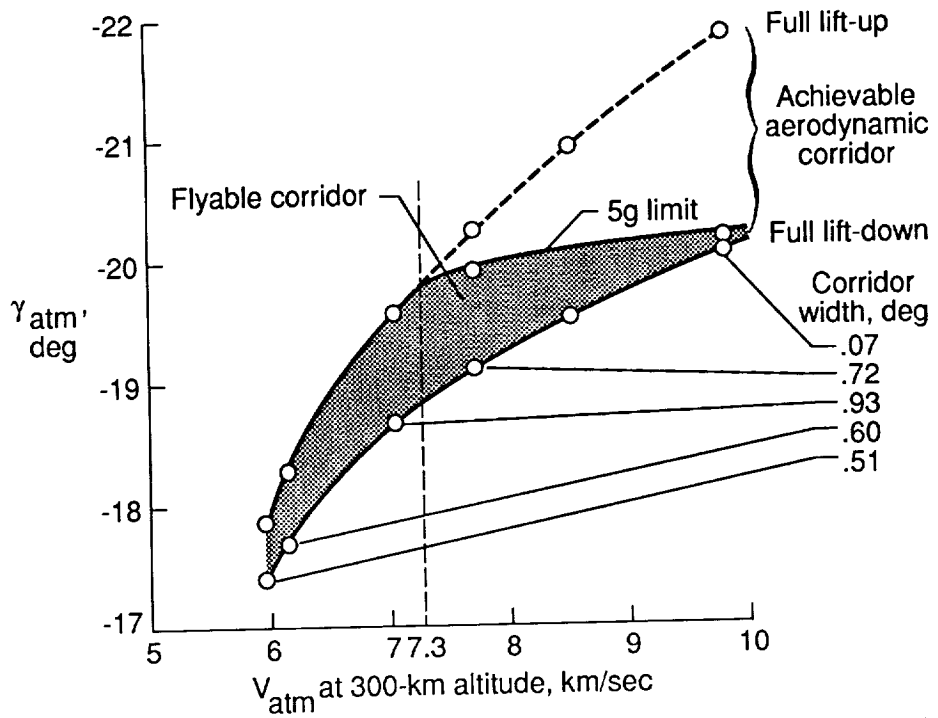
Figure 45. Flyable entry corridor (midrange ballistic-coefficient configuration).
$m/C_DS = 276.9$ kg/m².
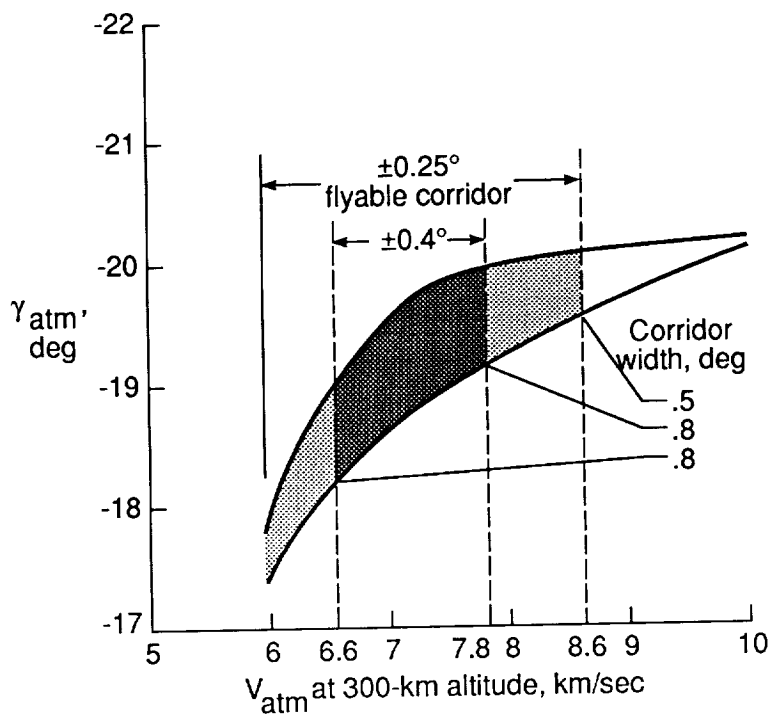
Figure 46. Flyable entry corridor with imposed guidance restrictions (midrange ballistic-coefficient configuration). $m/C_DS = 276.9$ kg/m².

Constraints: a) Trip time 1 to 2 years
b) $W_i/W_f \leq 50$
c) Earth-reentry velocity ≤ 12.5 km/sec
d) Minimum 20-day launch opportunity
e) Mars-entry velocity ≤ 8.6 km/sec (guidance requirements of ± 0.25° in interface flight-path angle)
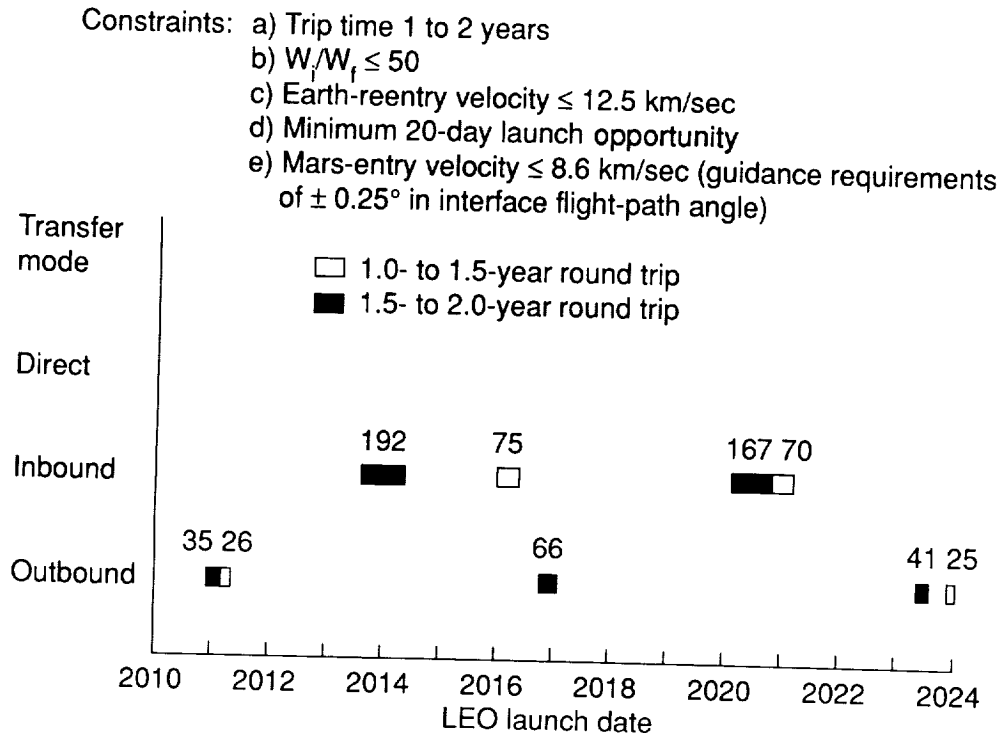
Figure 47. LEO launch opportunities (days) that also satisfy ±0.25° guidance requirement.

Constraints: a) Trip time 1 to 2 years
b) $W_i/W_f \leq 50$
c) Earth-reentry velocity ≤ 12.5 km/sec
d) Minimum 20-day launch opportunity
e) Mars-entry velocity 6.6 to 7.8 km/sec (guidance requirement of ±0.4° in interface flight-path angle)
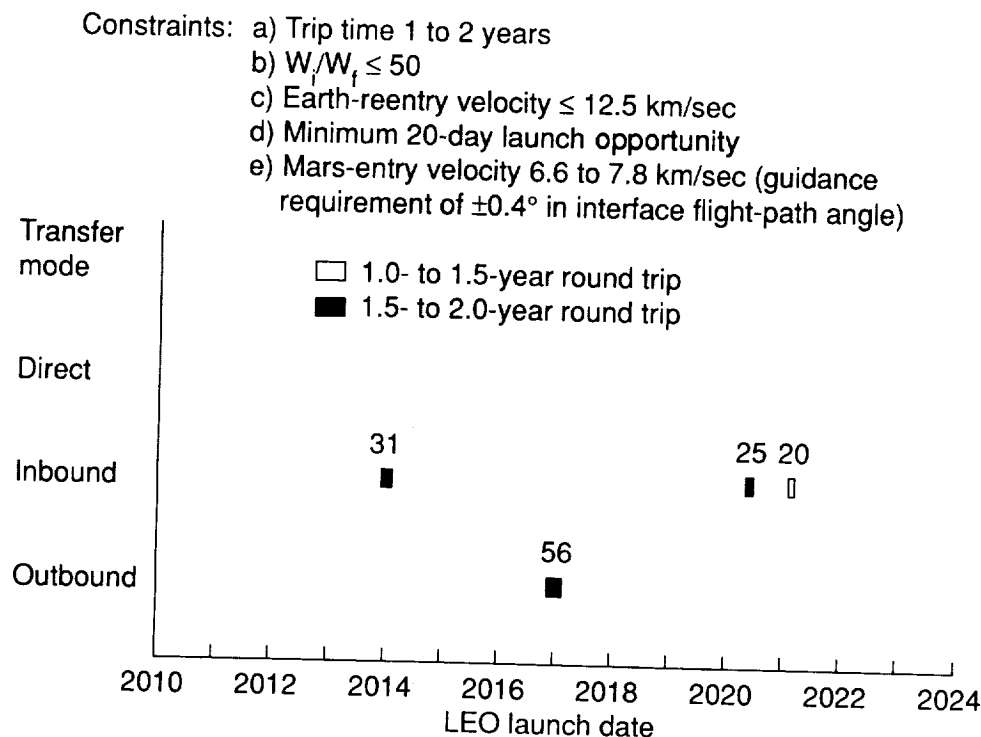
Figure 48. LEO launch opportunities (days) that also satisfy ±0.40° guidance requirement.

64
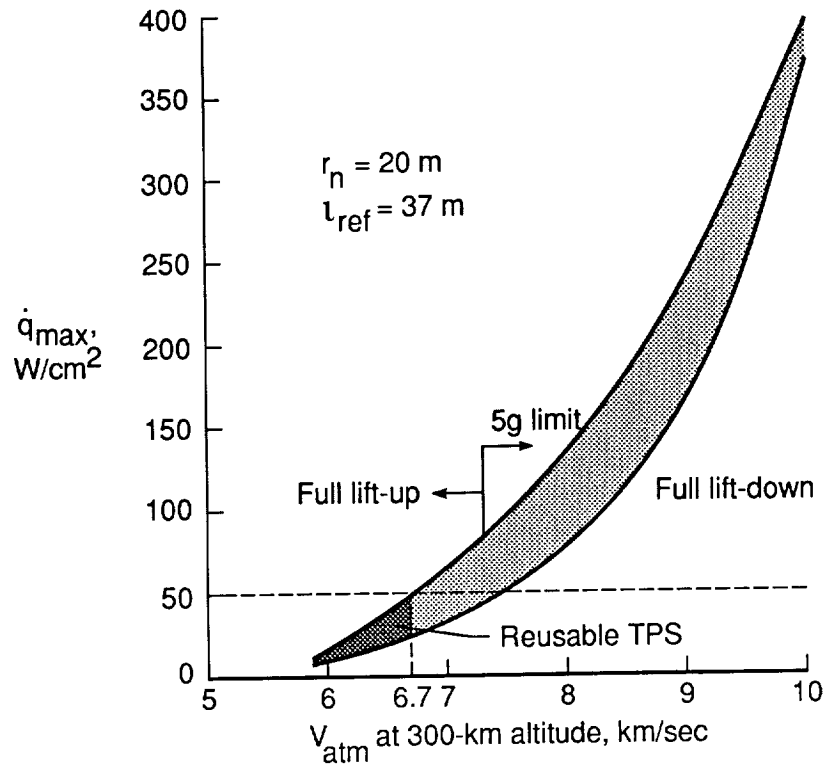
Figure 49. Maximum stagnation-point heat rate, midrange ballistic-coefficient configuration. $m/C_D S = 276.9$ kg/m^2.
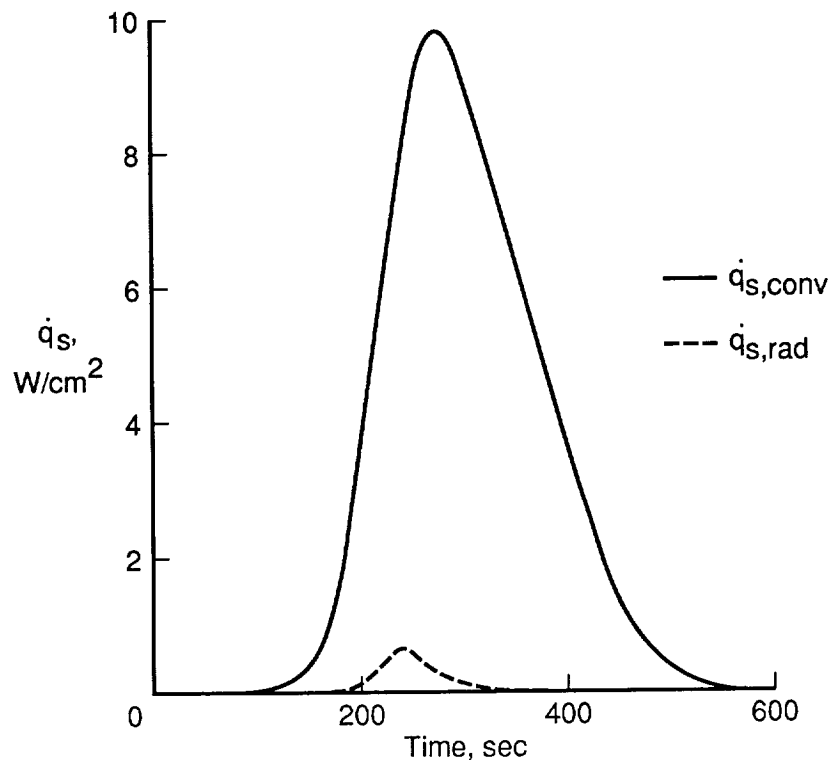
Figure 50. Convective and radiative stagnation-point heat rates for $V_{atm} = 5.95$ km/sec. $m/C_D S = 276.9$ kg/m^2.
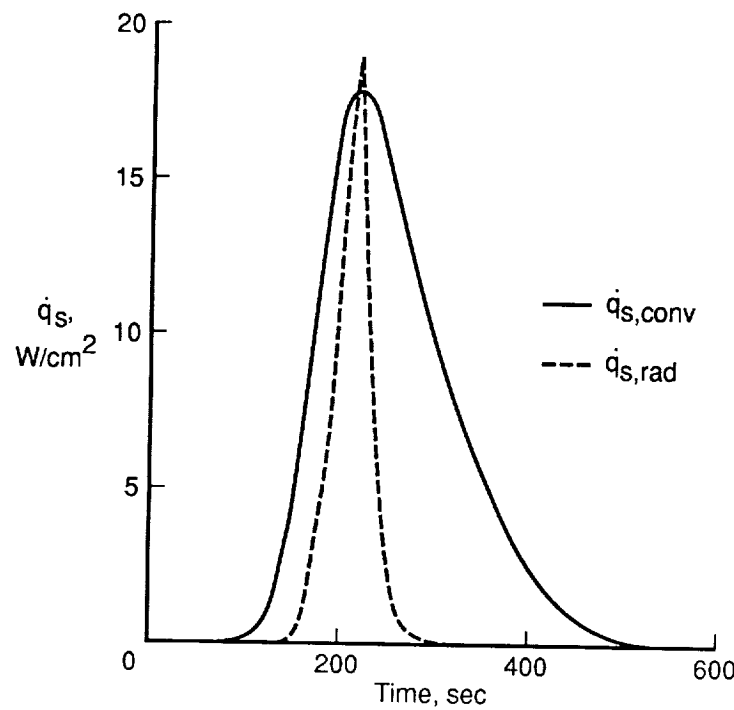
Figure 51. Convective and radiative stagnation-point heat rates for $V_{\text{atm}} = 7.08$ km/sec. $m/C_D S = 276.9$ kg/m^2.
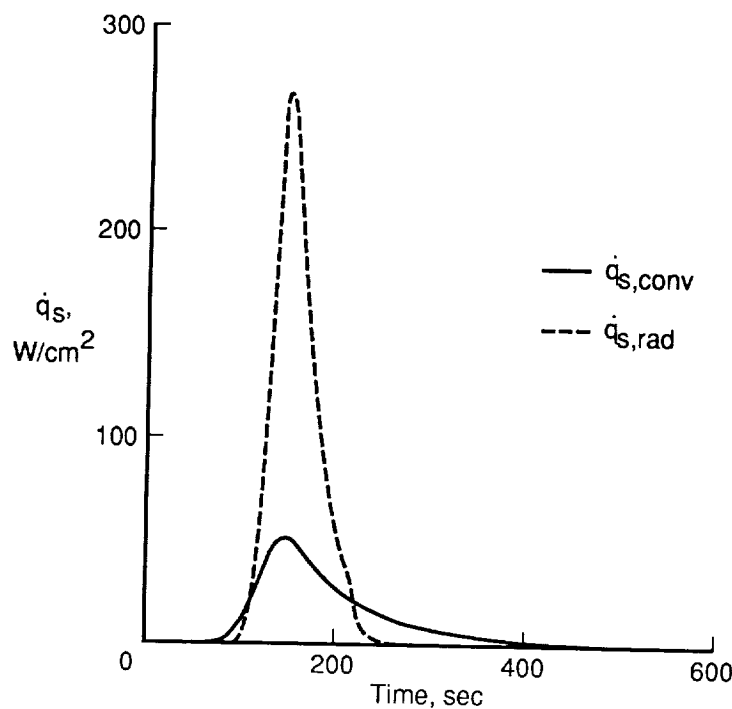
Figure 52. Convective and radiative stagnation-point heat rates for $V_{\text{atm}} = 9.79$ km/sec. $m/C_D S = 276.9$ kg/m^2.

Constraints: a) Trip time 1 to 2 years
b) $W_i/W_f < 50$
c) Earth-reentry velocity < 12.5 km/sec
d) Minimum 20-day launch opportunity
e) Mars-entry velocity ≤ 6.7 km/sec (meets ±0.25°
guidance reusable TPS requirements for midrange
and high ballistic-coefficient configurations)

☐ 1.0- to 1.5-year round trip
■ 1.5- to 2.0-year round trip

Transfer mode

Direct

Inbound

111 50   126 55

Outbound

2010   2012   2014   2016   2018   2020   2022   2024
LEO launch date

Figure 53. LEO launch opportunities (days) based on ±0.25° guidance and reusable TPS requirements for midrange and high ballistic-coefficient configurations.

-22

-21

±0.25°
flyable corridor

-20 |← ±0.4° →|

γ_{atm},
deg

Corridor
width, deg

-19   .5
                                       .8

                                       .8
-18   .5

-17

5   6   6.6   7   7.8 8   8.6 9   10

V_{atm} at 300-km altitude, km/sec
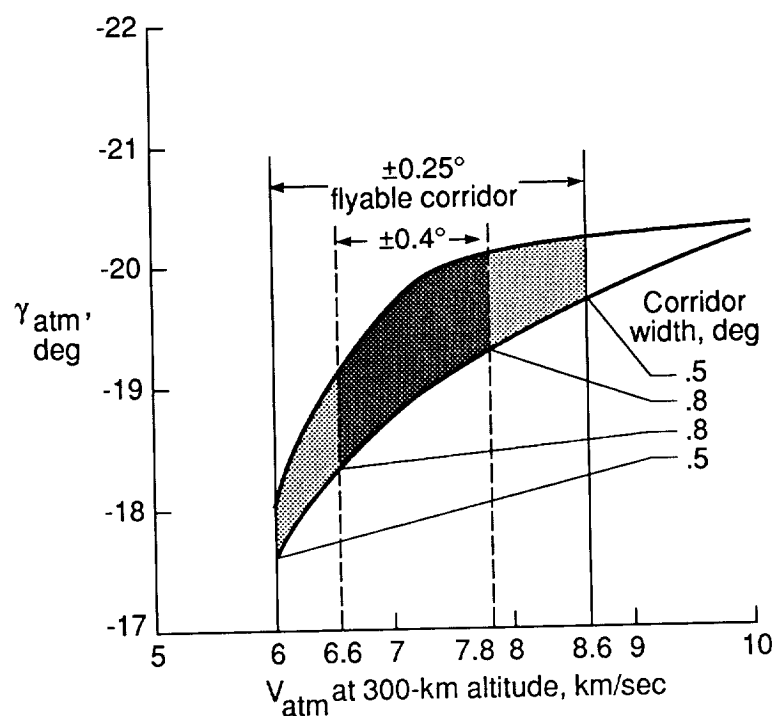
Figure 54. Flyable entry corridor with imposed guidance restrictions (high ballistic-coefficient configuration). $m/C_D S = 376.2$ kg/m^2.

67
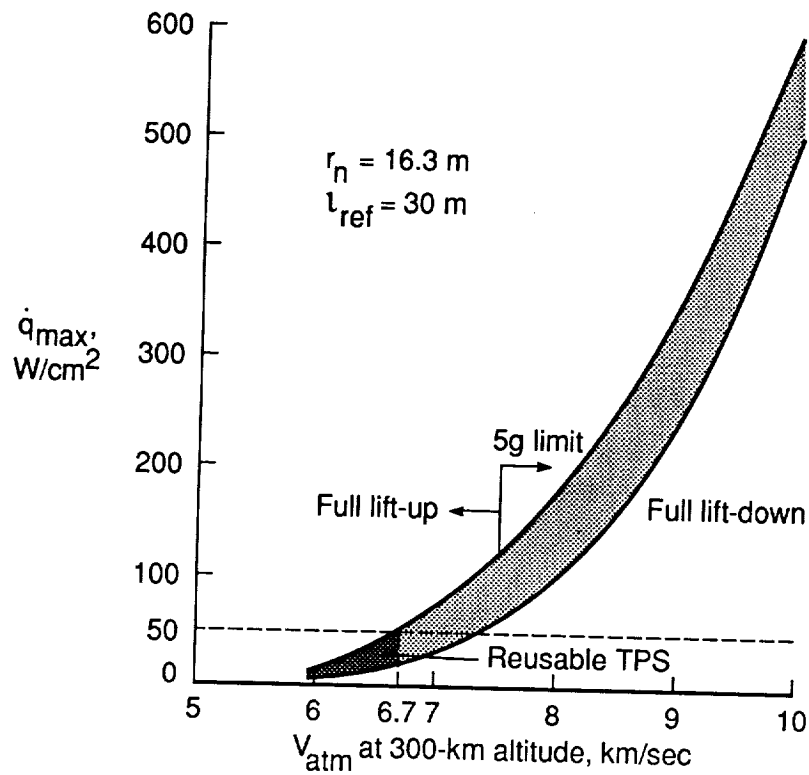
Figure 55. Maximum stagnation-point heat rate for high ballistic-coefficient configuration. $m/C_D S = 376.2$ kg/m^2.
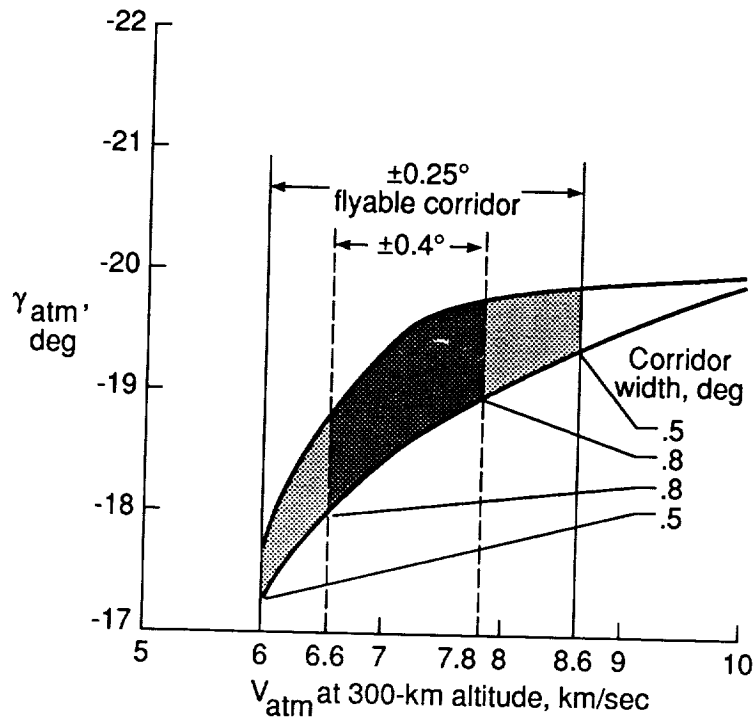

Figure 56. Flyable entry corridor with imposed guidance restrictions (low ballistic-coefficient configuration). $m/C_D S = 136.0$ kg/m^2.
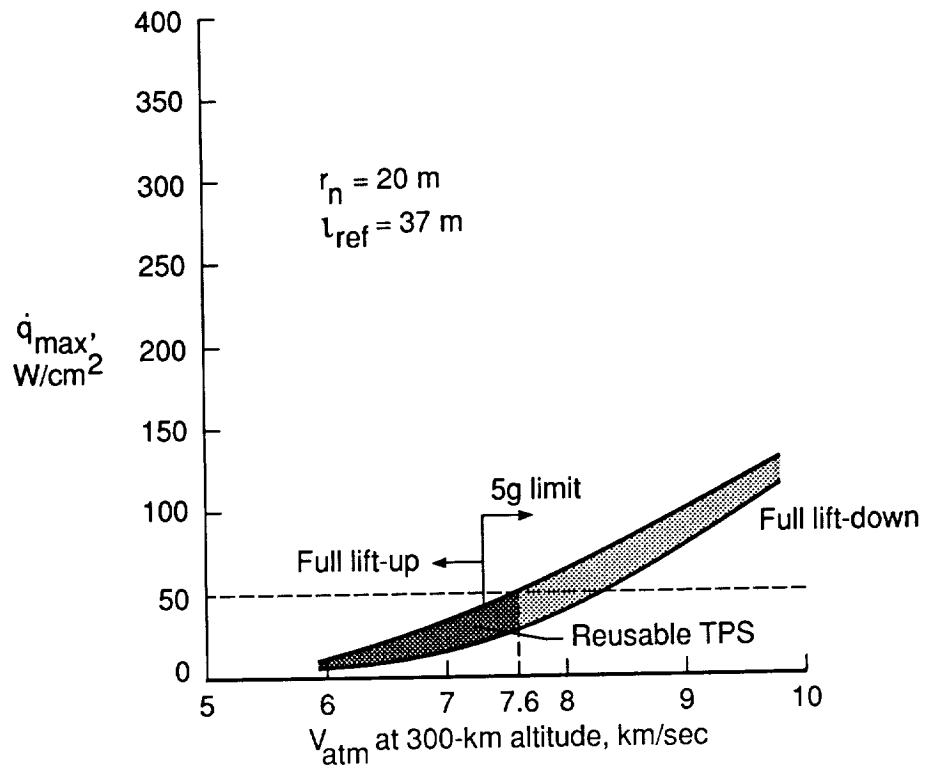
Figure 57. Maximum stagnation-point heat rate for low ballistic-coefficient configuration. $m/C_D S = 136.0$ kg/m^2.

Constraints: a) Trip time 1 to 2 years
b) $W_i/W_f \leq 50$
c) Earth-reentry velocity $\leq$ 12.5 km/sec
d) Minimum 20-day launch opportunity
e) Mars-entry velocity $\leq$ 7.6 km/sec (meets $\pm0.25°$ guidance and reusable TPS requirements for low ballistic-coefficient configuration)
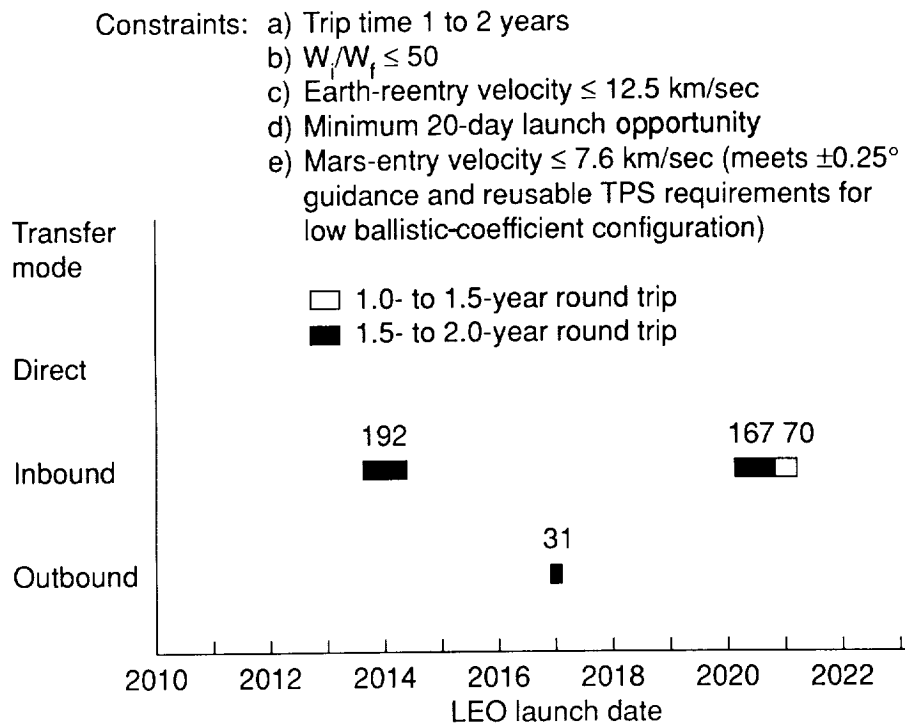
Figure 58. LEO launch opportunities (days) based on $\pm0.25°$ guidance and reusable TPS requirements for low ballistic-coefficient configuration.
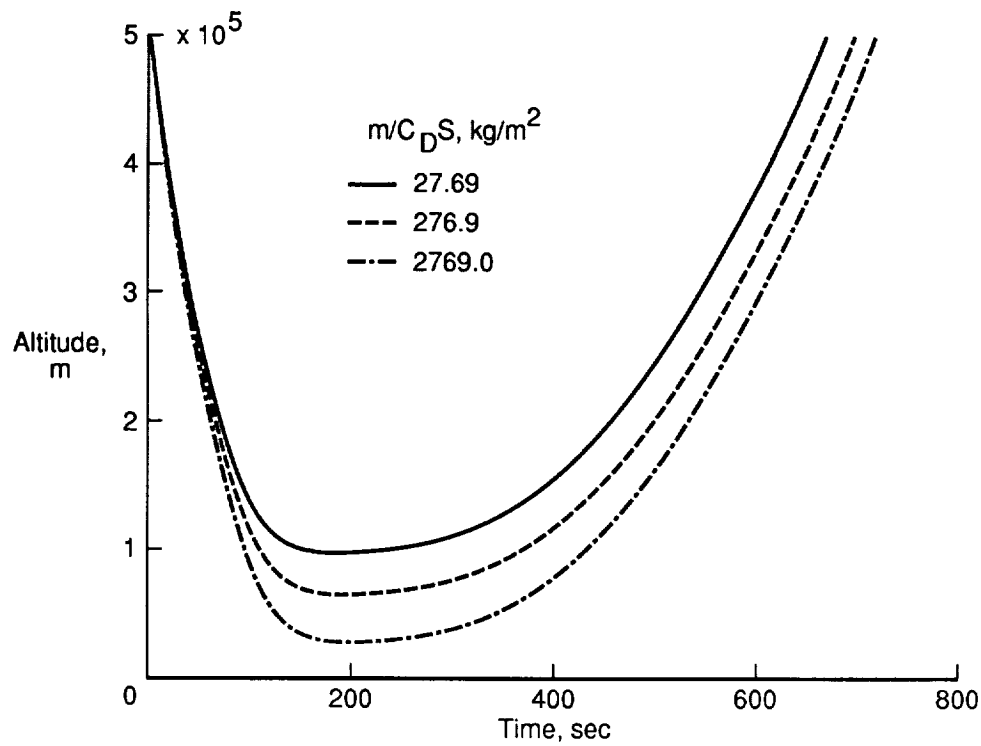
Figure 59. Altitude profile for various ballistic-coefficient configurations. (V_{atm} = 9.79 km/sec, full lift-down transfers.)
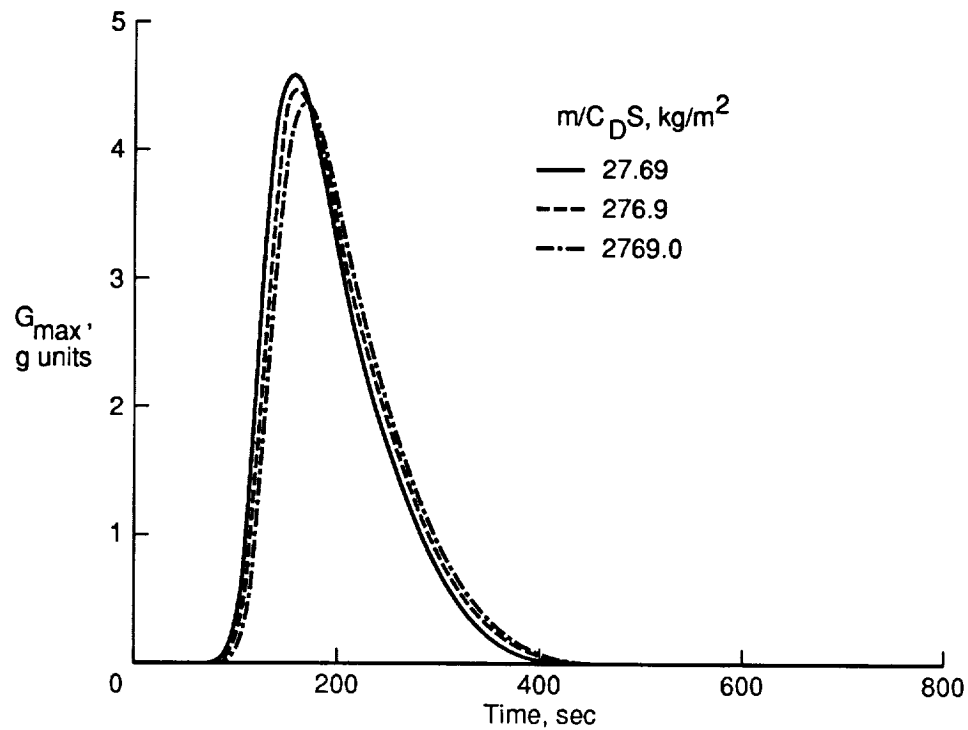

Figure 60. Maximum deceleration for various ballistic-coefficient configurations. (V_{atm} = 9.79 km/sec, full lift-down transfers.)
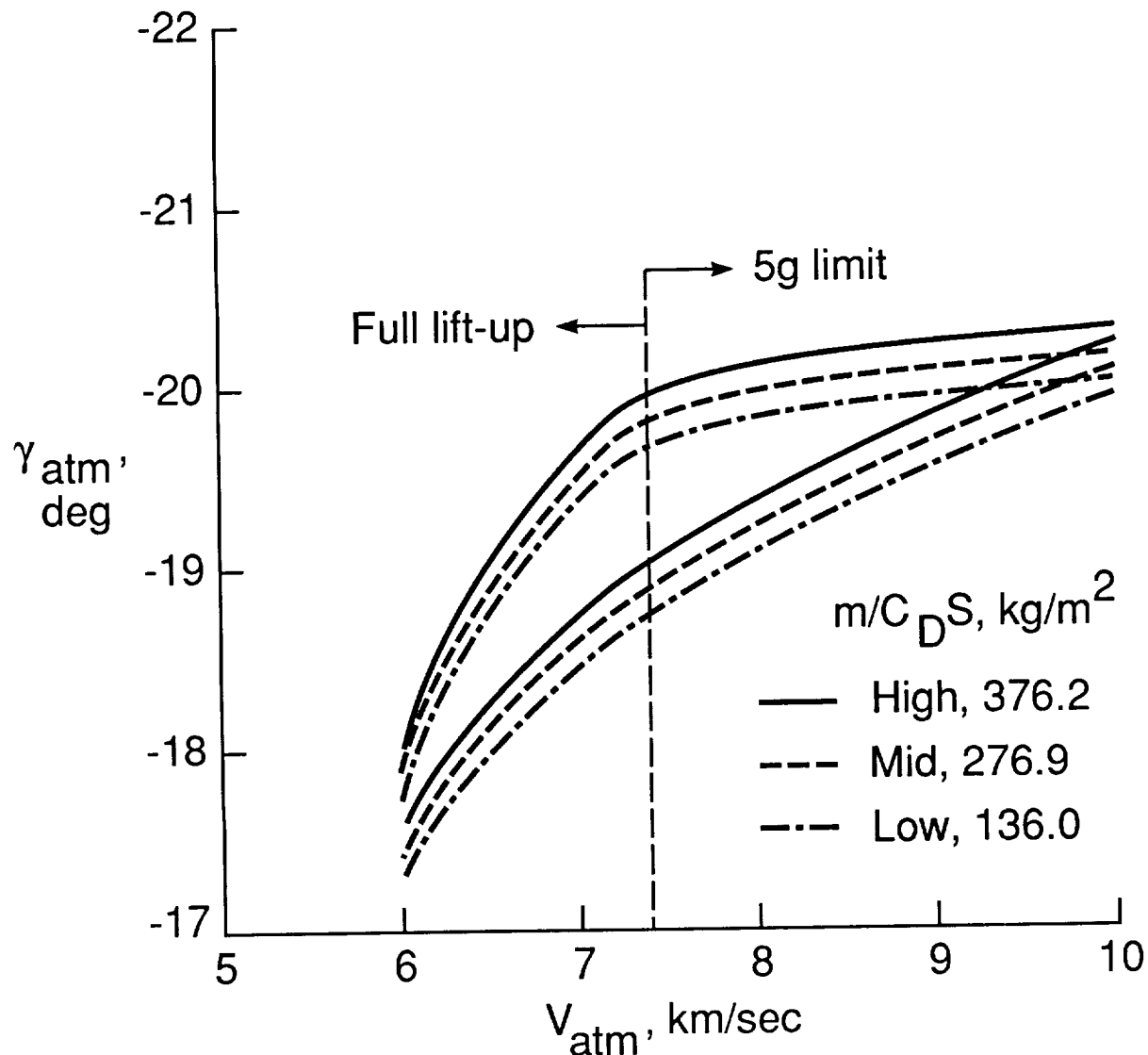
Figure 61. Flyable entry-corridor variation with ballistic coefficient. $m/C_D S$, kg/m^2.
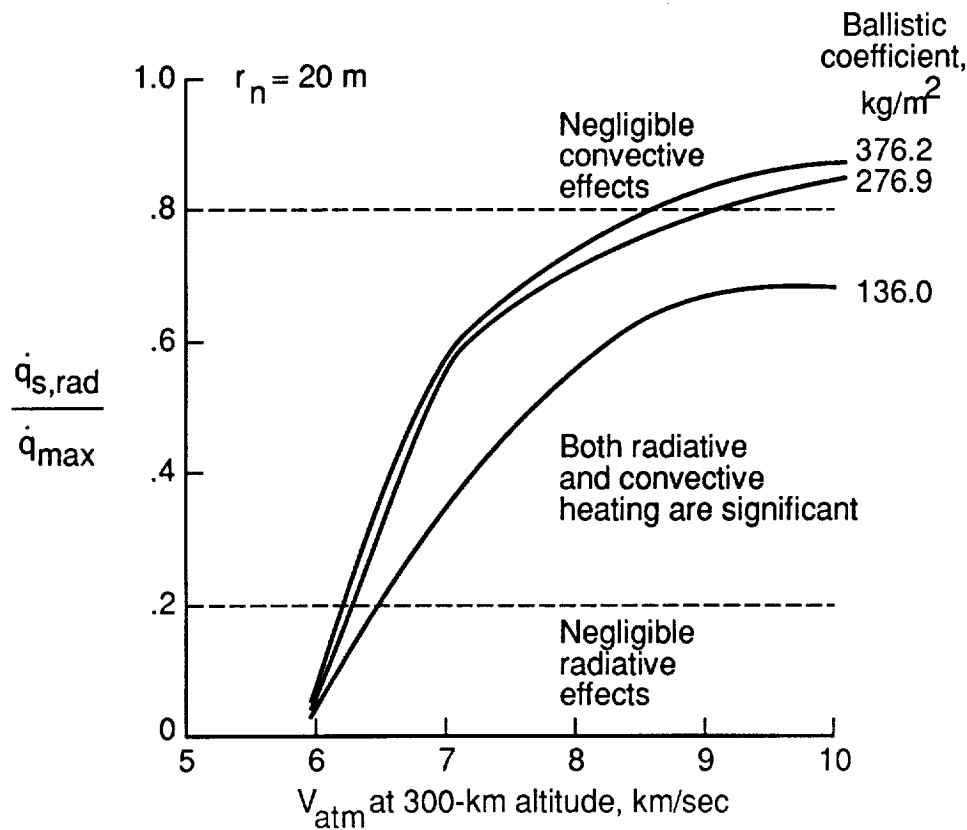
Figure 62. Significance of radiative heating during Mars aerocapture.
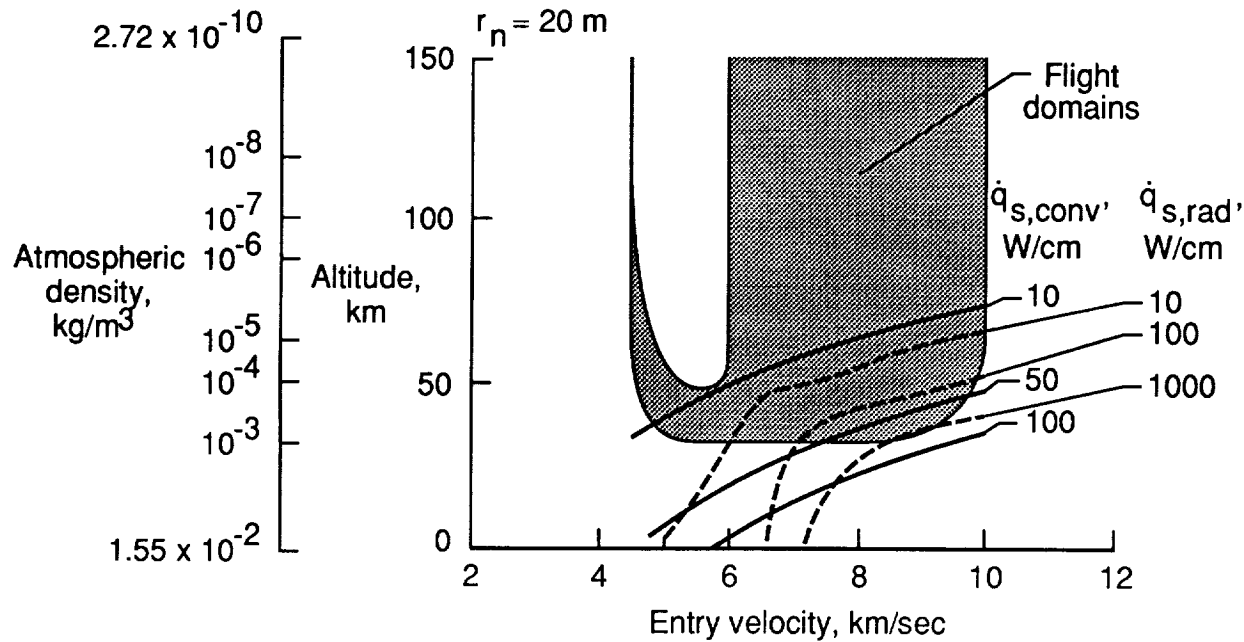
Figure 63. Flight domains and stagnation-point heat rate during Mars atmospheric passage.

Constraints: a) Trip time 1 to 2 years
b) $W_i/W_f < 50$
c) Earth-reentry velocity < 12.5 km/sec
d) Minimum 20-day launch window
e) $V_{atm} \leq 8.6$ km/sec (±0.25° guidance requirement)

□ All-propulsive
■ Aerobrake

Required initial LEO mass, kg
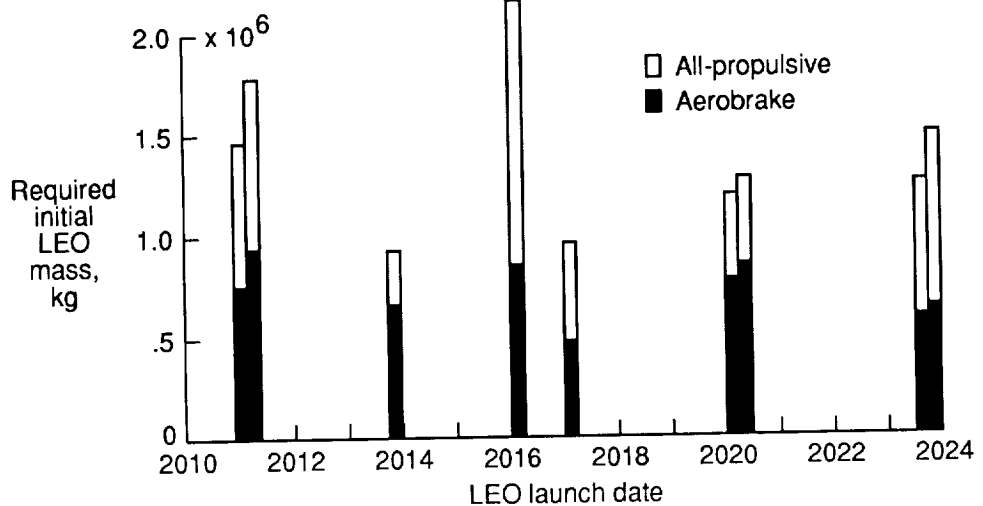
(a) Earth-return mode 1.

Constraints: a) Trip time 1 to 2 years
b) $W_i/W_f < 50$
c) Earth-reentry velocity < 12.5 km/sec
d) Minimum 20-day launch window
e) $V_{atm} \leq 8.6$ km/sec (±0.25° guidance requirement)

□ All-propulsive
■ Aerobrake

Required initial LEO mass, kg
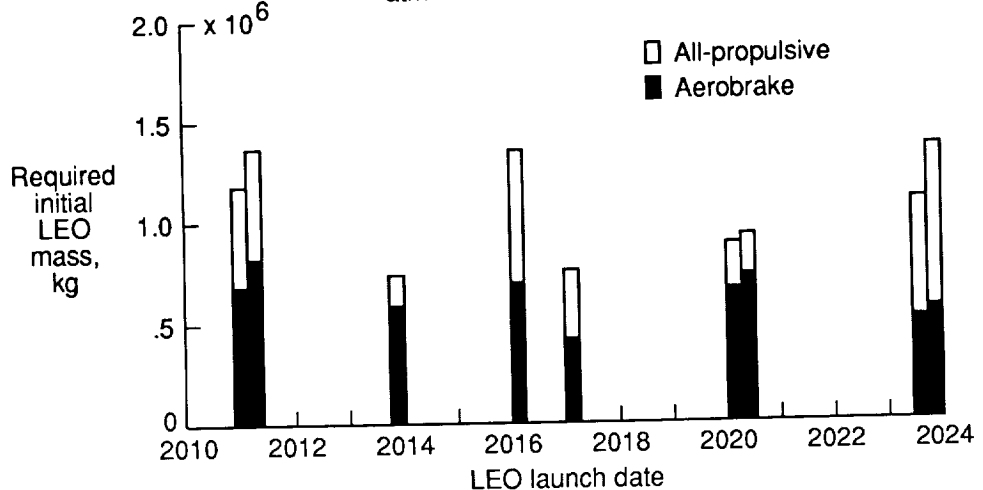
(b) Earth-return mode 2.

Figure 64. Aerobraking versus all-propulsive option.

NASA	Report Documentation Page

National Aeronautics and
Space Administration

1. Report No. NASA TP-3019	2. Government Accession No.	3. Recipient's Catalog No.
4. Title and Subtitle Effect of Interplanetary Trajectory Options on a Manned Mars Aerobrake Configuration		5. Report Date August 1990
		6. Performing Organization Code
7. Author(s) Robert D. Braun, Richard W. Powell, and Lin C. Hartung		8. Performing Organization Report No. L-16661
9. Performing Organization Name and Address NASA Langley Research Center Hampton, VA 23665-5225		10. Work Unit No. 506-40-61-01
		11. Contract or Grant No.
12. Sponsoring Agency Name and Address National Aeronautics and Space Administration Washington, DC 20546-0001		13. Type of Report and Period Covered Technical Paper
		14. Sponsoring Agency Code

15. Supplementary Notes

16. Abstract

Manned Mars missions originating in low-Earth orbit (LEO) in the time frame 2010 to 2025 were analyzed to identify preferred mission opportunities and the associated vehicle and trajectory characteristics. Two chemically propelled vehicle options were considered: (1) an all-propulsive configuration, and (2) a configuration that employs aerobraking at Earth and Mars with low lift-drag (L/D) shapes. Through careful trajectory selection, 11 mission opportunities are identified in which the Mars-entry velocity is between 6 and 10 km/sec and Earth-reentry velocity ranges from 11.5 to 12.5 km/sec. This investigation shows that a low L/D configuration (L/D $\leq$ 0.28) is not feasible for Mars aerobraking without substantial improvements in the interplanetary navigation system. However, even with an advanced navigation system, entry-corridor and aerothermal requirements restrict the number of potential mission opportunities. This study also shows that for a large blunt Mars aerobrake configuration, the effects of radiative heating can be significant at entry velocities as low as 6.2 km/sec and will grow to dominate the aerothermal environment at entry velocities above 8.5 km/sec. The use of aerobraking lowered the required initial LEO weight as much as 59 percent in comparison with the all-propulsive option.

17. Key Words (Suggested by Authors(s)) Trajectory Interplanetary Aerobrake	18. Distribution Statement Unclassified—Unlimited Subject Category 16
19. Security Classif. (of this report) Unclassified	20. Security Classif. (of this page) Unclassified	21. No. of Pages 76	22. Price A05

PAGE 74 + 75 INTENTIONALLY BLANK